NASA CONTRACTOR REPORT

NASA CR-2675

NASA CR-2675

CASE FILE COPY

DEVELOPMENT OF A COMPUTER CODE FOR CALCULATING THE STEADY SUPER/HYPERSONIC INVISCID FLOW AROUND REAL CONFIGURATIONS

Volume I - Computational Technique

Frank Marconi, Manuel Salas, and Larry Yaeger

Prepared by
GRUMMAN AEROSPACE CORPORATION
Bethpage, N.Y. 11714
for Langley Research Center

NATIONAL AERONAUTICS AND SPACE ADMINISTRATION • WASHINGTON, D. C. • APRIL 1976

1. Report No.	2. Government Accession No.	3. Recipient's Catalog No.
NASA CR-2675		

4. Title and Subtitle	5. Report Date
Development of Computer Code for Calculating the Steady Super/Hypersonic Inviscid Flow Around Real Configurations - Volume I - Computational Technique	April 1976
	6. Performing Organization Code
7. Author(s)	8. Performing Organization Report No.
Frank Marconi, Manuel Salas, and Larry Yaeger	
	10. Work Unit No.
9. Performing Organization Name and Address	505-26-10-07
Grumman Aerospace Corporation Bethpage, NY 11714	11. Contract or Grant No. NAS1-11525
	13. Type of Report and Period Covered
12. Sponsoring Agency Name and Address	Contractor Report
National Aeronautics & Space Administration Washington, DC 20546	14. Sponsoring Agency Code

15. Supplementary Notes

Final Report

Langley Technical Monitor: Harris Hamilton

16. Abstract

A numerical procedure has been developed to compute the inviscid super/hypersonic flow field about complex vehicle geometries accurately and efficiently. A second-order accurate finite difference scheme is used to integrate the three-dimensional Euler equations in regions of continuous flow, while all shock waves are computed as discontinuities via the Rankine-Hugoniot jump conditions. Conformal mappings are used to develop a computational grid. The effects of blunt nose entropy layers are computed in detail. Real gas effects for equilibrium air are included using curve fits of Mollier charts. Typical calculated results for shuttle orbiter, hypersonic transport, and supersonic aircraft configurations are included to demonstrate the usefulness of this tool.

A computer code utilizing this computational procedure is described in Volume II of this report.

17. Key Words (Suggested by Author(s))	18. Distribution Statement
Vehicle flow fields, three -dimensional flows, supersonic/hypersonic flows, inviscid flow, numerical flow field computations	Unclassified - Unlimited Subject Category 12

19. Security Classif. (of this report)	20. Security Classif. (of this page)	21. No. of Pages	22. Price*
Unclassified	Unclassified	102	$5.25

*For sale by the National Technical Information Service, Springfield, Virginia 22161

FOREWORD

This work was carried out for NASA by Grumman's Advanced Development Office under the Shuttle Research and Technology project (W. Ludwig, Mgr.; Dr. G. DaForno, Aerothermo Mgr.). The work was carried out under the technical cognizance of Mr. H. Harris Hamilton of NASA Langley Research Center. This work was initiated under a contract from the Office of Naval Research under the technical cognizance of Mr. M. Cooper.

Professor G. Moretti, of the Polytechnic Institute of New York, was a consultant in this work, and it was he who set down the basic guidelines for this computational technique. The authors are very grateful for his guidance.

The authors are pleased to acknowledge the contributions of Dr. G. DaForno, and Dr. B. Grossman of Grumman Aerospace Corp., Dr. M. Pandolfi of the Politecnico di Torino, and H. Harris Hamilton of NASA's Langley Research Center.

Dr. G. DaForno provided his technical experience and many hours of work to help complete this project.

Mr. Hamilton's help throughout the course of this work is greatly appreciated by the authors.

Dr. Pandolfi's help in the implementation of the blunt nose entropy layer calculation, developed by he and Dr. Moretti, is greatly appreciated. He also provided much help in developing the cross flow shock calculation.

Dr. Grossman's many hours of helpful discussion during the course of this work are appreciated.

DEVELOPMENT OF A COMPUTER CODE FOR CALCULATING THE STEADY SUPER/HYPERSONIC INVISCID FLOW AROUND REAL CONFIGURATIONS

VOLUME 1 - COMPUTATIONAL TECHNIQUE

by

F. Marconi, M.D. Salas and L.S. Yaeger

GRUMMAN AEROSAPCE CORPORATION

SUMMARY

A numerical procedure has been developed to compute the inviscid super/hypersonic flow field about complex vehicle geometries accurately and efficiently. A second-order accurate finite difference scheme is used to integrate the three-dimensional Euler equations in regions of continuous flow, while all shock waves are computed as discontinuities via the Rankine-Hugoniot jump conditions. Conformal mappings are used to develop a computational grid. The effects of blunt nose entropy layers are computed in detail. Real gas effects for equilibrium air are included using curve fits of Mollier charts.

Typical calculated results for shuttle orbiter, hypersonic transport and supersonic aircraft configurations are included to demonstrate the usefulness of this tool.

A computer code utilizing this computational procedure is described in Volume II of this report.

CONTENTS

	Page
NOMENCLATURE	ix
INTRODUCTION	1
PROBLEM DEFINITION	5
COMPUTATIONAL FRAME	9
COMPUTATION OF REGIONS OF CONTINUOUS FLOW	23
TREATMENT OF SHOCKS	29
SHARP LEADING EDGE SHOCKS	38
BODY POINT COMPUTATION	41
BLUNT NOSE ENTROPY LAYER CALCULATION	46
REAL GAS EFFECTS (Equilibrium/Frozen Air)	52
SPECIALIZED OUTPUT	58
TYPICAL RESULTS	67
CONCLUSIONS	86
REFERENCES	87
APPENDIX A: SECOND DERIVATIVES OF MAPPINGS	89
APPENDIX B: COEFFICIENTS OF TRANSFORMED EULER EQUATIONS	91

NOMENCLATURE

SYMBOLS

A,B,C,D,E,F	Coefficients of the mappings
a	Speed of sound
$b(\theta,\mathcal{L})$	Radius of the body in the mapped space
$B(Y,Z)$	Radius of the body in the mapped space as a function of the computational coordinates
c_p	Specific heat at constant pressure
c_v	Specific heat at constant volume
$\bar{c}(\theta,\mathcal{L})$	Radius of a wing type shock in the mapped space
C_A	Axial force coefficient (along F.R.L.)
C_D	Drag coefficient
$C_\ell(Y,Z)$	$C_\ell(Y,Z) = \bar{C}_{\ell-1}(Y,Z) \quad 2 \le \ell \le LC + 1$ and $C_1(Y,Z) = B(Y,Z)$
C_L	Lift coefficient
C_M	Moment coefficient
C_N	Normal force coefficient (normal to F.R.L.)
$\bar{C}_\ell(Y,Z)$	Radius of ℓth shock (wing type) in the mapped space
$h(r,\mathcal{L})$	$\theta = h(r,\mathcal{L})$ defines a cross flow shock in the mapped space
h_1, h_2, h_3	Metric coefficients (Fig. 26)
H_o	Stagnation or total enthalpy
$H_i(X,Z)$	$\theta = H_i(X,Z)$ on cross flow type surface i ($i = 1$, $\theta = -\pi/2$ & $i = IC+1$, $\theta = \pi/2$) in the mapped space
$\hat{i},\hat{j},\hat{k}$	Cartesian unit vectors (Fig. 4)
$\hat{I},\hat{J},\hat{K}$	Unit vectors associated with intrinsic shock coordinate system

SYMBOLS

IC	Number of circumferential regions in cross section
Im	Imaginary part
LC	Total number of radial regions in cross section
M	Mach number or mesh point counter in circumferential direction (Fig. 11)
MC(i)	Total number of mesh points in circumferential region i (Fig. 11)
MM	Mesh point counter in circumferential regions (Fig. 11)
N	Mesh point counter in radial direction (Fig. 11)
NC(ℓ)	Total number of mesh points in radial region ℓ (Fig. 11)
NN	Mesh point counter in radial regions (Fig. 11)
p	Pressure (non-dimensionalized with respect to $\bar{p}_\infty$)
P	$\ell n(\bar{p}/\bar{p}_\infty)$
$r,\theta,\mathcal{Z}$	Coordinates in the mapped space
Re	Real part
r',θ',z'	Coordinates used in geometry interrogation (Fig. 5)
R_N	Nose radius
s	Arc length (surface distance)
S	Entropy (non-dimensionalized with respect to $c_{V\infty}$) $S = (\bar{S}-\bar{S}_\infty)/c_{V\infty}$
T	Temperature (non-dimensionalized with respect to $\bar{T}_\infty$)
u,v,w	Velocity components in the x,y,z direction (non-dimensionalized with respect to $\sqrt{\bar{p}_\infty/\bar{\rho}_\infty}$) (Fig. 4)
$\tilde{u},\tilde{v},\tilde{w}$	Intrinsic velocity components

SYMBOLS

W_1, W_2, W_3, W_4, W_5	Intermediate mapped spaces (Eq. 1, Fig. 10)
x, y, z	Cartesian coordinates (left-handed system, non-dimensionalized with respect to an arbitrary length $\bar{\ell}$)
X, Y, Z	Coordinates in the computational space
α	Angle of attack
γ	Ratio of specific heats, c_p/c_v
Γ	a^2/τ, effective γ
ζ	Mapped space (Eq. 1 & Fig. 10)
λ	Characteristic slope
Λ	Wing sweep angle
ξ, η, ω	Intrinsic, local, coordinate system
ξ, η, ζ	Streamline coordinates (Fig. 26)
ρ	Density (non-dimensionalized with respect to $\bar{\rho}_\infty$)
τ	p/ρ effective temperature
ϕ	Circumferential angle (Fig. 36)
$\mathcal{R}$	Gas constant

SUBSCRIPTS

∞	Free stream conditions
ℓ	Counter for wing type shocks, $\ell = 1,2,3, \ldots$
i	Counter for crossflow type shocks, i = 1,2,3, . . .
T	Tangent to a surface
HL	Quantities on the entropy layer surface
SL	Sea level conditions; all quantities with this subscript are non-dimensionalized with respect to their free-stream values

SUBSCRIPTS

fr	Frozen state
EQ	Equilibrium state

Partial derivatives with respect to independent variables are denoted by subscripts.

SUPERSCRIPTS

$\wedge$	Unit vector
$\sim$	Predicted value or intrinsic variable
$-$	Dimensional quantity (except $\bar{c}\ (\theta,\mathcal{P})$ and $\bar{C}_{\ell}(Y,Z)$.

INTRODUCTION

The prediction of the steady three-dimensional inviscid flow fields about a vehicle is of great interest to the designer. Most data necessary to develop a high-speed vehicle is presently obtained from wind tunnel tests which are expensive, slow and sometimes inadequate. The goal of this work was to create a computer code to be used in the development of supersonic vehicle configurations. This code should therefore meet three basic requirements. The first is applicability. In order to obtain the required accuracy for the problem of computing the flow over a wide variety of geometries, for a wide range of Mach numbers and angles of attack, the Euler equations must be solved (Fig. 1). Small perturbation techniques yield accurate results only for the flow over slender bodies flying at low supersonic Mach numbers and small angles of attack, while Newtonian theory yields useful results only for large Mach numbers. Neither of these theories can yield all the details of the flow even in their range of applicability.

The second requirement is efficiency. The calculation of the flow field over a complete vehicle should take no longer than two hours on the C.D.C. 6600 computer. This requirement can only be met by reducing the number of mesh points needed to obtain an accurate solution and keeping the program logic as simple as possible. Computational techniques that "capture" the shocks in the flow field require too many mesh points to obtain acceptable results (ref. 1). The three-dimensional method of characteristics is rejected because of its extreme complexity in program logic.

The last requirement is that the code should be a user-oriented tool. This is in contrast to codes that are tailor-made for a particular configuration (ref. 2) and codes that must be constantly monitored "to nurse the solution through critical regions" (ref. 3). The designer should only have to specify the vehicle geometry and flight conditions to obtain reliable results in a directly usable form (e.g., aerodynamic coefficients, boundary layer inputs, etc.). The vehicle geometry should be input via techniques that, on the one hand, are of the same advanced level as those used in the best incompressible, supersonic and hypersonic three dimensional tools, and, on the other hand,

possess longitudinal and cross sectional continuity needed when solving partial differential equations.

Although the general background of the numerics involved in solving this problem were available at the beginning of this study, no computer tool for actually carrying out accurate flow field calculations past realistic configurations existed.

The only limitation inherent in the present formulation of this problem is that the Mach number in the marching direction (an axis running from the nose of the vehicle to its tail, figure 2) must be supersonic at every point in the flow field. This limitation implies that, first, the free stream Mach number must be "sufficiently" supersonic and, second, that the geometry of the vehicle is such that there are no imbedded regions of subsonic flow. The region around the nose of blunt nose vehicles can be computed using other existing computational techniques (e.g., ref. 4) and once the flow becomes supersonic the present technique can be applied. In general this limitation means that compressions in the flow field that cause subsonic Mach numbers cannot be handled. The general numerical scheme used to solve this problem has been developed by Moretti (refs. 5-8). It follows a number of basic guidelines:

- A second order accurate finite difference marching technique (satisfying the C.F.L. stability condition) is used to numerically integrate the governing partial differential equations
- All shock waves in the flow field are followed and the Rankine-Hugoniot conditions are satisfied across them
- The intersection of two shocks of the same family is computed explicitly
- Conformal mappings are used to develop a computational grid
- The body boundary condition is satisfied by recasting the equations according to the concept of characteristics
- The edge of the entropy layer on blunt nose vehicles is followed from its origin and special devices are used to form derivatives across it

- Real gas effects are included (equilibrium air) when appropriate, by using curve fits of Mollier charts
- Sharp leading edge wings are computed using a local two-dimensional solution

A computer code has been developed which uses these basic ideas. It is described in detail in Volume II of this report. This code has been used extensively to compute external flow fields and has been found to yield accurate results for a wide variety of complex vehicles (Fig. 2) flying at a wide range of supersonic Mach numbers ($M_\infty \sim 2 \rightarrow 26$) and angles of attack ($\alpha \sim \pm 30^\circ$). Computed results are presented in this report to demonstrate and validate this computational procedure.

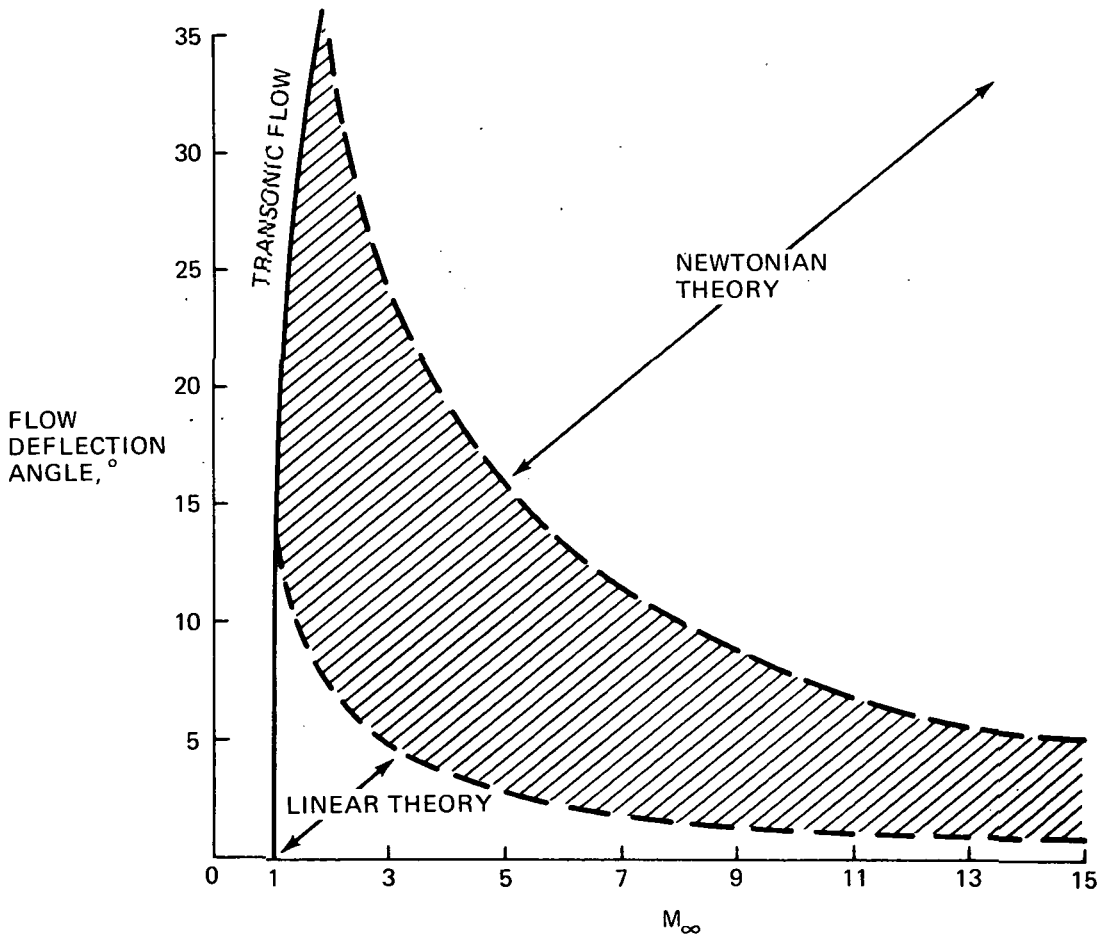

Figure 1. - Regions of applicability of inviscid flow theories (for the surface pressure on a sharp cone).

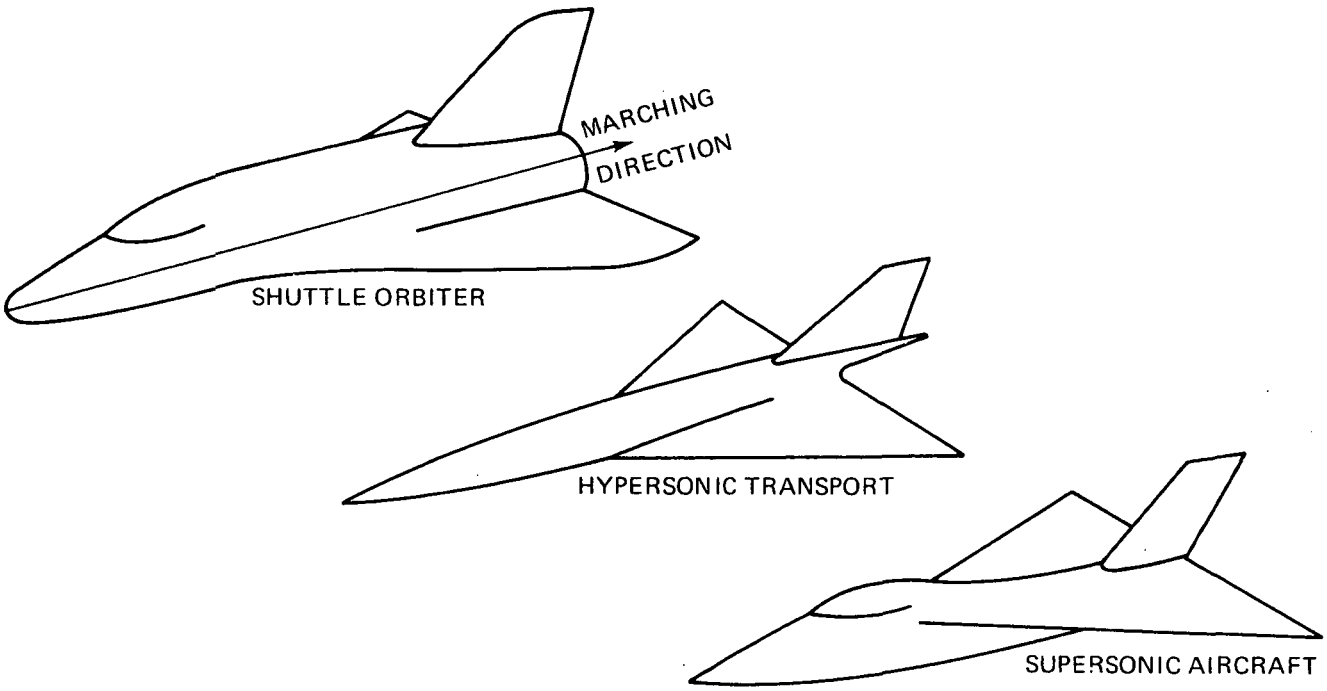

Figure 2. - Typical configurations.

PROBLEM DEFINITION

The problem of computing the external flow about a vehicle flying at supersonic speeds is completely defined by the vehicle geometry and the free stream Mach number, flow direction and ratio of specific heats (γ) for an ideal gas (NOTE: throughout this report an ideal gas will be assumed; modifications of the computational technique for a real gas will be discussed in a later section).

In order to apply the present computational procedure, the free stream Mach number must be supersonic. It will be assumed first that the geometry has a plane of symmetry and second that the free stream velocity vector lies in this plane of symmetry. These two assumptions are not necessary but the present techniques have not yet been applied to asymmetric bodies or bodies at yaw.

In order to apply the boundary condition at the vehicle surface (i.e., vanishing of the normal velocity) the surface and all its first derivatives must be defined. Therefore an analytic definition of the geometry is needed, with continuous first derivatives. The second derivatives of the body geometry appear explicitly in the present formulation of the problem but continuity is not necessary. The flow field over geometries with discontinuous slopes, such as cone-cylinder combinations with sharp expansion corners or geometries with discontinuous wing-fuselage roots and/or canopy-fuselage connections (Fig. 3) have been computed with no special treatment. In these cases computational points on either side of the discontinuity have well defined slopes (the slope at the corner itself is defined by the limit from one side or the other), therefore as far as the computation is concerned there is a smooth transition from one point to the next. Although major difficulties have not been encountered in these cases, best results are obtained for vehicles on which these discontinuities are eliminated by fairings. Special treatment of other slope discontinuities such as sharp leading edge wings will be discussed later.

Since a marching computational technique is employed (i.e., given data on a plane z = constant, (Fig. 4), data on a plane $z + \Delta z$ is computed) a geometry definition that specifies cross sections in the x,y plane (Fig. 5) at each value of z is required.

In order to define the body geometry as a single valued function of two variables, a polar coordinate system is used with the pole at a point in each cross section that will specify the body radius as a single valued function of the polar angle. Of course, the pole of this coordinate system is a function of the axial coordinate. A geometry package that fits all these requirements has been developed by A. Vachris and L. Yaeger (ref. 9).

The main effort in this study is to develop a computational technique that marches downstream from an initial data plane (z = constant, Fig. 4) in which all the dependent variables are known and the component of the velocity in the z direction (w) is supersonic.

For the flow near the nose of the vehicle there are efficient methods available so that the initial data can be easily computed. When the nose of the vehicle is blunt (Fig. 4a) the three-dimensional transonic blunt-body solution developed by Moretti (ref. 4) can be used. If the nose is sharp (Fig.4b) a region very close to the tip is conical. Input data from the flow field solution over sharp conical bodies with attached shocks are readily available (refs. 10 and 11). However, a method has been described by Moretti and Pandolfi (ref. 8) for computing sharp conical solutions. With this technique, a blunt cone solution will asymptote to the sharp cone solution, as the computation proceeds downstream. So that for sharp nose bodies, the calculation is started with a blunt nose solution and continued downstream until the sharp cone solution is reached and then the calculation is restarted with this sharp-nose solution.

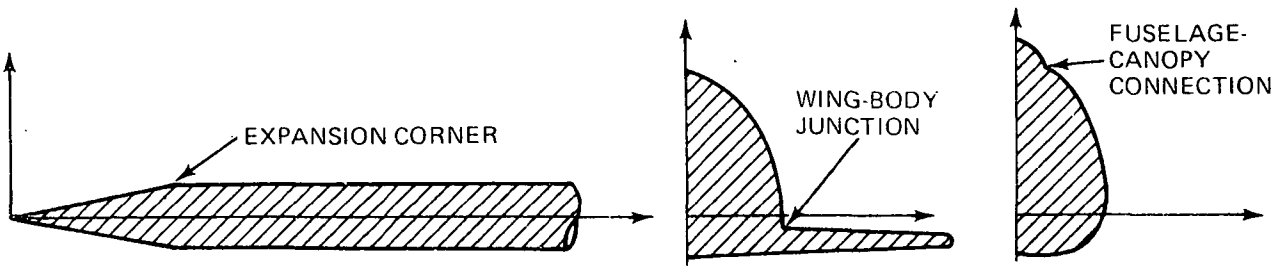

Figure 3. - Geometries with sharp corners.

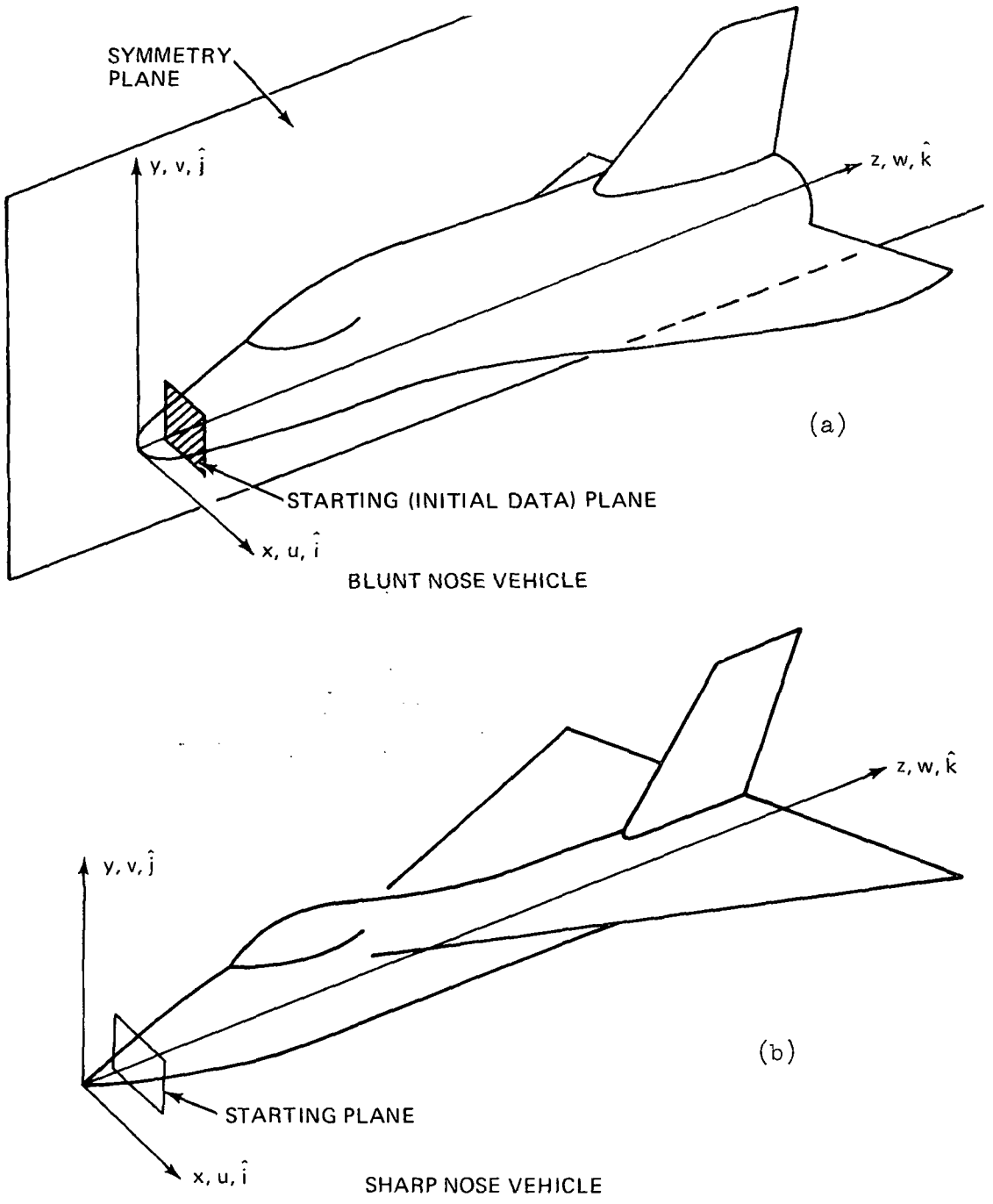

Figure 4. - Coordinate system definition.

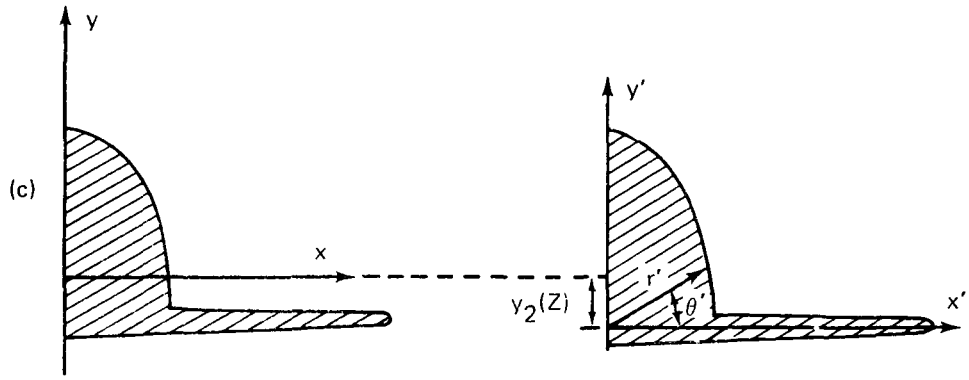

Figure 5. QUICK geometry cross-section definition.

COMPUTATIONAL FRAME

The definition of a computational grid is one of the most crucial steps in the building of a numerical technique. The idea of using conformal mappings to develop the computational mesh in this problem was originally proposed by Moretti (ref. 5).

Three coordinate systems or spaces will be referred to: the physical space (x,y,z), a mapped space (r,θ,ζ), and a computational space (X,Y,Z); figure 6. The physical coordinate system is Cartesian and defines the three velocity components that are computed. The governing equations are written in the physical space and then all derivatives are transformed into the computational space where the mesh points are at uniform intervals ΔX, ΔY, ΔZ.

Each ζ= constant plane in the mapped space is obtained by conformally mapping the geometry cross sections in the physical space into near circles, in the mapped space. So that the region bounded by the body and the bow shock becomes a ring in the mapped space. The corresponding computational space is obtained by normalizing the radial distance between body and shock (X-direction) and the circumferential distance between the two symmetry planes (Y-direction) (Fig. 7). The mapped space serves three purposes: first, it distributes the body mesh points (which are evenly spaced in the computational plane) so that the necessary resolution is obtained in regions of large curvature where truncation error may otherwise become too large. This is demonstrated in figures 7 and 8 where the mesh points are concentrated near the tips of the wing and the tail in the physical space. Second, the mapping makes the body and bow shock positions single valued functions $r = b(\theta,\zeta)$ and $r = \bar{c}(\theta,\zeta)$ in the mapped plane. Third, since shock waves imbedded in the flow field become mesh lines, the only chance of success is that their traces in a mapped space are (for the cross flow shocks) predominantly along lines θ = constant and (for the wing-type shocks) predominantly along lines r = constant. This enables one to define a number of regions in the computational space when more than one shock exists in a cross section. The dotted lines in figure 9 are extensions of shocks to complete the boundaries of these regions. The points on either side of these portions of the boundaries are allowed to pass information across the boundary. The require-

ments for such a surface are that they meet the shocks at the edge points (Fig. 9) and that they do not intersect each other if they are of the same type. The cross flow surfaces (i.e., extensions of cross flow shocks) are defined as θ = constant. The constant taken is the value of θ at the last point on the shock. Since the wing-type shocks intersect each other, points on their dividing surfaces are taken at the same percent of the distance between its two neighboring boundaries at its edge shock points, so that no point on the dividing surface of a wing-type shock gets any closer to the two adjacent boundaries of the shock than its edge shock points.

Now the transformation $(r,\theta,z) \rightarrow (x,y,z)$ is considered. A series of algebraic, invertible, conformal mappings have been developed which transform a wide variety of cross sections (Fig. 2) into near circles.

Let $\zeta = re^{i\theta}$, $W_{1,2,3,4,5}$, be intermediate spaces, and $G = x + iy$ (Fig. 10).

$$\zeta = re^{i\theta} \qquad \text{(a)}$$

$$W_1 = \zeta - F/\zeta \qquad \text{(b)}$$

$$W_2 = W_1 + iE \qquad \text{(c)} \qquad (1)$$

$$W_3 = W_2 + B/W_2^2 \qquad \text{(d)}$$

$$W_4 = W_3 + iA \qquad \text{(e)}$$

$$W_5 = W_4 + D^2/(4W_4) \qquad \text{(f)}$$

$$G = W_5 + iC \qquad \text{(g)}$$

These mappings give $x = f_1(r,\theta,z)$, $y = f_2(r,\theta,z)$ while $z' = z$ completes the definition of the transformation.

Each coefficient A,B,C,D,E and F is determined by placing the singularities of the mappings inside the body so as to obtain a near circle in the ζ-plane. Therefore these coefficients are functions of the axial coordinate z. The coefficients are determined by the geometry. These mappings can handle a wide variety of vehicles with the coefficients defined as follows:

$$A = 0^{*} \qquad \text{(a)}$$

$$B = i(D^3/54) \qquad \text{(b)}$$

$$C = y_2 \qquad \text{(c)} \qquad (2)$$

$$D = \sqrt{x_2^2 - (y_1 - y_2)^2} \qquad \text{(d)}$$

$$E = (\mathrm{Im}(W_{2_1}) + \mathrm{Im}(W_{2_4}))/2 \qquad \text{(e)}$$

$$F = (W_{2_5} - iE)^2/4 \qquad \text{(f)}$$

where W_{2_1}, W_{2_4} and W_{2_5} are the positions of points 1, 4 and 5 (Fig. 10) in the W_2 plane. These points are computed by inverting equations (1) as follows,

$$y_5 = \sqrt{(y_4 - y)^2 - x_3^2}$$

and

$$G_1 = iy_1 \qquad \text{(a)}$$

$$G_4 = iy_4 \qquad \text{(b)} \qquad (3)$$

$$G_5 = iy_5 \qquad \text{(c)}$$

and for K = 1,4 and 5

$$W_{5_K} = G_K - iC \qquad \text{(a)}$$

$$W_{4_K}^2 - 4W_{5_K} W_{4_K} + D^2 = 0 \qquad \text{(b)} \qquad (4)$$

$$W_{3_K} = W_{4_K} - iA \qquad \text{(c)}$$

$$W_{2_K}^3 - W_{3_K} W_{2_K}^2 - B = 0 \qquad \text{(d)}$$

The roots with the largest modulus is used in equations (4b and d).

* A = 0 for all applications thus far, $A \neq 0$ would give the mappings even greater generality.

The derivatives A_z, B_z, etc., are obtained in a straight forward manner by differentiating equations (2-4) and are functions of x_{2_z}, x_{3_z}, y_{1_z}, y_{2_z}, and y_{4_z} (Fig. 10).

To obtain r,θ in terms of x,y(at $\zeta = z$) all of the mappings must be inverted. This is a straightforward process that can be carried out using equations (1a) through (1g) (similar to the procedure used in equations (4)).

In order to transform the derivatives in the governing equations from the physical space to the computational space the first and second derivatives of all the transformations are needed. The derivatives r_x, r_y, θ_x, and θ_y can be calculated as follows.

$$G_\zeta = (W_{1\zeta})(W_{3W_2})(W_{5W_4})(G_{W_5}) \tag{5}$$

and

$$\zeta_G = 1/G_\zeta \tag{6}$$

If $\zeta = u + iv$, where $u = r\cos\theta$ and $v = r\sin\theta$, then

$$u_x = \mathrm{Re}(\zeta_G)$$

$$v_x = \mathrm{Im}(\zeta_G)$$

and from the Cauchy-Riemann conditions

$$u_y = -v_x$$

$$v_y = u_x$$

thus

$$r_x = (uu_x + vv_x)/r \qquad \text{(a)}$$

$$r_y = (uu_y + vv_y)/r \qquad \text{(b)}$$

$$\theta_x = (uv_x - vu_x)/r \qquad \text{(c)} \tag{7}$$

$$\theta_y = (uv_y - vu_y)/r \qquad \text{(d)}$$

For the $\not{z}$-derivatives of the mappings the following results are obtained:

$$W_1 = -F_{\not{z}}/\zeta \qquad \text{(a)}$$

$$W_{2\not{z}} = W_{1\not{z}} + iF_{\not{z}} \qquad \text{(b)}$$

$$W_{3\not{z}} = W_{2\not{z}}\,(W_{3W_2}) + B_{\not{z}}\,/W_2^{\,2} \qquad \text{(c)}$$

$$W_{4\not{z}} = W_{3\not{z}} + iA_{\not{z}} \qquad \text{(d)}$$

$$W_{5\not{z}} = W_{4\not{z}}\,(W_{5W_4}) + D_{\not{z}}\,/2W_4 \qquad \text{(e)} \qquad (8)$$

$$G_{\not{z}} = W_{5\not{z}} + iC_{\not{z}} \qquad \text{(f)}$$

$$x_{\not{z}} = \mathrm{Re}\,(G_{\not{z}}) \qquad \text{(g)}$$

$$y_{\not{z}} = \mathrm{Im}\,(G_{\not{z}}) \qquad \text{(h)}$$

Where $A_{\not{z}} = A_z$, $B_{\not{z}} = B_z$ etc., since $z = \not{z}$ and $z_{\not{z}} = 1$. Now since $r, \theta, \not{z}$ are independent coordinates, it follows that $r_{\not{z}} = \theta_{\not{z}} = 0$, therefore

$$r_{\not{z}} = r_x\, x_{\not{z}} + r_y\, y_{\not{z}} + r_z\, z_{\not{z}} = 0$$

and

$$\theta_{\not{z}} = \theta_x\, x_{\not{z}} + \theta_y\, y_{\not{z}} + \theta_z\, z_{\not{z}} = 0$$

solving for r_z and θ_z the following results are obtained

$$r_z = -(r_y\, y_{\not{z}} + r_x\, x_{\not{z}}) \qquad \text{(a)}$$

$$\theta_z = -(\theta_y\, y_{\not{z}} + \theta_x\, x_{\not{z}}) \qquad \text{(b)} \qquad (9)$$

The second derivatives of this transformation needed for the body point calculation are derived in Appendix A.

The singularities of these mappings are all inside the body so that the mappings are never evaluated at singular points. It is not necessary that the mappings be conformal but it has been found that conformal mappings give the best results in terms of mesh point distribution. It is also not necessary that r, θ, ζ be orthogonal coordinates, in fact in general they are not.

These mappings (equations (1))use simple algebraic expressions and their coefficients are defined explicitly so that transformation from one space to another takes a minimum of time. Considerable work has been done to develop conformal mappings that can map arbitrary cross sections into circles or near circles (ref. 12). These generalized mappings offer a greater flexibility than the mappings used herein but would require a large increase in computational time.

With the mapped plane completely defined, the transformation between the computational space and the mapped space $(X,Y,Z) \rightarrow (r,\theta,\zeta)$ is required. Consider a cross section ($Z = \zeta$= constant) with multiple shock waves, e.g., (Fig. 9) bow shock, wing shock and tail shock plus two cross flow shocks. The computational plane is divided into IC regions in the Y direction, and LC regions in the X direction, they are ordered as in figure 9. The body is described by $r = B(Y,Z)$ and a wing-type shock as $r = \bar{C}_{\ell}(Y,Z)$ for $\ell = 1 \rightarrow LC$ ($\ell = LC$ being the bow shock). Similarly, the cross flow shocks are described as $\theta = H_i(X,Z)$ for $i = 1 \rightarrow IC + 1$ ($i = 1$ is the bottom symmetry plane and $i = IC + 1$ is the top symmetry plane). These surfaces are shocks for some range of X and Y and arbitrary (dividing) surfaces for other values of X and Y as described previously.

Now define LC + 1 surfaces such that:

$$C_1(Y,Z) \equiv B(Y,Z)$$

$$C_{\ell}(Y,Z) \equiv \bar{C}_{\ell-1}(Y,Z) \qquad (\ell = 2,3,\ldots LC + 1)$$

The transformation to the computational plane then can be written as:

$$X = (r-C_{\ell})/(C_{\ell+1} - C_{\ell}) \qquad (a)$$

$$Y = (\theta-H_i)/(H_{i+1} - H_i) \qquad (b) \qquad (10)$$

$$Z = \zeta \qquad (c)$$

The coordinates X,Y,Z are not orthogonal. The boundary C_{ℓ} in the mapped plane becomes X = 0 in region ℓ and $C_{\ell+1}$ becomes X = 1. Similarly, the IC regions in the Y-direction in the computational plane are bounded by Y = 0 and Y = 1.

Inverting this transformation yields the result:

$$r = X(C_{\ell+1}-C_{\ell}) + C_{\ell} \qquad (a)$$

$$\theta = Y(H_{i+1}-H_i) + H_i \qquad (b) \qquad (11)$$

$$\zeta = Z \qquad (c)$$

Again the derivatives of this transformation $X_r, X_\theta, X_\zeta, Y_r, Y_\theta$ and Y_ζ are needed.

First

$$r_X = (C_{\ell+1}-C_{\ell}) \qquad (a)$$

$$r_Y = (C_{Y_{\ell+1}} - C_{Y_{\ell}}) X + C_{Y_{\ell}} \qquad (b)$$

$$r_Z = (C_{Z_{\ell+1}} - C_{Z_{\ell}}) X + C_{Z_{\ell}} \qquad (c)$$

$$\theta_X = (H_{X_{\ell+1}} - H_{X_i}) Y + H_{X_i} \qquad (d) \qquad (12)$$

$$\theta_Y = (H_{i+1} - H_i) \qquad (e)$$

$$\theta_Z = (H_{Z_{i+1}} - H_{Z_i}) Y + H_{Z_i} \qquad (f)$$

$$\zeta_X = 0 \qquad (g)$$

$$\zeta_Y = 0 \qquad (h)$$

$$\zeta_Z = 1 \qquad (i)$$

The Jacobian of the transformation is defined as:

$$J \equiv \frac{\partial(r,\theta,\not{z})}{\partial(X,Y,Z)} \equiv \begin{vmatrix} r_X & r_Y & r_Z \\ \theta_X & \theta_Y & \theta_Z \\ \not{z}_X & \not{z}_Y & \not{z}_Z \end{vmatrix}$$

and thus

$$X_r = \frac{1}{J}\left[\frac{\partial(X,\theta,\not{z})}{\partial(X,Y,Z)}\right] \quad (a)$$

$$Y_r = \frac{1}{J}\left[\frac{\partial(Y,\theta,\not{z})}{\partial(X,Y,Z)}\right] \quad (b)$$

$$X_\theta = \frac{1}{J}\left[\frac{\partial(r,X,\not{z})}{\partial(X,Y,Z)}\right] \quad (c)$$

$$Y_\theta = \frac{1}{J}\left[\frac{\partial(r,Y,\not{z})}{\partial(X,Y,Z)}\right] \quad (d) \qquad (13)$$

$$X_{\not{z}} = \frac{1}{J}\left[\frac{\partial(r,\theta,X)}{\partial(X,Y,Z)}\right] \quad (e)$$

$$Y_{\not{z}} = \frac{1}{J}\left[\frac{\partial(r,\theta,Y)}{\partial(X,Y,Z)}\right] \quad (f)$$

After some algebraic manipulations the above derivatives can be written in the following form:

$$X_r = 1./\left[\delta + XD_1\delta_Y + D_1 C_{y_{\not{z}}}\right] \quad (a)$$

$$Y_r = D_1 X_r \quad (b) \qquad (14)$$

$$Y_\theta = 1./\left[\Delta + YD_2\Delta_X - D_2 H_{xi}\right] \quad (c)$$

$$X_\theta = D_2 Y_\theta \quad (d)$$

$$X_2 = -\frac{\left[X\delta_Z + X\delta_Y D_3 + C_{Z_\ell} + C_{Y_\ell} D_3\right]}{\left[\delta + X D_4 \delta_Y + C_{y_\ell} D_4\right]} \qquad \text{(e)} \qquad (14)$$

$$Y_2 = D_3 + D_4 X_2 \qquad \text{(f)}$$

where

$$\delta = C_{\ell+1} - C_\ell \qquad \text{(a)}$$

$$\delta_Y = C_{Y\ell+1} - C_{Y\ell} \qquad \text{(b)}$$

$$\delta_Z = C_{Z\ell+1} - C_{Z\ell} \qquad \text{(c)}$$

$$\Delta = H_{i+1} - H_i \qquad \text{(d)}$$

$$\Delta_X = H_{X_{i+1}} - H_{X_i} \qquad \text{(e)}$$

$$\Delta_Z = H_{Z_{i+1}} - H_{Z_i} \qquad \text{(f)} \qquad (15)$$

$$D_1 = -(Y\Delta_X - H_{X_i})/\Delta \qquad \text{(g)}$$

$$D_2 = -(X\delta_Y + C_{Y\ell})/\delta \qquad \text{(h)}$$

$$D_3 = -(H_{Z_i} + Y\Delta_Z)/\Delta \qquad \text{(i)}$$

$$D_4 = -(H_{X_i} + Y\Delta_X)/\Delta \qquad \text{(j)}$$

This transformation is a modification of the one used previously by Moretti to solve numerical problems. (e.g. see reference 4) Singularities occur when $C_\ell = C_{\ell+1}$ or $H_i = H_{i+1}$ and when $J = 0$. The former occurs when two shocks intersect, this matter will be discussed in the section on "Treatment of Shocks". The latter case occurs when the mesh lines X = constant and Y = constant become parallel in the physical plane. This can occur for certain locations of cross flow shocks. However this problem can be overcome

by either modifying the conformal mappings so that the cross section in the mapped plane is "more circular" or using a cross flow shock type surface (which acts like an extension to a cross flow shock) to control the shape of the mesh lines.

All shocks are defined in the mapped plane as $r = \bar{c}(\theta,\not{2})$ and $\theta = h(r,\not{2})$ so that $\bar{C}(Y,Z) = \bar{c}\,[\theta(X_s,Y,Z),\not{2}]$, $H(X,Z)=h\,[r(X,Y_s,Z),\not{2}]$ (where X_s and Y_s are either 0 or 1) and their derivatives $\bar{C}_Y, \bar{C}_Z, H_X$ and H_Z must be calculated. The body is defined in the physical plane and an iterative procedure is needed to describe the body as $r = b(\theta,\not{2})$ from which $B(Y,Z)$ can be computed. From the derivatives b_θ, $b_{\not{2}}$, $\bar{c}_\theta$, $\bar{c}_{\not{2}}$, $h_{\not{2}}$ and h_r the calculation of B, $\bar{C}$, B_Z, and $\bar{C}_Z$ proceeds as follows.

Using the notation of equations (11 - 13) define

$$c_1 \equiv b(\theta,\not{2})$$

$$c_\ell \equiv \bar{c}_{\ell-1}(\theta,\not{2})$$

then

$$\begin{aligned} C_{X_\ell} &= c_{\theta_\ell}\,[H(X_s,Z)_{i+1} - H(X_s,Z)_i] \\ H_{X_i} &= h_{r_i}\,[C(Y_s,Z)_{\ell+1} - C(Y_s,Z)_\ell] \end{aligned} \tag{16}$$

Where again X_s (the value of X at the shock C_ℓ) and Y_s (the value of Y at the shock H_i) are 0 or 1.

$$\begin{aligned} C_{Z_\ell} &= c_{\not{2}_\ell} + c_{\theta_\ell}\,\theta_Z && \text{(a)} \\ \theta_Z &= Y[H_Z(X_s,Z)_{i+1} - H_Z(X_s,Z)_i] + H_Z(X_s,Z)_i && \text{(b)} \\ H_{Z_i} &= h_{\not{2}_i} + h_{r_i}\,r_Z && \text{(c)} \\ r_Z &= X[C_Z(Y_s,Z)_{\ell+1} - C_Z(Y_s,Z)_\ell] + C_Z(Y_s,Z)_\ell && \text{(d)} \end{aligned} \tag{17}$$

At the points $X = X_s$ and $Y = Y_s$ at a cross section Z these equations result in a set of simultaneous linear equations for $H_Z(X_s,Z)$ and $C_Z(Y_s,Z)$.

$$C_Z(Y_s,Z)_{\ell} = \frac{c_{\theta_{\ell}} \left[Y_s \left(h_{\mathcal{Z}_{i+1}} - h_{\mathcal{Z}_i} \right) - h_{\mathcal{Z}_i} \right] + c_{\mathcal{Z}_{\ell}}}{1 - c_{\theta_{\ell}} \left[Y_s \left(h_{r_{i+1}} - h_{r_i} \right) - h_{r_i} \right]} \tag{18}$$

where as $H_Z(X_s,Z)$ can be computed from equations (16). For all other points equations (16) are used to compute $C_Z(Y,Z)$ and $H_Z(X,Z)$.

Now the computational plane and its boundaries are completely defined so that for any mesh point (X,Y,Z) in the computational plane the corresponding point (x,y,z) in the physical plane and all the necessary transformation derivatives can be computed.

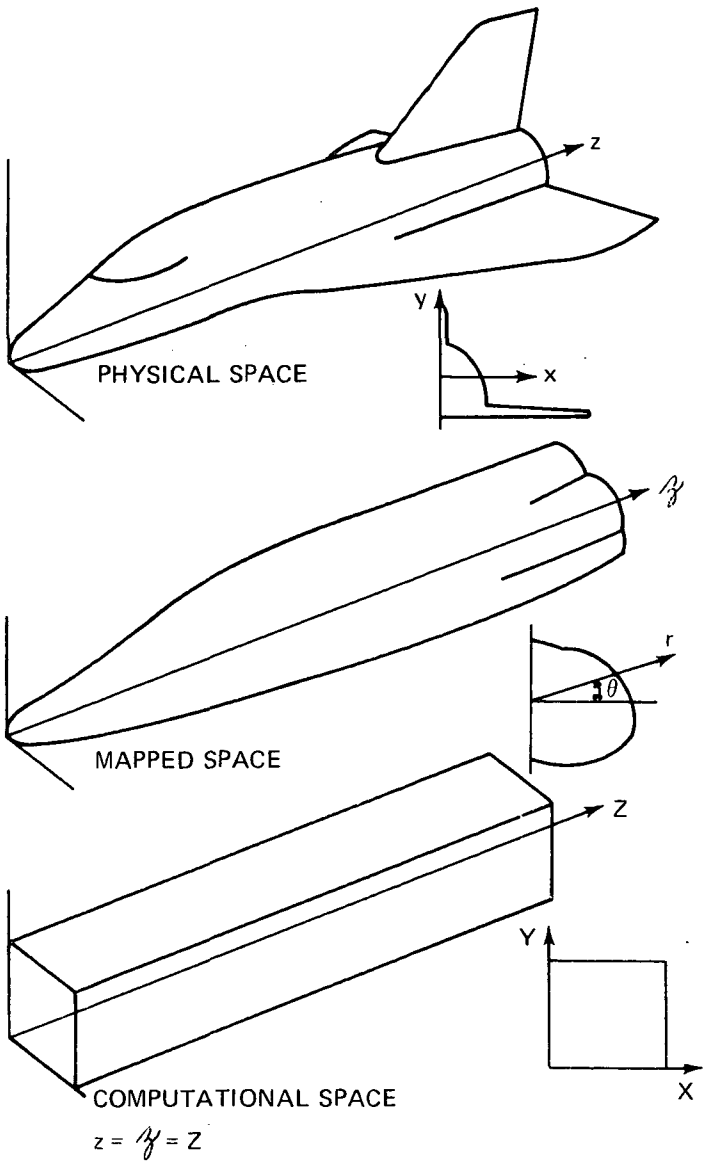

Figure 6. - Three coordinate systems/spaces used.

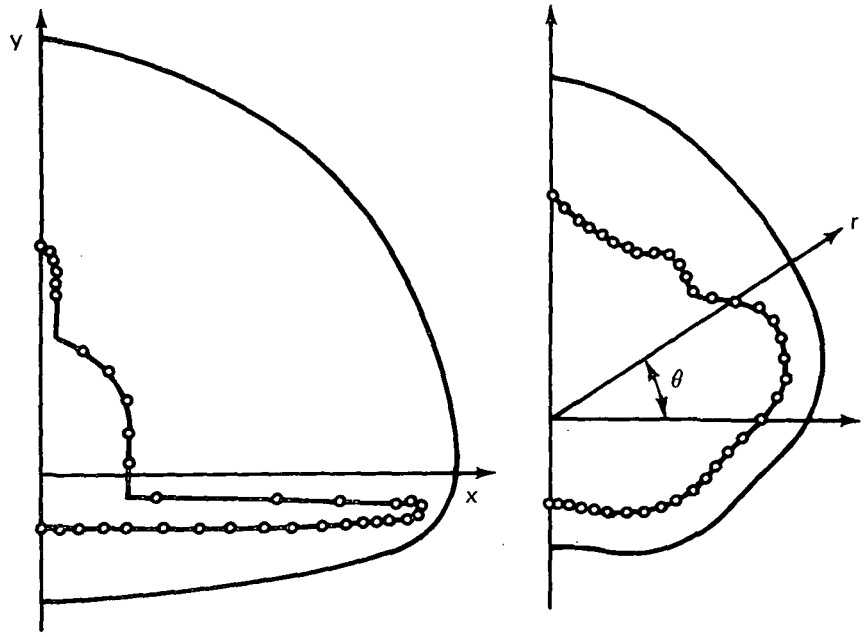

Figure 7. - Body mesh point distribution.

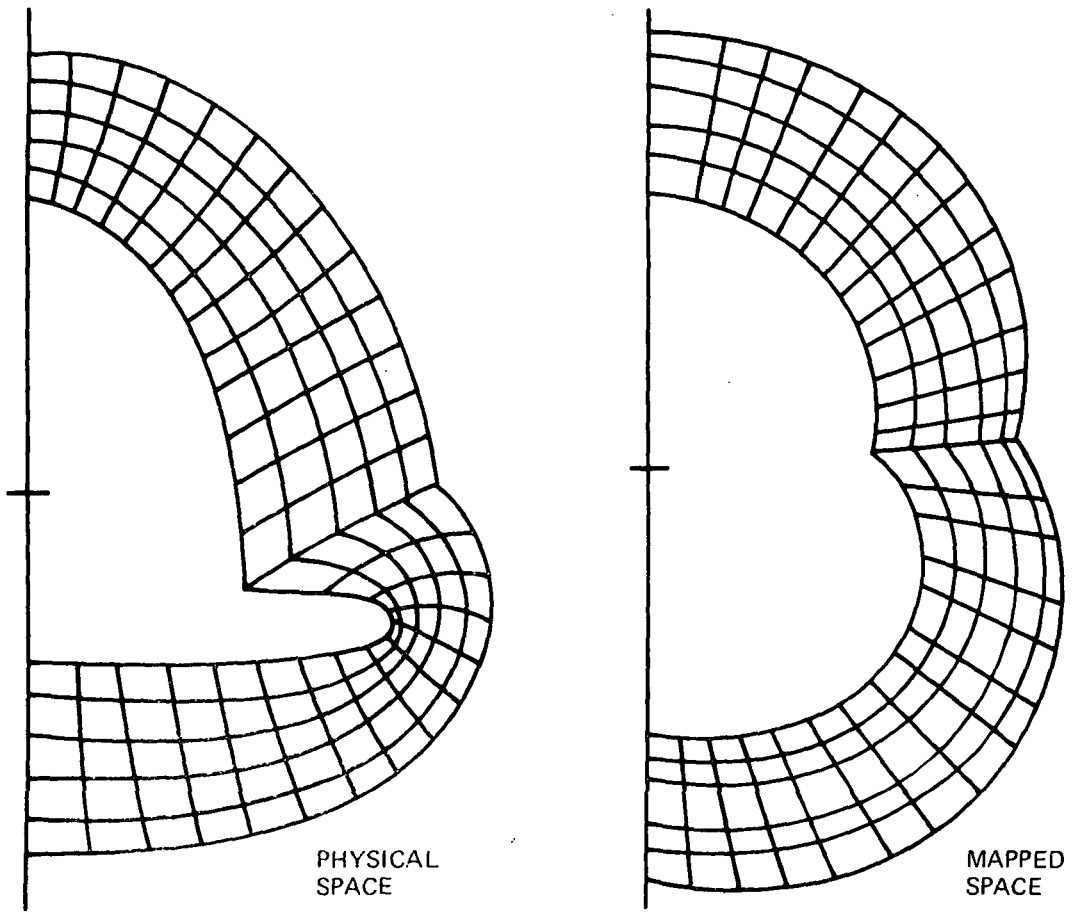

Figure 8. - Grid lines (near the body).

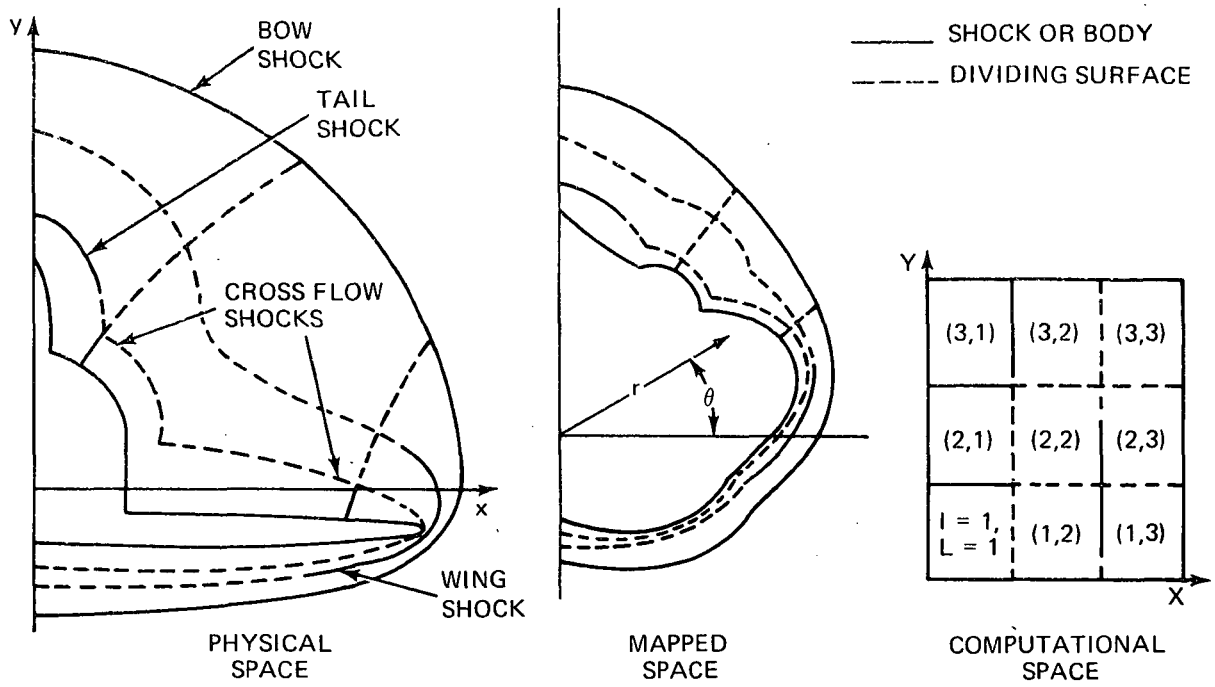

Figure 9. - Plane Z = Constant in the physical, mapped and computational spaces.

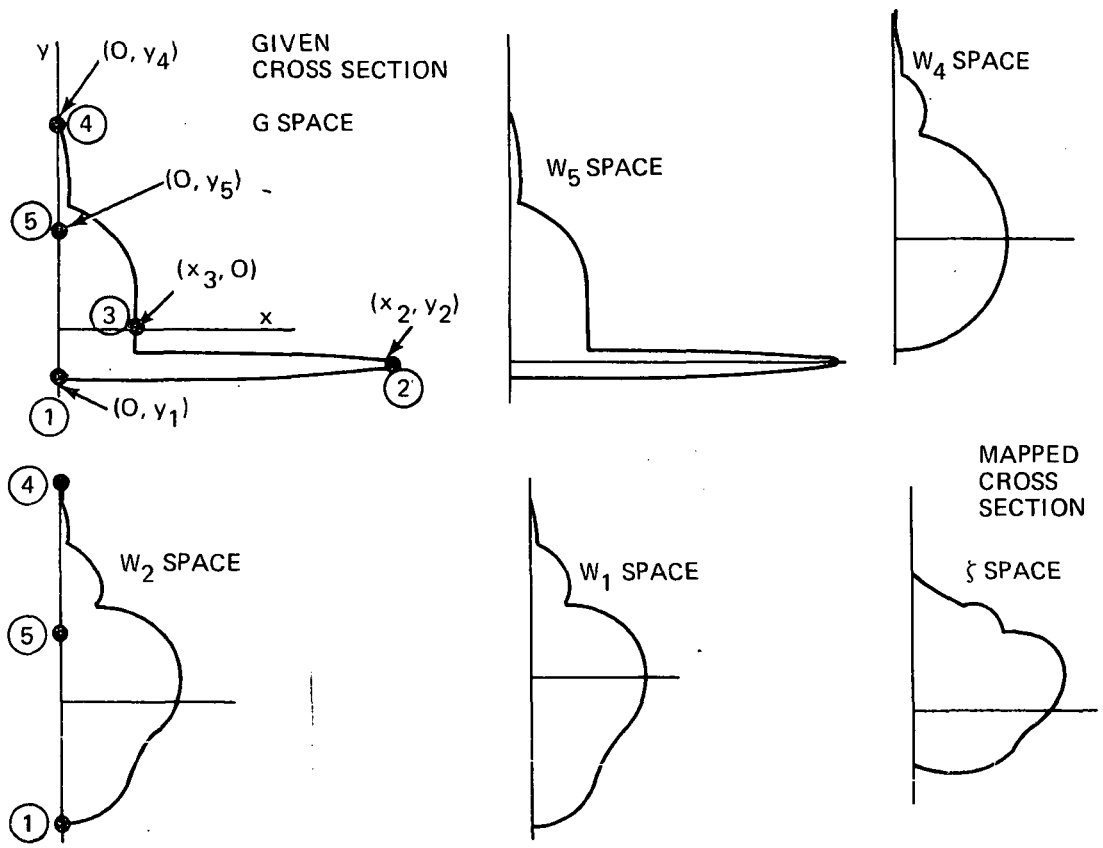

Figure 10. - Series of mappings.

COMPUTATION OF REGIONS OF CONTINUOUS FLOW

In the physical plane (x,y,z) the Euler equations are:

$$
\begin{aligned}
wP_z + \gamma w_z &= -(uP_x + vP_y + \gamma u_x + \gamma v_y) && \text{(a)}\\
wu_z &= -(uu_x + vu_y + TP_x) && \text{(b)}\\
wv_z &= -(uv_x + vv_y + TP_y) && \text{(c)}\\
TP_z + ww_z &= -(uw_x + vw_y) && \text{(d)}\\
wS_z &= -(uS_x + vS_y) && \text{(e)}
\end{aligned}
\qquad (19)
$$

where $T = \bar{T}/\bar{T}_\infty$, $P = \ln(\bar{p}/\bar{p}_\infty)$, $S = (\bar{S}-\bar{S}_\infty)/c_{v_\infty}$ and all velocities are non-dimensionalized with respect to $\bar{p}_\infty/\bar{\rho}_\infty$ (the barred quantities are dimensional), $x = \bar{x}/\bar{\ell}$, $y = \bar{y}/\bar{\ell}$, $z = \bar{z}/\bar{\ell}$ ($\bar{\ell}$ is an arbitrary length),

The equation of state for an ideal gas becomes:

$$\ln(T) = P\,\frac{(\gamma-1)}{\gamma} + \frac{S}{\gamma} \qquad (20)$$

The dependent variables are P,S and the Cartesian velocity components u,v,w (Fig. 4). Now transforming all derivatives to the computational plane the following results are obtained.

$$
\begin{aligned}
f_x &= f_X X_x + f_Y Y_x + f_Z Z_x && \text{(a)}\\
f_y &= f_X X_y + f_Y Y_y + f_Z Z_y && \text{(b)}\\
f_z &= f_X X_z + f_Y Y_z + f_Z Z_z && \text{(c)}
\end{aligned}
\qquad (21)
$$

where f is the vector (P,u,v,w,S) and

$$X_x = X_r r_x + X_\theta \theta_x + X_z z_x \qquad (a)$$

$$X_y = X_r r_y + X_\theta \theta_y + X_z z_y \qquad (b) \qquad (22)$$

$$X_z = X_r r_z + X_\theta \theta_z + X_z z_z \qquad (c)$$

Similar expressions can be written for the Y and Z derivatives. The derivatives of (X,Y,Z) with respect to (r,θ,z) and (r,θ,z) with respect to (x,y,z) have already been discussed in the previous section.

Combining equations (19a) and (19e) the following form of the Euler equations is obtained which are used in the present solution.

$$P_Z = (a_{11}P_X + a_{12}u_X + a_{13}v_X + a_{14}w_X + b_{11}P_Y + b_{12}u_Y + b_{13}v_Y + b_{14}w_Y) \qquad (a)$$

$$u_Z = -(a_{21}P_X + a_{22}u_X + b_{21}P_Y + b_{22}u_Y) \qquad (b)$$

$$v_Z = -(a_{31}P_X + a_{33}v_X + b_{31}P_Y + b_{33}v_Y) \qquad (c) \qquad (23)$$

$$w_Z = -(a_{41}P_X + a_{42}u_X + a_{43}v_X + a_{44}W_X + b_{41}P_Y + b_{42}u_Y + b_{43}v_Y + b_{44}w_Y) \qquad (d)$$

$$S_Z = -(a_{55}S_X + b_{55}S_Y) \qquad (e)$$

where the coefficients appearing in equations (23) are defined in Appendix B.

At a data plane, $Z = Z_o$ = constant, all the quantities on the right side of equations (23) are known and therefore the derivative f_Z can be computed and used to predict the dependent variables at $Z = Z_o + \Delta Z$.

The step size ΔZ in the marching direction must satisfy the C.F.L. condition for stability (ref. 13). If $\lambda_{X\pm}$ are the characteristic slopes in the X,Z plane and $\lambda_{Y\pm}$ are the characteristic slopes in the Y,Z plane the stability criterion is written as follows:

$$\Delta Z_{X+} = \Delta X/\lambda_{X+} \qquad \Delta Z_{Y+} = \Delta Y/\lambda_{Y-} \qquad (24)$$

$$\Delta Z_{X-} = \Delta X/\lambda_{X-} \qquad \Delta Z_{Y-} = \Delta Y/\lambda_{Y-}$$

Each of these quantities is evaluated for every mesh point at the station $Z = Z_o$, and ΔZ is taken as 70% of the minimum of all of these ΔZ values.

A modified MacCormack, two-level, predictor-corrector finite-difference scheme (ref. 14) is used to integrate equations (23). It can be proven that the MacCormack scheme is accurate to second order for a linear system of equations. So that the truncation error is of the form.

$$\frac{\partial^2 f}{\partial \ell^3} \Delta \ell^3$$

where ℓ is a length in the physical plane. In regions where $\partial^3 f/\partial \ell^3$ is large the mappings tend to assure $\Delta \ell \to 0$ so that the truncation error remains small, while keeping the total number of grid points to a minimum.

Equations (23) can be written in the following general form

$$f_Z = [A]f_X + [B]f_Y \tag{25}$$

where as previously defined f is the vector (P,u,v,w,S) and [A] and [B] are matrices of the coefficients of equations (23). With these equations the MacCormack scheme proceeds as follows.

Level one:

$$f_Z(Z_o) = [A]f_X + [B]f_Y \quad \text{(all quantities evaluated at } Z_o\text{)} \tag{a}$$

$$\tilde{f} = f(Z_o) + f_Z(Z_o)\,\Delta Z \quad (\tilde{f} \text{ is the predicted value}) \tag{b}$$

Level two: (26)

$$\tilde{f}_Z = [\tilde{A}]\,\tilde{f}_X + [\tilde{B}]\tilde{f}_Y \quad \text{(all dependent variables evaluated with the predicted values and all independent variables are evaluated at } Z = Z_o + \Delta Z\text{)} \tag{c}$$

$$f(Z_o + \Delta Z) = (\tilde{f} + f(Z_o) + \tilde{f}_Z \Delta Z)/2 \tag{d}$$

The f_X derivatives are taken one sided in the positive X-direction in level one, the f_Y derivatives in the positive Y-direction. For level two the direction of these derivatives is reversed.

This procedure defines all the dependent variables at interior points of the computational plane (1<NN<NC(L) and 1<MM<MC(I)); figure 11. The body point calculation and the shock point calculation will be discussed later. However, note here that all imbedded shock points have two mesh points associated with them, one for the low pressure side and one for the high pressure side, both having the same position in the physical plane (Fig. 11). The low pressure side of all shocks are computed following the MacCormack scheme and taking X and Y derivatives into the low pressure region in both levels. The low pressure side of the bow shock ((NN = NC(L), L = LC)) is defined by the given free stream conditions.

The points on the symmetry planes (MM = 1, I = 1 and MM = MC(I), I = IC) are computed using the same scheme and the symmetry conditions $P_Y = v_Y = w_Y = S_Y = 0$ and $u = 0$. The points on the internal boundaries that are not shock points are also computed using the MacCormack scheme. In level one the points NN=1 and MM=1 are computed, taking the difference between NN=1, NN=2 and MM=1, MM=2 for the X and Y derivatives respectively. After level one quantities at NC(L) and MC(L) are updated (i.e., $f(NC(L),M)_L = f(1,M)_{L+1}$ and $f(N,MC(I))_I = f(N,1)_{I+1}$). In level two the points on the other side of the surfaces NN = NC(L) and MM = MC(I) are computed and afterward the points NN=1 and MM=1 are updated.

The modifications to MacCormack's integration scheme were originally found necessary in the calculation of blunt nose bodies. For blunt nose bodies derivatives across the "edge" of the entropy layer are not allowed. The entropy layer calculation will be discussed later, for now assume the position of a surface X = F(Y,Z) representing, in the computational plane, the edge of the entropy layer, (Fig. 12a) and all dependent variables on this surface are known. Across this surface the derivatives S_X, u_X, v_X and w_X become very large as the surface approaches the body. In computing these derivatives at the mesh point N of figure 12b, instead of taking the X derivatives between points N and N + 1 differences are taken between N and the * point which is on the entropy layer

surface. If the entropy layer surface point becomes very close to the mesh point (Fig. 12c) the dependent variables at N are set equal to those computed at the entropy layer surface point since the distance between N and * is too small to compute S_X, u_X, v_X and w_X between them.

In order to calculate the flow field over bodies with blunt nose entropy layers it was found necessary to use "windward" differencing. Equations (23b, c, and e) state the variation of u, v and S along a streamline, i.e., the velocity direction is the characteristic direction of these equations. Accordingly, for the derivatives v_X, u_X and S_X in these equations, differences are taken in a direction determined by the velocity direction in both levels of the MacCormack scheme (Fig. 13); the same is true for v_Y, u_Y and S_Y. If the slope β_X and/or β_Y of the velocity vector is small the derivative direction is changed between level one and two as usual. Since in equations (23b, c, and e) information is carried along streamlines, windward differences satisfy the rule of the domain of influence, so that windward differences are used even when there is no blunt nose entropy layer in the computation. The techniques of following the entropy layer and using windward differences were originally suggested by Moretti and Pandolfi (refs. 7 and 8). When derivatives are approximated with windward differencing they are no longer formally second order accurate. But it was found that windward differencing yields more stable results and the integration scheme was found to be second order accurate in a numerical experiment.

The calculation of interior points is the most time consuming part of this computation mainly because it is done many times. The scheme used here keeps the computational time to a minimum by keeping the total number of mesh points as small as possible.

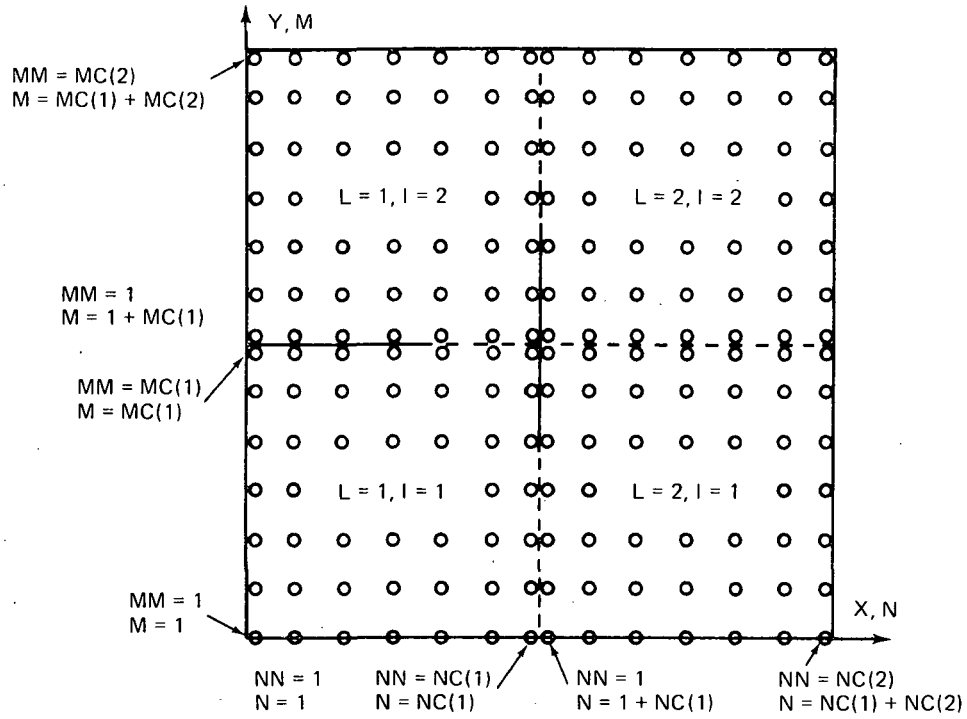

Figure 11. - Region and mesh point notation.

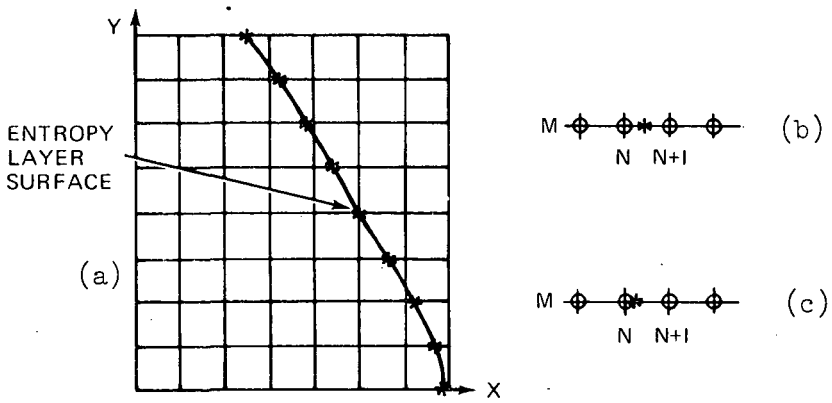

Figure 12. - Entropy layer surface (computational space).

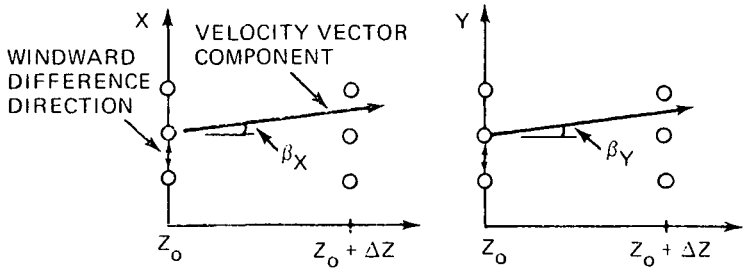

Figure 13. - Windward differencing scheme.

TREATMENT OF SHOCKS

In this section the computation of grid points on the high pressure side of all shock waves, the detection of imbedded shocks and the intersection of two same family shocks will be discussed. In this area we draw systematically from Moretti's extensive research on the treatment of shock waves (ref. 1 and 6).

The bow shock, all wing type shocks (i.e., imbedded shocks which in general originate near the body and move toward the bow shock, caused by canopies, wings and vertical tails) and cross flow shocks in the flow field are computed as discontinuities satisfying the Rankine-Hugoniot conditions. The bow shock and wing type shocks are defined in the mapped plane by $r = \bar{c}(\theta,\ell)$ and the crossflow shocks by $\theta = h(r,\ell)$. At a data plane Z_o all dependent variables are known, and in addition, the quantities $\bar{c}$, $\bar{c}_\theta$, $\bar{c}_\ell$, h, h_r, h_ℓ are also known. Using equations (16) to (18) $C(Y,Z_o)$, C_Y, C_Z, $H(X,Z_o)$, H_X and H_Z are computed for all the shocks in the flow field. At $Z_o + \Delta Z$ the positions of the shock points can be computed by using;

$$C(Y,Z_o + \Delta Z) = C(Y,Z_o) + C_Z(Y,Z_o)\,\Delta Z \qquad \text{(a)}$$

$$H(X,Z_o + \Delta Z) = H(X,Z_o) + H_Z(X\,Z_o)\,\Delta Z \qquad \text{(b)} \qquad (27)$$

Then $C_Y(Y,Z_o + \Delta Z)$ and $H_X(X,Z_o + \Delta Z)$ are computed using central differences. With these quantities and equations (16) $\bar{c}$, $\bar{c}_\theta$, h and h_r can be computed at $Z = Z_o + \Delta Z$.

After the first level of the MacCormack scheme the predicted values of the dependent variables on the low pressure side of all shocks are computed (the variables on the low pressure side of the bow shock being the constant free stream values). With the low pressure side of the shocks known the high pressure side is computed by an iterative process.

A value of h_2 or $\bar{c}_2$ is guessed, between the values corresponding to an infinitely weak shock and the value which gives a subsonic axial Mach number. Once this guess is made the normal to the shock can be defined. Let

$$F \equiv r - \bar{c}(\theta, z_2)$$

or

$$F \equiv \theta - h(r, z_2)$$

Then the normal to the shock $\hat{I}$ is given by:

$$\hat{I} = (F_x \hat{i} + F_y \hat{j} + F_z \hat{k}) / \sqrt{F_x^2 + F_y^2 + F_z^2} = I_1 \hat{i} + I_2 \hat{j} + I_3 \hat{k}$$

where

$$F_x = F_r r_x + F_\theta \theta_x + F_{z_2} z_{2x}$$

$$F_y = F_r r_y + F_\theta \theta_y + F_{z_2} z_{2y}$$

$$F_z = F_r r_z + F_\theta \theta_z + F_{z_2} z_{2z}$$

With the normal to the shock defined, the Rankine-Hugoniot conditions can be applied. Using the subscripts 1 for the low pressure side and 2 for the high pressure side we have:

$$V_{n_1} = \vec{V}_1 \cdot \hat{I} \qquad \text{(a)}$$

$$M_{n_1} = V_{n_1} / \sqrt{\gamma T_1} \qquad \text{(b)}$$

$$\rho_2/\rho_1 = [M_{n_1}^2 (\gamma+1)/2.]/[1 + M_{n_1}^2 (\gamma-1)/2.] \qquad \text{(c)} \qquad (28)$$

$$p_2/p_1 = [(\gamma+1)/(\gamma-1)\rho_2/\rho_1 - 1.]/[(\gamma+1)/(\gamma-1) - \rho_2/\rho_1] \qquad \text{(d)}$$

$$T_2/T_1 = [T_1(p_2/p_1)]/(\rho_2/\rho_1) \qquad \text{(e)}$$

$$\vec{V}_2 = \vec{V}_1 - V_{n_1} \hat{I} \qquad \text{(f)}$$

Where M_n and V_n are the Mach number and velocity normal to the shock and $\vec{V}_T$ is the velocity tangent to the shock.

An intrinsic coordinate system is defined at the shock with the three directions $(\hat{I},\hat{J},\hat{K})$, coordinates (ξ,η,ω) and velocities $(\tilde{u},\tilde{v},\tilde{w})$ such that $\hat{I}$ is normal to the shock and:

$$\hat{K} = (\hat{I} \times \hat{k})/|\hat{I} \times \hat{k}| = K_1 \hat{i} + K_2 \hat{j} + K_3 \hat{k}$$

$$\hat{J} = \hat{I} \times \hat{K} = J_1 \hat{i} + J_2 \hat{j} + J_3 \hat{k}$$

In the ξ,ω plane the characteristic that intersects the shock from the high pressure side has a slope

$$\frac{d\xi}{d\omega} = \lambda = \frac{(\tilde{u}\tilde{w} + a\sqrt{\tilde{u}^2 + \tilde{w}^2 - a^2})}{(\tilde{w}^2 - a^2)} \qquad (29)$$

Figure 14 shows the shock, characteristic (in the ξ,ω plane) and the point (*) in the Z_o data plane where the characteristic originates. The characteristic slope at the shock point is first evaluated and then the position of the (*) point is computed using the relations:

$$\omega^* = -\Delta Z/(K_3 + \lambda I_3) \qquad (a)$$

$$\xi^* = \lambda\,\omega^* \qquad (b)$$

$$x^* = x_{SH} + \xi^* I_1 + \omega^* K_1 \qquad (c) \qquad (30)$$

$$y^* = y_{SH} + \xi^* I_2 + \omega^* K_2 \qquad (d)$$

Where the subscript SH refers to quantities at the shock at $Z + \Delta Z$ (Fig. 14). Dependent variables at the (*) point are obtained by linear interpolation. A value of the pressure on the high pressure side of the shock is computed using the compatibility equation along the characteristic:

$$\beta = \gamma\tilde{w}^2/[a\sqrt{\tilde{u}^2+\tilde{w}^2-a^2} \qquad (a)$$

$$\lambda = (\tilde{u}\,\tilde{w} + a\sqrt{\tilde{u}^2+\tilde{w}^2-a^2})/(\tilde{w}^2-a^2) \qquad (b)$$

$$R = \frac{[(\tilde{u}-\lambda\tilde{w})(\tilde{v}P_\eta + \gamma\tilde{v}_\eta) - \gamma\tilde{v}\tilde{u}_\eta \quad \gamma\tilde{v}\tilde{w}_\eta]}{a\sqrt{\tilde{u}^2+\tilde{w}^2-a^2}} \qquad (c) \qquad (31)$$

$$d\tau = \tilde{u}^*/\tilde{w}^* - \tilde{u}_{SH}/\tilde{w}_{SH} \qquad (d)$$

$$P_{SH} = P^* + R\omega^* - \beta d\tau \qquad (e)$$

$$p_2 = e^{P_{SH}} \qquad (f)$$

Where β,λ, and R are averaged between the * point and the shock point. The iteration is continued until this value of pressure agrees with that computed from the Rankine-Hugoniot conditions, for some value of $\bar{c}_2$ or h_2. For weak shocks this iteration may converge to a pressure ratio $p_2/p_1 < 1$, in these cases the value of $\bar{c}_2$ or h_2 which gives $p_2/p_1 = 1$ is taken.

Cross flow shock points at the body must satisfy the body boundary condition, that is the velocity normal to the body on the high pressure side of the shock must vanish. This implies that the shock normal, at the body, must be perpendicular to the body normal. This condition gives a relationship between h_2 and h_r at the body:

$$h_r = (F_H - h_2 F_{Bz})/F_r \qquad (32)$$

Where:

$$F_H = F_{Bx}\theta_x + F_{By}\,\theta_y + F_{Bz}\theta_z$$

$$F_r = F_{Bx}\,r_x + F_{By}\,r_y + F_{Bz}\,r_z$$

and F_{Bx}, F_{By}, F_{Bz} are x, y, z derivatives

of $F_B = r - b(\theta, \ell)$

and $r = b(\theta, \ell)$ defines the body.

After the second level of the MacCormack scheme the corrected, final values of the dependent variables on the low pressure side of the imbedded shocks, the values of $\bar{c}_\ell$ and h_ℓ computed after the first level, and the Rankine-Hugoniot conditions are used to compute the final values of the dependent variables on the high pressure side of the shocks.

The first problem encountered when one treats imbedded shocks as discontinuities is their detection. There have been a number of techniques proposed (see ref. 6). One of the earliest procedures has been found to be well suited for the type of shocks encountered in this problem.

Cross flow shocks and wing type shocks are detected in very similar ways. For cross flow shocks, the pressure distribution is monitored in the Y-direction and for wing type shocks the pressure distribution is monitored in the X-direction. At a data plane $Z = Z_o$ the maximum pressure gradient P_X for wing type shocks and P_Y for crossflow shocks is located. Then a third order polynomial is fit through the four mesh points adjacent to the maximum gradient (Fig. 15). This polynomial takes the form:

$$X = a_o P^3 + a_1 P^2 + a_2 P + a_3 \tag{33}$$

Where (X = X for wing type shocks)

(X = Y for cross flow shocks)

and the coefficients a_o, a_1, a_2 and a_3 are computed by matching the curve fit to the four mesh points (Fig. 15). The condition used to determine the origin of a shock is $dX/dP = 0$ which implies $dP/dX \to \infty$. Applying this condition to equation (33) yields an equation for P_f of the form:

$$P_f = \frac{-a_1 \pm \sqrt{a_1^2 - 3 a_o a_2}}{a_o}$$

When $\sqrt{a_1^2 - 3a_0a_2} = 0$. This equation has one real root. When this condition is satisfied a shock is inserted in the flow field at $X_f = a_0P_f^3 + a_1P_f^2 + a_2P_f + a_3$.

Cross flow shocks are assumed to originate on the body, so that the pressure distribution is monitored in the Y-direction on X = 0 (the body). Once a shock is found on the body monitoring is begun at increasing values of X = constant.

In general it is not known at what value of Y the first shock point on a wing type shock will be found so that the maximum pressure gradient P_X at all values of Y must be tested until the first shock point is detected. Once a wing type shock is detected additional shock points are sought at the grid points adjacent to the end shock points (Fig. 16).

Finally, consider the intersection of two shocks of the same family. Cross flow shocks do not move very much (i.e., h_2 is small) so that a scheme to handle the intersection of two crossflow shocks is not needed. Wing type shocks are detected near the body (they are usually caused by compressions on the body) and they move toward the bow shock, so that they are all of the "same family". As a shock moves toward the bow shock the region between the imbedded shock and the body gets larger and the region between the imbedded shock and the bow shock gets smaller so that mesh points must be moved from the outside region to the inside region. When the distance between two shocks becomes a small percent of the total shock layer (1 to 5%) at some value of Y (Fig. 17) the two shocks are intersected. A local, exact, two dimensional calculation is used to compute the intersection of two shocks. The same intrinsic coordinate system is used as was discussed in the shock point computation, where $\hat{I}$ is normal to the outside shock. In the ξ,ω plane the intersection of two same family shocks is shown in Fig. 18. The conditions in regions 1 and 4 (Fig. 18) are known. The slope $\bar{c}_2$ of the resulting shock is assumed and Rankine-Hugoniot conditions (28) and the conditions in region 1 are used to compute the conditions in region 2. The pressure in region 3 is set equal to that in region 2 (since the pressure is

constant across a contact surface) and the total pressure in region 3 equal to that of region 4 (since the total pressure is constant through an expansion fan). With the pressure and the total pressure in region 3 the Mach number can be computed. Then from the Prandtl-Meyer expansion relation the flow direction δ_3 is obtained. The iteration is continued until the velocity direction δ_3 matches that computed in region 2.

All the iterations follow the same procedure. Assume we have two functions of a single variable $g(\eta)$ and $G(\eta)$. The problem is to find the value of η for which $g = G$. Two values of η are assumed and two errors ($\epsilon_1 = g_1 - G_1$) and ($\epsilon_2 = g_2 - G_2$) are computed. With $\epsilon_1, \epsilon_2, \eta_1$ and η_2 a linear variation of ϵ vs η is assumed to predict the value of η which will force $\epsilon \to 0$.

$$\eta_3 = \eta_1 - \epsilon_1 (\eta_2 - \eta_1)/(\epsilon_2 - \epsilon_1)$$

The assumed value is repeatedly updated in this manner until $\epsilon \to 0$. This scheme was found simple and fast and in most cases it converges in 4-5 iterations.

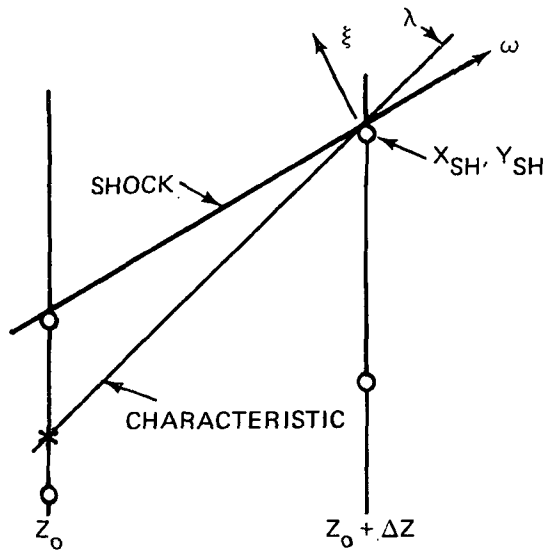

Figure 14. - Shock point calculation.

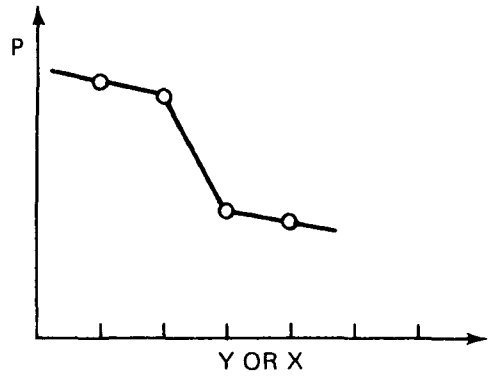

Figure 15. - Four mesh points used in shock detection.

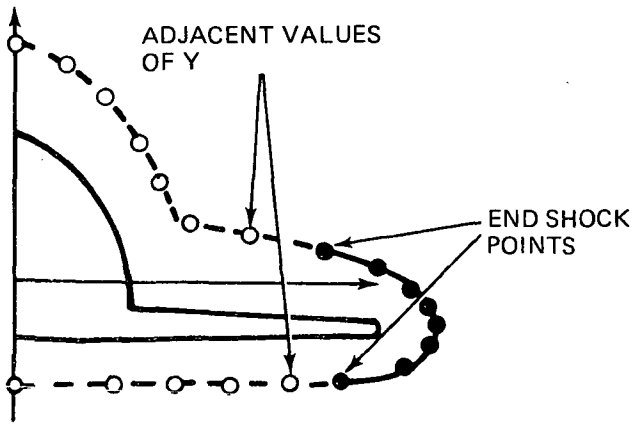

Figure 16. - End shock points (wing type shocks).

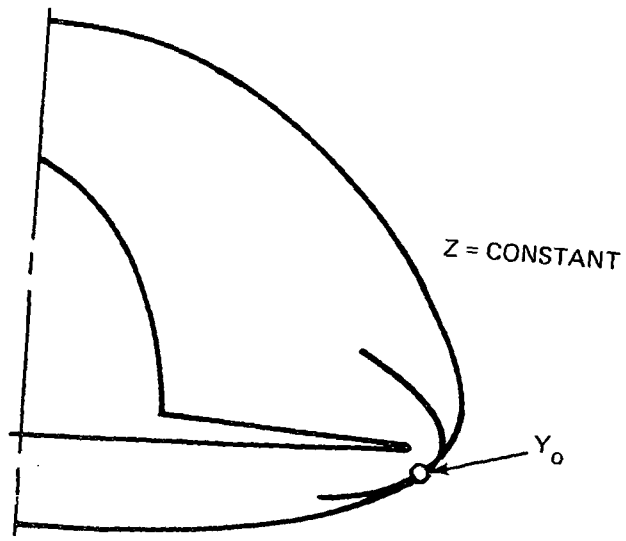

Figure 17. - Shock intersection in Z = constant plane.

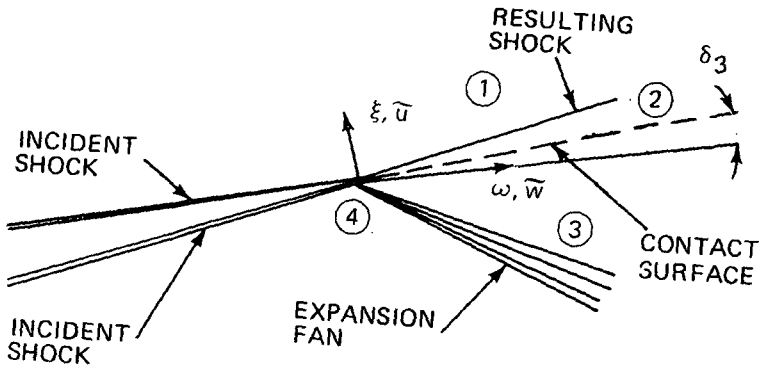

Figure 18. - Shock intersection, local two dimensional (ξ, ω plane) calculation.

SHARP LEADING EDGE SHOCKS

When a configuration has a sharp leading edge wing (Fig. 19) its wing leading edge is computed using a local two dimensional solution. The component of the Mach number normal to the leading edge must be supersonic in order for this technique to be applied. Also the wing must be sharp from the root.

The mesh point distribution near a sharp tip is shown in figure 20. The mappings are not modified for this type of configuration but a cross flow type surface is inserted starting at the wing tip, in order to have a double point at the tip, on the top and bottom of the wing.

The shock points at the tip (the case of an expansion fan on one side and a shock on the other can be handled) are automatically inserted when the wing starts. All other points on this shock are detected as in the case of a blunt nose wing. The extensions of the shock are treated as discussed previously. If the flow direction is such that there is a centered expansion fan on the top or bottom of the wing (Fig. 20), the expansion is computed explicitly at the tip point, and an arbitrary surface is used from the tip to the symmetry plane. Thus, the expansion fan is computed using the finite difference scheme for all points except the one at the tip.

The calculation of the tip points utilizes an intrinsic frame of reference $(\xi,\eta,\omega),(\tilde{u},\tilde{v},\tilde{w})$ defined in figure 21. The η direction is tangent to the sharp edge of the wing (hence, also tangent to the shock) so that $\tilde{v}$ remains unchanged across the shock. In the ξ,ω plane, a local two dimensional wedge calculation is performed. The conditions on the low pressure side of the shock are known. A third order algebraic equation (ref. 15) is used to compute β, the shock angle, and then the Rankine-Hugoniot jump conditions are used to compute the dependent variables on the high pressure side of the shock. If the flow is such that there is a centered expansion fan at the tip point the Prandtl-Meyer expansion fan equations are used to compute the dependent variables on the body surface. This calculation is done after each level of the McCormack scheme.

This method will not handle the situation in which the Mach number normal to the leading edge of the wing is subsonic or the situation in which the wing angle (δ, Fig. 21) is large enough to force the shock to be detached.

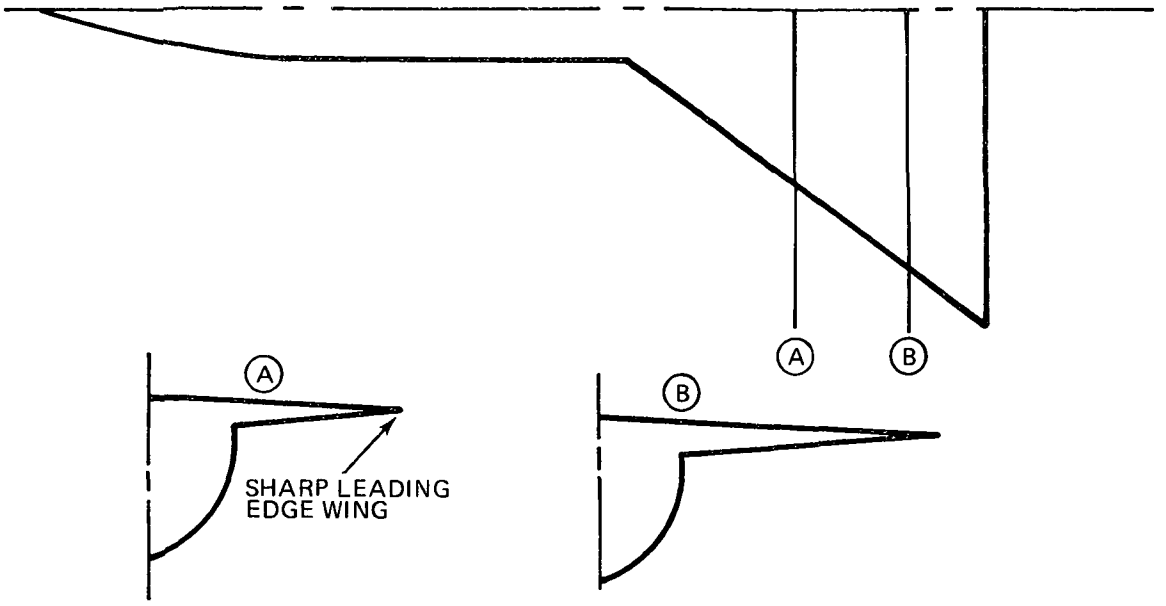

Figure 19. - Sharp leading edge wing configuration.

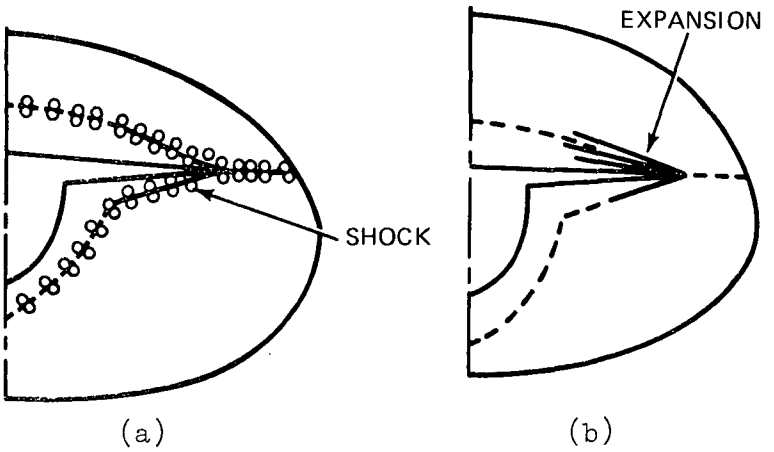

Figure 20. - Mesh point distribution, sharp leading edge wing.

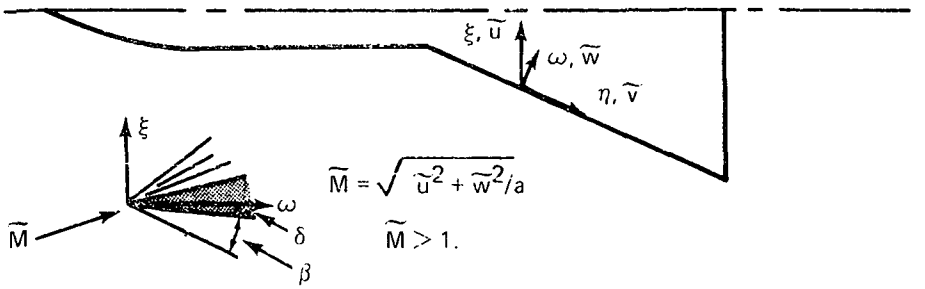

Figure 21. - Sharp leading edge wing intrinsic frame.

BODY POINT COMPUTATION

The boundary condition at the vehicle surface is $\tilde{u} = 0$, where $\tilde{u}$ is the velocity normal to the body. The entropy at the body is computed by using equation (23e), as for any other mesh point. At the body the coefficient of S_X (i.e., a_{55}) in equation (23e) vanishes, so that this derivative does not affect the calculation of entropy on the body.

To compute the pressure on the body the continuity and three momentum equations (23a, b, c, and d) and the body boundary condition are combined to write a compatability equation along the characteristic (in the X,Z plane) reaching the wall from the flow field.

$$
\begin{aligned}
&P_Z + a_{11}P_X + a_{12}\,u_X + a_{13}v_X + a_{14}\,w_X = R_1 && \text{(a)}\\
&u_Z + a_{21}P_X + a_{22}\,u_X = R_2 && \text{(b)}\\
&v_Z + a_{31}P_X + a_{33}\,v_X = R_3 && \text{(c)}\\
&w_Z + a_{41}P_X + a_{42}\,u_X + a_{43}\,v_X + a_{44}\,w_X = R_4 && \text{(d)}
\end{aligned}
\qquad (34)
$$

where

$$R_1 = -(b_{11}P_Y + b_{12}u_Y + b_{13}v_Y + b_{14}w_Y)$$

$$R_2 = -(b_{21}P_Y + b_{22}u_Y)$$

$$R_3 = -(b_{31}P_Y + b_{33}v_Y)$$

$$R_4 = -(b_{41}P_Y + b_{42}u_Y + b_{43}u_Y + b_{44}w_Y)$$

Substituting for a_{12}, a_{13} and a_{14} equation (34a) becomes

$$P_Z + a_{11}P_X + \frac{w^2 v_X}{A_1}\tau_X + \frac{w^2 v_Y}{A_1}\sigma_X = R_1 \qquad (35)$$

where:

$$\tau = u/w \text{ and } \sigma = v/w$$

Taking the difference between the product of w with equation (34b) and u with equation (34b) and substituting for a_{33}, a_{43}, a_{42} and a_{44} the following result is obtained.

$$w^2\tau_Z + P_X(wa_{21} - ua_{41}) + w^2\left(X_z + \frac{X_x\tau w^2}{A_1} - X_y\sigma\right)\tau_X + \frac{w^2\tau\gamma T}{A_1} X_y\sigma_X = wR_2 - uR_4 \tag{36}$$

Similarly, taking the difference between the product of w with equation (34c) and v with equation (34d) and substituting for a_{33}, a_{43}, a_{42} and a_{44} the following result is obtained

$$w^2\sigma_Z + P_X(wa_{31} - va_{41}) + w^2\left(X_z + \frac{X_y\sigma w^2}{A_1} + X_x\tau\right)\sigma_X + \frac{w^2\sigma\gamma T}{A_1} X_x\tau_X = wR_3 - vR_4 \tag{37}$$

The body boundary condition is $\tilde{u} = 0$. Since X = constant is the body, this boundary condition can be written as

$$\tilde{u} = uX_x + vX_y + wX_z = 0$$

or

$$\tau X_x + \sigma X_y + X_z = 0 \tag{38}$$

Combining equations (35), (36), and (37) and using equation (38) the equation for the characteristic slopes can be written in the form

$$\lambda_{\pm} = \frac{-a_{14}T}{w} \pm \sqrt{\frac{a_{14}^2T^2}{w^2} + \frac{\gamma T}{A_1}\left[\frac{\left(vX_y + uX_x\right)^2}{w^2} + X_y^2 + X_x^2\right]} \tag{39}$$

λ_- is the slope of the characteristic reaching the wall from the flow field and the compatibility condition along this characteristic is:

$$\left[\lambda - \frac{\gamma T}{A_1 w}\ (uX_x + vX_y)\right]\ (P_Z + \lambda P_X)$$

$$+ \frac{w^2\gamma}{A_1}\ (X_x\tau_Z + X_y\sigma_Z) + \frac{w^2\gamma\lambda}{A_1}\ (X_x\tau_X + X_y\sigma_X) = \frac{R}{\lambda} \qquad (40)$$

where

$$R = \left(\lambda - \frac{\gamma T}{A_1 w}\ (uX_x + vX_y)\right) R_1$$

$$+ \frac{X_x\gamma\lambda}{A_1}\ (wR_2 - uR_4) + \frac{X_y\gamma\lambda}{A_1}\ (wR_3 - uR_4)$$

The equation for the body can be written in the form

$$F = r - B(Y,Z) \qquad (41)$$

Thus the body boundary condition is

$$\tau F_x + \sigma F_y + F_z = 0 \qquad (42)$$

This equation holds for all values of Z, thus

$$\sigma_Z F_y + \tau_Z F_x = -\ (F_{zZ} + \sigma F_{yZ} + \tau F_{xZ}) = \bar{R} \qquad (43)$$

Now using equation (10a) equation (41) becomes

$$F = r - B = (C_\ell - B)\ X \qquad (44)$$

Thus, differenting equation (44)

$$F_x = [(C_\ell)_x - B_x]X + (C_\ell - B)X_x \qquad \text{(a)}$$

$$F_y = [(C_\ell)_y - B_y]X + (C_\ell - B)X_y \qquad \text{(b)} \qquad (45)$$

and for X = 0

$$F_x = (C_\ell - B)X_x \qquad \text{(a)}$$

$$F_y = (C_\ell - B)X_y \qquad \text{(b)} \qquad (46)$$

Using equation (43) and (46) in equation (40), the following result is obtained

$$P_z = \frac{\frac{R}{\lambda_+} - \frac{\gamma w^2}{A_1}\left[\frac{\bar{R}}{(C_\ell - B)} + \lambda_+ (X_x \tau_X + X_y \sigma_X)\right] - \lambda_+ P_X}{\left[\lambda_+ - \frac{\gamma T}{A_1}(\tau X_x + \sigma X_y)\right]} \tag{47}$$

This equation is integrated with the same scheme used for interior points with the X-derivatives computed using three-point end differencing away from the body.

To compute the velocity components on the body an intrinsic frame $(\hat{I},\hat{J},\hat{K})$ is used with velocity components $(\tilde{u},\tilde{v},\tilde{w})$. The vector $\hat{I}$ is the unit normal to the body with $\hat{J}$ and $\hat{K}$ defined as follows:

$$\hat{I} = I_1 \hat{i} + I_2 \hat{j} + I_3 \hat{k} \tag{a}$$

$$\hat{J} = (\hat{I} \times \hat{k})/\left|\hat{I} \times \hat{k}\right| = J_1 \hat{i} + J_2 \hat{j} + J_3 \hat{k} \tag{b} \qquad (48)$$

$$\hat{K} = \hat{I} \times \hat{K} = K_1 \hat{i} + K_2 \hat{j} + K_3 k \tag{c}$$

where $\hat{i}$, $\hat{j}$ and $\hat{k}$ are defined in figure 4. The x and y momentum equations are used to compute $\tilde{v}$ as follows. Equations (34b) and 34c) are integrated using the MacCormack scheme to obtain u and v and then $\tilde{v}$ is obtained from the equation

$$\tilde{v} = uJ_1 + vJ_2 \tag{49}$$

From the integrated form of the energy equation the $\tilde{w}$ component of velocity can be obtained

$$\tilde{w} = \sqrt{2H_o - \frac{2\gamma T}{\gamma - 1} - \tilde{v}^2} \tag{50}$$

where T is computed from P and S and the equation of state (19). The three Cartesian velocity components are

$$u = \tilde{v} J_1 + \tilde{w} K_1 \tag{a}$$

$$v = \tilde{v} J_2 + \tilde{w} K_2 \tag{b} \qquad (51)$$

$$w = \tilde{v} J_3 + \tilde{w} K_3 \tag{c}$$

Thus, all the dependent variables (P,u,v,w, and S) on the body are defined.

Modifications of this calculation for real gas and entropy layer effects will be discussed in later sections of this report.

BLUNT NOSE ENTROPY LAYER CALCULATION

On blunt nose bodies, as the computation proceeds downstream, the entropy gradient normal to the body becomes very large. Stream lines that cross a weaker bow shock and therefore have low entropies approach the body which is wetted by the stagnation stream line and therefore has a very large entropy. The pressure gradients at the body remain small as the edge of this layer approaches the body but the normal derivatives of S,u,v and w become very large. This physical phenomenon can create numerical problems for a calculation which does not handle it properly. A technique proposed by Moretti and Pandolfi (refs. 7 and 8) is used to account for this phenomenon.

In this section, after defining the "edge" of the entropy layer, the detection of points on the edge of the entropy layer, the calculation of the dependent variables at these points and the modification of the body calculation when the edge becomes close to the body will be discussed.

In figure 22 the entropy distribution (S vs X) in the windward symmetry planes on two typical geometries at several values of Z (axial stations) is shown. The *'ed points in figure 22 denote what is called the edge of the entropy layer. The entropy distributions are similar in other circumferential planes up to the top symmetry plane. The locus of these * points defines an "entropy layer surface" as $r = R_{HL}(Y,Z)$ (Fig. 23). This surface originates at the bow shock and moves toward the body as one proceeds downstream.

This surface is not a coordinate surface, so that in the computational plane the * point will be between two mesh points (Fig. 12) at each value of Y (it should be noted that this surface does not originate at the same axial station for all circumferential planes).

The key idea of this procedure is that no derivatives should be taken across this surface. The method used to insure that the derivatives S_X u_X, v_X and w_X are not taken across this surface when computing the mesh point near it is discussed in the section on interior point computations. The questions

remaining are: how the surface is detected and traced and how the dependent variables are computed on it.

The surface is detected at it's origin, the bow shock. When the entropy distribution is similar to the one shown in figure 22a (the entropy has a minimum) the * points at each value of Y is located at the mesh points adjacent to the bow shock when the entropy there is a minimum. The surface at this Y is initiated with the value of the dependent variables at this mesh point and is tracked separately from this station on. When the entropy distribution is similar to the one shown in figure 22b (no minimum exists) the * point at a value of Y is started when the S_X derivative at the mesh point adjacent to the shock has a minimum (i.e., $S_{XZ} \leq 0$).

The surface $r = R_{HL}(Y,Z)$ is a stream surface (i.e., a surface containing the same group of streamlines for all axial stations). This means that the velocity normal to the surface is zero. When at a station Z, all the dependent variables on the surface and the position of all the * points are known. Therefore, $(R_{HL})_Y$ of the surface can be computed using finite differences. The normal to the surface is

$$\bar{I}_{HL} = (r - R_{HL})_x \hat{i} + (r - R_{HL})_y \hat{j} + (r - R_{HL})_z \hat{k} \tag{52}$$

Since the velocity normal to the surface vanishes

$$(r - R_{HL})_x u + (r - R_{HL})_y v + (r - R_{HL})_z w = 0 \tag{53}$$

From this equation the following result can be obtained

$$\begin{aligned} R_{HL_Z} = {} & [u(r_X X_x + (r_Y - R_{HL_Y})Y_x) + \\ & v(r_{Xy} + (r_Y - R_{HL_Y})\,Y_y)]/w + r_X X_z + (r_Y - R_{HL_Y})Y_z + r_Z \end{aligned} \tag{54}$$

The position of the entropy layer surface at $Z_o + \Delta Z$ is given by

$$R_{HL}(Y,Z_o + \Delta Z) = R_{HL}(Y,Z_o) + R_{HL_Z}\,\Delta Z \tag{55}$$

Since the pressure is continuous across the surface the pressure at each * point can be obtained by interpolation using the two adjacent mesh points. The entropy and crossflow velocity at each * point are computed using the following relations

$$S_Z = -[S_Y'(uY_x + vY_y + wY_z)]/w \qquad (a)$$

$$u_Z = -[T(P_Y Y_x + P_X X_x) + u_Y'(uY_x + vY_y + wY_z)]/w \qquad (b) \qquad (56)$$

$$v_Z = -[T(P_Y Y_y + P_X X_y) + v_Y'(uY_x + vY_y + wY_z)]/w \qquad (c)$$

where S_Y', u_Y' and v_Y' are the Y-derivatives on the entropy layer surface.

These three equations are derived by taking a coordinate system (X',Y',Z') defined by the following transformation

$$X' = (r - B)/(R_{HL} - B) \qquad (a)$$

$$Y' = Y \qquad (b) \qquad (57)$$

$$Z' = Z \qquad (c)$$

The substantial derivative of any quantity f = (u,v,S) in this coordinate system is

$$\begin{aligned} \frac{Df}{Dt} &= uf_x + vf_y + wf_z \\ &= f_X'(uX_x' + vX_y' + wX_z') \\ &\quad + f_Y'(uY'_x + vY'_y + wY'_z) \\ &\quad + f_Z'(uZ'_x + vZ'_y + wZ'_z) \end{aligned} \qquad (58)$$

The coefficient of f_X' is zero on the "entropy layer" surface since the velocity normal to that surface is zero, while f_Y' is the Y-derivative on the surface and

$$\frac{Df}{Dt} = f_Y'(uY_x + vY_y + wY_z) + f_Z w \qquad (59)$$

To compute the velocity components an intrinsic coordinate system is used with unit vectors $(\hat{I},\hat{J},\hat{K})$ defined as follows:

$$\hat{I} = (X_x \hat{i} + X_y \hat{j} + X_z \hat{k}) / \sqrt{X_x^2 + X_y^2 + X_z^2} \qquad (a)$$

$$\hat{J} = (\hat{I} \times \hat{k}) / \left|\hat{I} \times k\right| \qquad (b) \qquad (60)$$

$$\hat{K} = \hat{I} \times \hat{J} \qquad (c)$$

The velocity components in the $\hat{I},\hat{J},\hat{K}$ directions are called $\tilde{u},\tilde{v},\tilde{w}$. The streamline slope in the (X,Z) plane is continuous across the entropy layer surface (just as in the case of a contact surface, where the slope of the contact surface is the same as that of the streamline adjacent to it ref. 7 and 8). Therefore $(\tilde{u}/\tilde{w})$ can be interpolated from the adjacent mesh points. Moreover, $\tilde{v} = uJ_1 + vJ_2$ where u and v are computed from equations 34b and 34c. Next, $\tilde{w}$ and $\tilde{u}$ are computed from the following equations

$$\tilde{w} = \sqrt{\frac{2Ho - 2\gamma T/(\gamma-1) - \tilde{v}^2}{(1+(\tilde{u}/\tilde{w})^2)}} \qquad (61)$$

$$\tilde{u} = (\tilde{u}/\tilde{w})\tilde{w} \qquad (62)$$

Then, from $\tilde{u},\tilde{v},\tilde{w}$ and the vectors $\hat{I},\hat{J},\hat{K}$, the velocity components u,v, and w are computed.

When the entropy layer surface becomes very close to the body (that is within 1% of the total shock layer thickness, figure 23c and 23d) at some value of the circumferential coordinate the entropy and the crossflow velocity $(\tilde{v})$ on the body are changed to their values on the edge of the entropy layer. The pressure at the body remains unchanged. On the body there is a jump in entropy at the points where the entropy layer surface separates from the body (Fig. 23c), so that Y-derivatives cannot be taken across these points.

For grid points that have collapsed Y-derivatives are always taken onto the entropy layer surface. For the Y-derivative at a grid point that hasn't been collapsed but is adjacent to a point that has been, a pseudo grid point is located at the adjacent collapsed point with the blunt nose entropy, and velocity direction and pressure of the collapsed point.

Changing the body entropy, from the high stagnation-point value to the low value at the edge of the entropy layer increases the axial Mach number and therefore increases the step size (ΔZ) at which the computation can proceed. In some cases the axial Mach number would become subsonic with the stagnation entropy and the computation would be unable to proceed. This significant advantage could not have been gained without following the entropy layer explicitly.

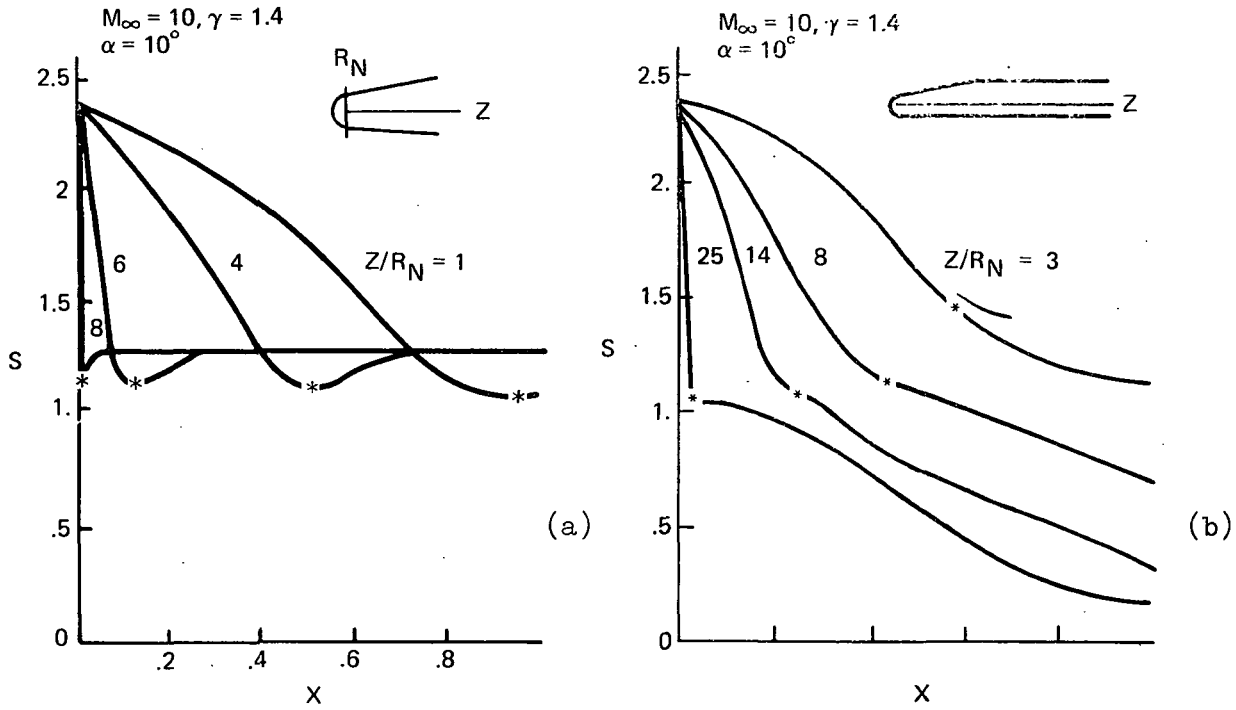

Figure 22. - Typical entropy distribution

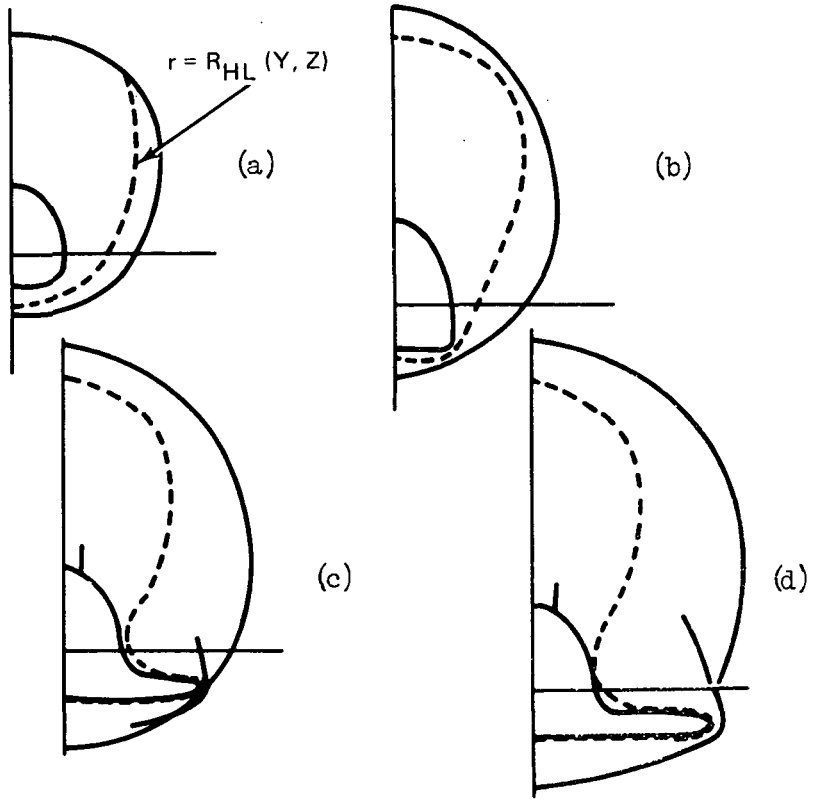

Figure 23. - Entropy surface (physical plane)

REAL GAS EFFECTS (EQUILIBRIUM/FROZEN AIR)

In some flight regimes encountered by hypersonic vehicles the simple assumption of air being a perfect gas is not acceptable and real gas effects must be taken into account. Grossly speaking, real gas effects shift but do not change the qualitative pattern calculated with perfect gas thermodynamics. A code for real gas should, therefore, be patterned along the same lines as a code for perfect gas.

It is in this spirit that the real air problem has been approached. The salient points of the procedure that has been adopted are:

1. The equations of motion are written using the same dependent variables as for the perfect gas calculations, namely, the three velocity components, the logarithm of pressure and entropy.
2. Simple analytical expressions, developed by Moretti (ref. 16), are used to fit the Mollier diagrams for equilibrium air. The ability to suddenly "freeze" the fluid with an equivalent ideal gas γ is included.
3. The computational time has not increased out of proportion. The computational time needed for a perfect gas computation is increased by a factor of less than 50% when equilibrium real gas effects are included.
4. An accuracy of around 5% is maintained for enthalpies less than $500 \times (\rho_{SL}/p_{SL})$
5. The parts of the code dealing with gas properties are kept separated from the flow calculations so that if necessary the code may be easily extended to helium, nitrogen, CF_4, or supersteam.

The equations of motion in nondimensional form are:

$$wP_z + uP_x + vP_y + \Gamma(w_z + u_x + v_y) = 0 \qquad (a)$$

$$ww_z + uw_x + vw_y + \tau P_z = 0 \qquad (b)$$

$$wu_z + uu_x + vu_y + \tau P_x = 0 \qquad (c) \qquad (63)$$

$$wv_z + uv_x + vv_y + \tau P_y = 0 \qquad (d)$$

$$wS_z + uS_x + vS_y = 0 \qquad (e)$$

where $\tau = p/\rho$ and $\Gamma = a^2/\tau$. The only difference from perfect gas is in Γ and τ. The quantity, τ is not the temperature except for a perfect gas; it is $\tau = zT$, where T is the temperature and z is the compression coefficient. Similarly, Γ is not $\gamma(c_{p_\infty}/c_{v_\infty})$ except for a perfect gas. For equilibrium flow both τ and Γ are obtained at every point via the Mollier fits.

The Mollier fits for τ and Γ developed by Moretti (ref. 16) are written in terms of enthalpy and pressure.

$$\bar{\tau} = \bar{\tau}_o = a + b\bar{h} + c/(\bar{h} + d) \qquad (0 < \bar{h} \leq 50,\ 150 \leq \bar{h} \leq 350) \qquad (a)$$

$$\bar{\tau} = \bar{\tau}_o + fe^{g(\bar{h}+m)^2} \qquad (50 \leq \bar{h} \leq 150) \qquad (b) \qquad (64)$$

$$\bar{\tau} = \bar{\tau}_o + ke^{(\bar{h}/50-10)} \qquad (350 \leq \bar{h} \leq 500) \qquad (c)$$

and

$$\Gamma = \Gamma_o = (\epsilon + \xi\,\bar{h} + \eta e^{\sigma\bar{h}})/H_o \qquad \begin{pmatrix} 0 \leq \bar{h} \leq 50, \\ 150 \leq \bar{h} \leq 500 \end{pmatrix} \qquad (a)$$

$$\Gamma = \Gamma_o \bar{\tau}_o/(\bar{\tau} + fe^{g(\bar{h}+m)^2}) \qquad (50 < \bar{h} < 150) \qquad (b) \qquad (65)$$

where

$$\bar{h} = \rho_{SL}\, h/p_{SL},\quad \bar{P} = P - \ell n(p_{SL})$$

and

$$t = \frac{12030.872}{77.938126-\bar{P}} - .764759(\bar{P} + 157.7555)$$

$$\ell = 12.813 + .0871477\ (\bar{P} + 9.4423)^2$$

$$d = 250\ (\ell - t)/(2t - \ell - 79.4)$$

$$a = (.3176 - b)\ d$$

$$b = 3176 + (1 + d/250)(r - 79.4)/250$$

$$c = -ad$$

$$f = -1.83 + 1.098/(e^{-.8686(\bar{P} - 1.72725)} + 1.)$$

$$g = -.0038 - .00219476/(\bar{P} + 10.3635)$$

$$m = -84.6 - .34744\ \bar{P}\ (1.- .21745\bar{P})$$

$$k = 9.2217 - .05213171(\bar{P} + 8.0605)^2$$

$$\epsilon = 1.0459 + .00424528\bar{P}$$

$$\xi = (12.707 - .424528\ \bar{P})\ 10^{-5}$$

$$\eta = 1.1828-\epsilon$$

$$\sigma = -(.001955 + \xi)/\eta$$

The subscript SL refers to sea level conditions as follows (the bar in the following equations means dimensional quantities):

$$p_{SL} = \bar{p}_{SL}/\bar{p}_\infty$$
$$\rho_{SL} = \bar{\rho}_{SL}/\bar{\rho}_\infty \qquad (66)$$

The normalized entropy, S, as a function of enthalpy and pressure is given by

$$S = (\gamma - 1)\ \bar{S}/\mathcal{R} \qquad (67)$$

where

$$\gamma = c_{p_\infty}/c_{v_\infty}$$

$$\frac{\bar{S}^*}{R} = 4.82068 \ln(\bar{h}) + 11.875 + .0245\,\bar{h} + 1175./(\bar{h} + 50) + .434294\,B\,\bar{P}$$

and

$$B = -2307. - (.0042\,\bar{h} - .092)/[1. + e^{(.07(45. - \bar{h}))}]$$

Since τ and Γ must be obtained as functions of entropy and pressure, the expression given for the entropy is solved for the enthalpy, and then with the enthalpy and pressure, τ and Γ are obtained from the remaining fits.

The interior point computation can be performed by the same procedure used for perfect gases, except that τ and Γ are computed via the curve fits.

Some changes are necessary in the shock computation. If subscripts 1 and 2 refer to the low pressure side and high pressure side of the shock respectively, and if V_n and $\vec{V}_T$ refer to the velocity components in the directions of the normal and tangent to the shock respectively then the jump conditions are given by

$$\frac{V_{n1}}{V_{n2}} = \frac{1. + 1./(\Gamma_2 M_{n2}^2)}{1. + 1./(\Gamma_1 M_{n1}^2)} \qquad \text{(a)}$$

$$\vec{V}_{T2} = \vec{V}_{T1} \qquad \text{(b)}$$

$$\rho_1/\rho_2 = V_{n2}/V_{n1} \qquad \text{(c)} \qquad (68)$$

$$p_1/p_2 = \frac{1 + \Gamma_2 M_{n2}^2}{1 + \Gamma_1 M_{n1}^2} \qquad \text{(d)}$$

$$h_1 + \frac{V_{n1}^2 + |\vec{V}_{T1}|^2}{2} = h_2 + \frac{V_{n2}^2 + |\vec{V}_{T2}|^2}{2} \qquad \text{(e)}$$

*Note: $\bar{S}$ is the dimensional entropy referenced to 0° Kelvin and 1 atmosphere of pressure.

The method of solution follows the same procedure used for a perfect gas. The shock slope and V_{n_2} are guessed and equation (68a) is used to solve for $\Gamma_2 M_{n2}^2$. Equation (68d) is then solved for p_2 and from equation (68e) h_2 is obtained. The ratio ρ_2/ρ_1 is then computed from equation (68c).

A second value for ρ_2/ρ_1 is obtained from the curve fits of the Mollier chart using h_2 (obtained from Eq. (68e) and p_2. An iteration is now performed on V_{n_2} until the difference in the two computed values of ρ_2/ρ_1 is sufficiently small. The rest of the calculation is identical to that used for a perfect gas.

The equilibrium air calculation starts at the nose of the vehicle and continues until a "freezing plane" (i.e., a plane Z = constant), after which both the chemistry and vibrational relaxation are assumed fixed (this is called frozen air in what follows). This freezing station (Z_{fr}) is user input. At the freezing station Z_{fr} all the dependent variables are related by the Mollier fits and are in equilibrium. (P_{EQ}, S_{EQ}, u_{EQ}, v_{EQ}, w_{EQ}, T_{EQ} and h_{EQ}. The frozen equations of state are (ref. 17)

$$p_{fr}/\rho_{fr} = (\mathcal{R}/\mathcal{R}_\infty)\, T_{fr} \qquad (a)$$

$$h_{fr} = \left(\frac{\mathcal{R}}{\mathcal{R}_\infty}\right)\left(\frac{\Gamma}{\Gamma-1}\right) T_{fr} \qquad (b) \qquad (69)$$

$$S_{fr} = \left(\frac{\mathcal{R}}{\mathcal{R}_\infty}\right)\left(\frac{\gamma-1}{\Gamma-1}\right) \left\{ \Gamma \ell n\, T_{fr} - (\Gamma-1)\, P_{fr} + S_{REF} \right\} \qquad (c)$$

with the quantities $(\mathcal{R}/\mathcal{R}_\infty)$, Γ and S_{REF} defining the properties of the gas downstream of freezing station. In order to match the equilibrium state (i.e., $P_{fr} = P_{EQ}$, $S_{fr} = S_{EQ}$ $u_{fr} = u_{EQ}$ etc.) at each mesh point one must set:

$$\mathcal{R}/\mathcal{R}_\infty = (p_{EQ}/\rho_{EQ})/T_{EQ} \qquad (a)$$

$$\Gamma = \frac{h_{EQ}(\mathcal{R}/\mathcal{R}_\infty)}{h_{EQ}\,\mathcal{R}/\mathcal{R}_\infty - T_{EQ})} \qquad (b) \qquad (70)$$

$$S_{REF} = \frac{S_{EQ}}{(\mathcal{R}/\mathcal{R}_\infty)}\,\frac{\Gamma-1}{\gamma-1} - \Gamma \ell n\ T_{EQ} + (\Gamma-1)\ P_{EQ} \qquad (c)$$

Downstream of this station, these quantities are constant along streamlines because they are functions only of the concentration of species which are in turn constant along streamlines. But since the variation $(\mathcal{R}/\mathcal{R}_\infty)$, Γ and S_{REF} is small at the freezing plane, they are averaged.

Downstream of the freezing station, equations (70) are used instead of the Mollier-curve fits to relate thermodynamic properties.

SPECIALIZED OUTPUT

Calculations have been added to the procedure which use the inviscid flow field solution to compute desired results in a useable engineering form or as an input to other calculations. At the user's option, the flow field data may be used to calculate aerodynamic coefficients, boundary layer input quantities, (streamlines, metric coefficients, etc.) and sonic boom data. Following is a description of the approach used for each of these calculations.

Aerodynamic Coefficients. Aerodynamic coefficients are calculated, when desired, along with the flow field. Vectored pressures, located at the area centroid of triangular facets (two such facets between each pair of mesh points in the previous and current data planes) and directed normal to the facet plane, are summed at each step over user-specified portions of the vehicle. By making use of the body lines (running cross sectional control points) in the QUICK geometry package, the coefficients C_L, C_D, C_M, C_N, and C_A can then be computed from the appropriate direction components of the integrated forces and moments for virtually any body components (even multiply disjoint sections such as the body-alone represented by the solid line in Fig. 24).

The pitching moments are referenced to a user-specified position in the vehicle symmetry plane. Coefficients are expressed in two fashions - (1) referenced to the surface area integrated thus far for the given component (this surface area is included in the output), and (2) referenced to a user input area. In both cases the reference pressure and density are $\bar{p}_\infty$ and $\bar{\rho}_\infty$.

Aerodynamic coefficients and wetted areas are available in terms of the entire vehicle, its components, and their distributions in z.

Boundary Layer Input Quantities. The boundary layer input quantities are calculated in two steps. During the flow field computation, integration techniques are applied to obtain the metric coefficient h_1, defined herein.

Consider Figure 25, in which the fixed body coordinates (x, y, z), the unit vectors ($\hat{i}$, $\hat{j}$, $\hat{k}$), and velocity directions (u, v, w) have been indicated. Also shown is an inviscid streamline on the surface of the body, and the associated coordinates (ξ, η, ζ), unit vectors ($\hat{\xi}$, $\hat{\eta}$, $\hat{\zeta}$), and the velocity directions ($\tilde{u}$, $\tilde{v}$, $\tilde{w}$). The $\hat{\eta}$- direction is taken along the streamline, the

$\hat{\zeta}$-direction is perpendicular to the body and $\hat{n}$ and the $\hat{\xi}$ - direction is perpendicular to both $\hat{\eta}$ and $\hat{\zeta}$.

Associated with these two sets of coordinates, (x, y, z) and (ξ, η, ζ), we have the three scalar factors (h_1, h_2, h_3), defined by:

$$h_1^2 = x_\xi^2 + y_\xi^2 + z_\xi^2$$

$$h_2^2 = x_\eta^2 + y_\eta^2 + z_\eta^2$$

$$h_3^2 = x_\zeta^2 + y_\zeta^2 + z_\zeta^2$$

Now,

$$\vec{\eta} = h_2\hat{\eta} = h_2(u/q\hat{i} + v/q\hat{j} + w/q\hat{k})$$

or,

$$x_\eta = h_2\ u/q$$

$$y_\eta = h_2\ v/q$$

$$z_\eta = h_2\ w/q$$

The body surface normal ($\hat{\zeta} = \zeta_1\hat{i} + \zeta_2\hat{j} + \zeta_3\hat{k}$) is readily available, and

$$x_\zeta = h_3\ \zeta_1$$

$$y_\zeta = h_3\ \zeta_2$$

$$z_\zeta = h_3\ \zeta_3$$

and since $\hat{\xi} = \hat{\eta}$ x $\hat{\zeta}$,

$$x_\xi = h_1(z_\eta\ y_\zeta - y_\eta\ z_\zeta)/h_2\ h_3 = h_1\ (w\zeta_2 - v\zeta_3)/q$$

$$y_\xi = h_1(x_\eta\ z_\zeta - z_\eta\ x_\zeta)/h_2\ h_3 = h_1\ (u\zeta_3 - w\zeta_1)/q$$

$$z_\xi = h_1(y_\eta\ x_\zeta - x_\eta\ y_\zeta)/h_2\ h_3 = h_1\ (v\zeta_1 - u\zeta_2)/q$$

In three-dimensions, between any two points P and P', we have:

$$d\vec{P} = d\vec{\xi} + d\vec{\eta} + d\vec{\zeta}$$
$$= h_1\, d\xi\hat{\xi} + h_2\, d\eta\hat{\eta} + h_3\, d\zeta\hat{\zeta}$$

We get:

$$\frac{\partial \vec{P}}{\partial \xi} = h_1\, \hat{\xi}$$

$$\frac{\partial \vec{P}}{\partial \eta} = h_2\, \hat{\eta}$$

$$\frac{\partial \vec{P}}{\partial \zeta} = h_3\, \hat{\zeta}$$

and,

$$\frac{\partial}{\partial \eta}\left(\frac{\partial \vec{P}}{\partial \xi}\right) = \frac{\partial}{\partial \xi}\left(\frac{\partial \vec{P}}{\partial \eta}\right)$$

$$\frac{\partial}{\partial \eta}\left(\frac{\partial \vec{P}}{\partial \zeta}\right) = \frac{\partial}{\partial \zeta}\left(\frac{\partial \vec{P}}{\partial \eta}\right)$$

$$\frac{\partial}{\partial \xi}\left(\frac{\partial \vec{P}}{\partial \zeta}\right) = \frac{\partial}{\partial \zeta}\left(\frac{\partial \vec{P}}{\partial \xi}\right)$$

thus,

$$\frac{\partial h_1}{\partial \eta}\,\hat{\xi} + \frac{\partial \hat{\xi}}{\partial \eta}\,h_1 = \frac{\partial h_2}{\partial \xi}\,\hat{\eta} + \frac{\partial \hat{\eta}}{\partial \xi}\,h_2$$

$$\frac{\partial h_3}{\partial \eta}\,\hat{\zeta} + \frac{\partial \hat{\zeta}}{\partial \eta}\,h_3 = \frac{\partial h_2}{\partial \zeta}\,\hat{\eta} + \frac{\partial \hat{\eta}}{\partial \zeta}\,h_2$$

$$\frac{\partial h_3}{\partial \xi}\,\hat{\zeta} + \frac{\partial \hat{\zeta}}{\partial \xi}\,h_3 = \frac{\partial h_1}{\partial \zeta}\,\hat{\xi} + \frac{\partial \hat{\xi}}{\partial \zeta}\,h_1$$

Finally, dot multiplying by the appropriate unit vector ($\hat{\xi}$, $\hat{\eta}$ or $\hat{\zeta}$) we obtain,

$$\frac{\partial h_1}{\partial \eta} = h_2 \frac{\partial \hat{\eta}}{\partial \xi} \cdot \hat{\xi} \qquad \text{(a)}$$

$$\frac{\partial h_2}{\partial \xi} = h_1 \frac{\partial \hat{\xi}}{\partial \eta} \cdot \hat{\eta} \qquad \text{(b)} \qquad (71)$$

$$\frac{\partial h_3}{\partial \eta} = h_2 \frac{\partial \hat{\eta}}{\partial \zeta} \cdot \hat{\zeta} \qquad \text{(c)}$$

We make the usual assumption of $h_3 = 1$, which is valid in the absence of a strong entropy layer. Observing equation (71a), one will note that h_2 is differentiated with respect to (ξ) which leads to a multiplier of the h_{2_Z} derivative that corresponds to a cross flow velocity which may vanish, thus making an axial marching technique inapplicable to the determination of h_2. The other parts of equation (71) involve (η) derivatives which lead to an axial velocity type multiplier which is always non-zero and relatively large for the cases to which this computational procedure is to be applied.

Equation (71a) is then recast, using the appropriate transformations as discussed in the section on the computational plane, to obtain a differential equation for h_1 which is integrated at mesh points on the body during the computation.

The metric coefficient h_1 is then stored in an array and treated the same as any other flow variable. An exterior calculation then uses this data as input to trace streamlines on the surface of the vehicle, create the pseudo-stream surfaces (by taking normals to the body at points along the streamlines of length 3 x flat plate boundary layer thickness), and interpolate in three dimensions to obtain all quantities and derivatives of interest in these surfaces. Normal derivatives are formed numerically.

The method used for tracing streamlines on the body does not rely on simply stepping in the velocity direction (thus in most cases off the body) and then arbitrarily "pulling" the new point to a "corresponding" position on the body.

Instead, a method was devised to work directly with the angular position (θ_s') of the streamline on the body. A differential equation was set up for $d\theta_s'/dz$ on the body, and was integrated in a marching fashion.

Consider the vector triad ($\hat{N},\hat{B},\hat{T}$) as shown in Figure 26. $\hat{N}$ is the normal to the body (supplied analytically by our geometry package), $\hat{B}$ is a body tangent lying entirely in the cross sectional plane, and $\hat{T}$ is also tangent to the body, and equals $\hat{B} \times \hat{N}$.

$$\hat{N} = N_x\hat{i} + N_y\hat{j} + N_z\hat{k}$$

$$\hat{B} = B_x\hat{i} + B_y\hat{j} + B_z\hat{k}$$

$$\hat{T} = T_x\hat{i} + T_y\hat{j} + T_z\hat{k}$$

Since $\hat{B}$ must lie in the x, y plane, $B_z \equiv 0$. Also,

$$\hat{N} \cdot \hat{B} = 0 = B_x N_x + B_y N_y$$

and since $\hat{B}$ is a unit vector,

$$1 = B_x^2 + B_y^2$$

Accordingly,

$$B_x = -N_y / \sqrt{N_x^2 + N_y^2}$$

$$B_y = N_x / \sqrt{N_x^2 + N_y^2}$$

Finally, since $\hat{T} = \hat{B} \times \hat{N}$,

$$T_x = B_y N_z$$

$$T_y = B_x N_z$$

$$T_z = B_x N_y - N_x B_y$$

Now define the velocity directions ($\tilde{u}$, $\tilde{v}$, $\tilde{w}$) in the ($\hat{N}$, $\hat{B}$, $\hat{T}$) directions. Since $\vec{V} = u\hat{i} + v\hat{j} + w\hat{k}$

$$\tilde{u} = \vec{V}\cdot\hat{N} = 0 = uN_x + vN_y + wN_z$$

$$\tilde{v} = \vec{V}\cdot\hat{B} = uB_x + vB_y$$

$$\tilde{w} = \vec{V}\cdot\hat{T} = uT_x + vT_y + wT_z$$

In the (r', θ', z') and (x', y', z') coordinate systems (Fig. 5, $z' = z$), we define an elemental length (ds) lying in the x', y' (or x, y) plane, such that,

$$\vec{\tilde{v}} = \frac{ds}{dt}\,\hat{B}$$

We also note that,

$$\vec{w} = \frac{dz'}{dt}\,\hat{k}' = \frac{dz}{dt}\,\hat{k}$$

Accordingly,

$$\frac{\tilde{v}}{w} = \frac{ds}{dt}\,\frac{dt}{dz} = \frac{ds}{dz}$$

$$ds = \tilde{v}/w\ dz$$

We can also write

$$ds^2 = dr'^2 + r'^2\ d\theta'^2$$

which yields

$$d\theta' = ds/\sqrt{(dr'/d\theta')^2 + r'^2}$$

and thus,

$$\frac{d\theta'}{dz} = \frac{(\tilde{v}/w)}{\sqrt{(dr'/d\theta)^2 + r'^2}}$$

Then, using a second order backwards integration, assuming ($d\theta_s'/dz$) linear between computational planes (see Figure 27),

$$\frac{d\theta'_s}{dz} = \left(\frac{d\theta'_s}{dz}\right)_o + \left[\left(\frac{d\theta'_s}{dz}\right)_1 - \left(\frac{d\theta'_s}{dz}\right)_o\right]\frac{z-z_o}{\Delta z_o}$$

$$\theta'_{s_2} = \theta'_{s_1} + \int_{z_1}^{z_2} \left(\frac{d\theta'_s}{dz} \right) dz$$

we obtain:

$$\theta'_{s_2} = \theta'_{s_1} + \frac{\Delta z}{\Delta z_o} \left[\left(\frac{d\theta'_s}{dz} \right)_1 \left(\Delta z_o + \frac{\Delta z}{2} \right) - \left(\frac{d\theta'_s}{dz} \right)_o \frac{\Delta z}{2} \right]$$

This method of integration is used to trace any set of streamlines from specified positions on the body in the initial data plane. The radial position of these streamlines is, of course, supplied immediately by the geometry package for a given θ'_s.

Sonic Boom Data. Sonic boom calculations make use of the same data as the boundary layer quantity calculation. Another calculation performs a two-dimensional second order interpolation in given data planes to obtain the values of flow field variables (p, S, u, v, w) on a data cylinder enclosing the body, of user-specified radius, whose center line is the z or body axis (FRL).

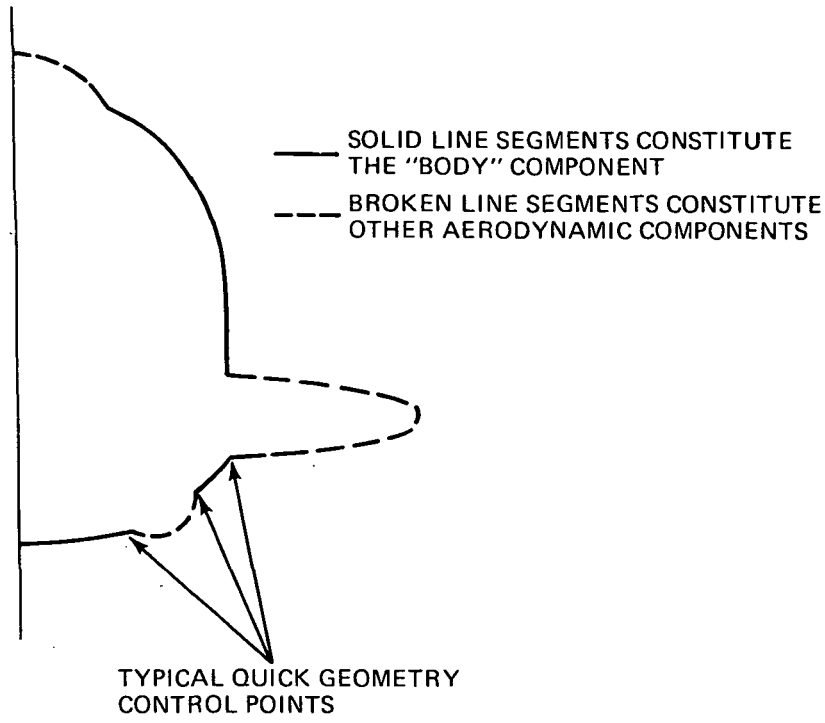

Figure 24. - Example of modular breakup for aerodynamic coefficients.

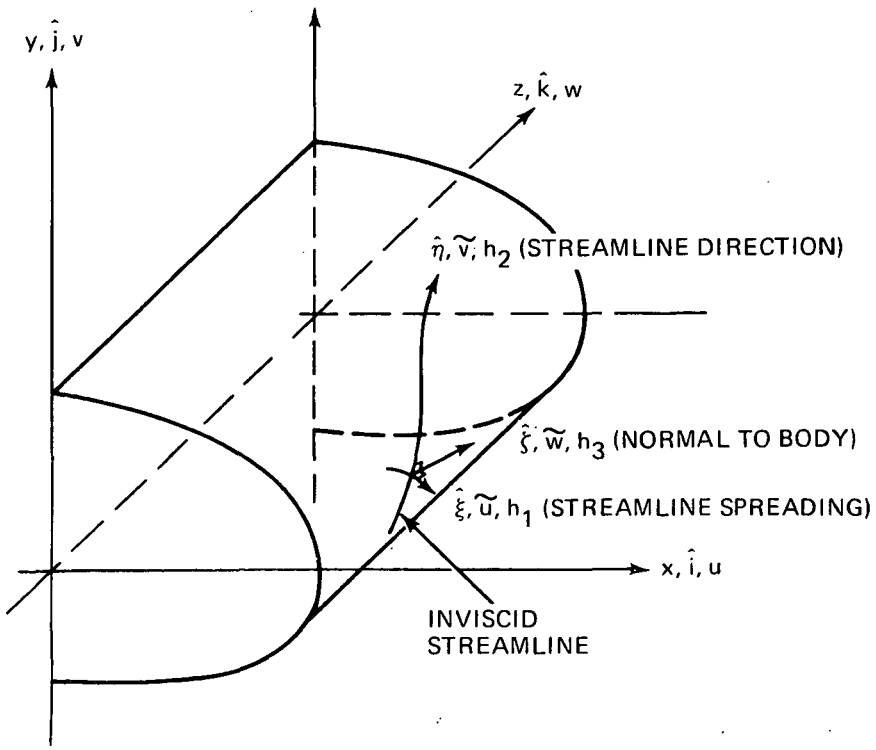

Figure 25. - Definition of coordinate system for metric coefficient calculation.

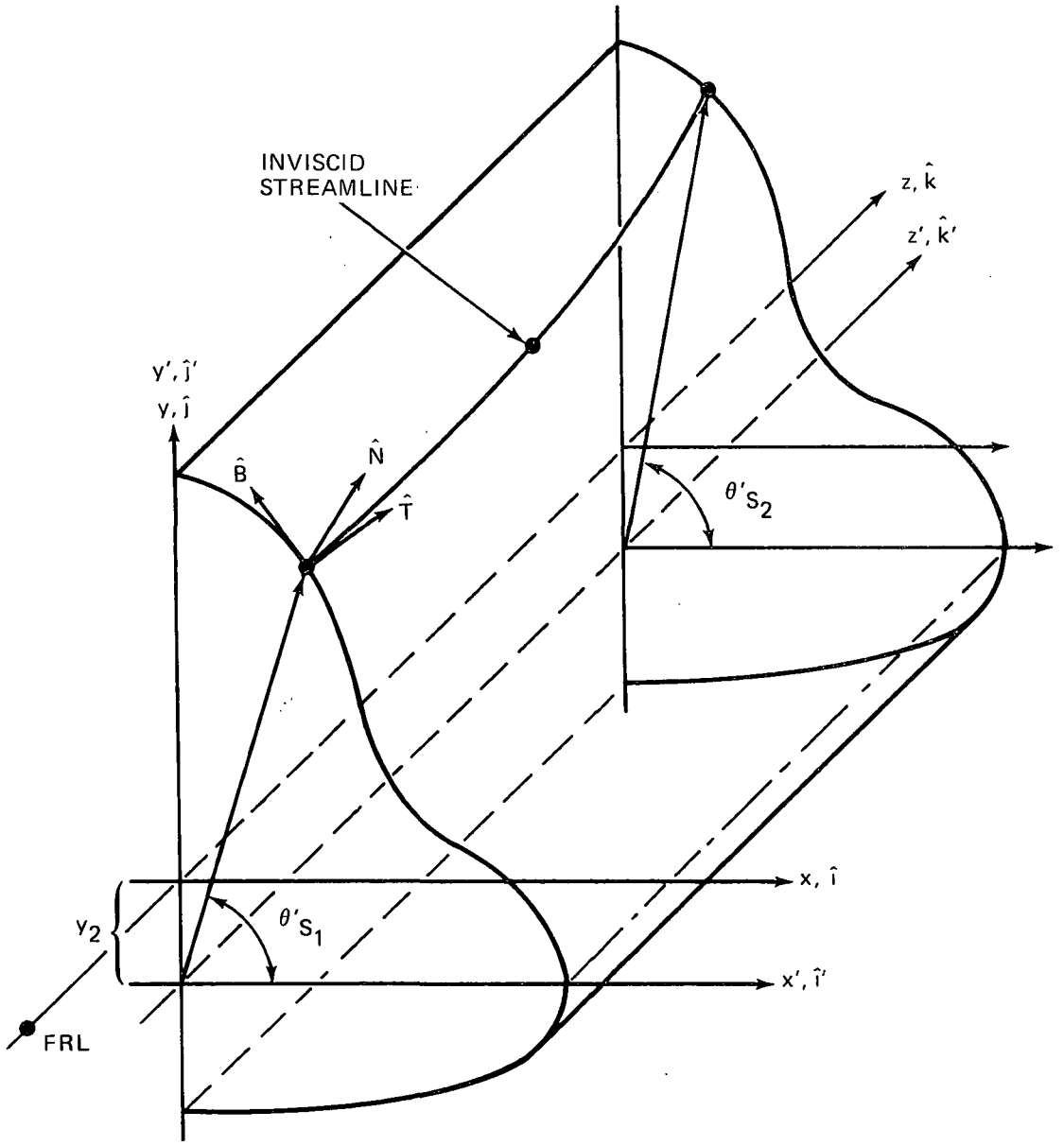

Figure 26. - Definition of coordinate system for streamline tracing technique

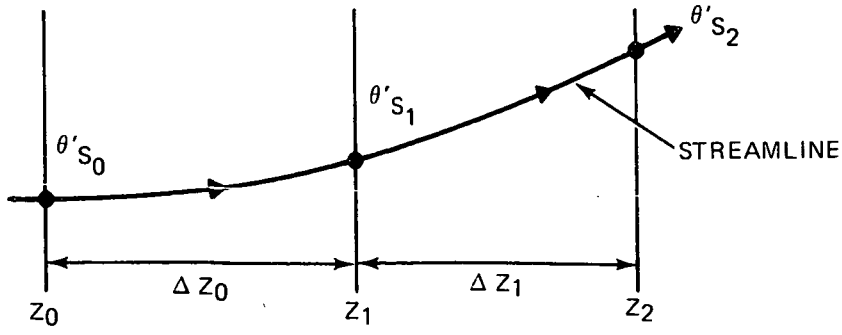

Figure 27. - Diagram for streamline marching procedure.

TYPICAL RESULTS

During the course of this work the flow fields about a large number of geometries have been studied. Firstly to be sure that the numerical techniques used worked for all these configurations, second to compare the results with existing data, and finally to study flow field phenomenon which can't be studied through other means. In this section some of the results of these calculations will be discussed. Most of these results have been presented previously in references 18 and 19.

In figure 28 the surface streamlines and pressure distribution are shown for an 80° slab delta wing at 30° angle of attack with $M_{\infty} = 9.6$. At this high angle of attack the cross flow velocity expands around the wing tip and becomes supersonic on the lee side. This velocity component must vanish at the leeward symmetry plane and therefore a cross flow shock (Fig. 19a) is generated. The strength of this shock at the body is demonstrated by the streamline deflection across it. Figure 26 shows an axial and circumferential surface pressure distribution compared with experimental data (ref. 18). The jump in pressure (circumferential distribution) at about $\theta = 170^{\circ}$ is due to the cross flow shock. The calculation of this flow from a starting plane ($Z/R_N \cong .8$) to the end ($Z/R_N = 15$) took about 15 minutes on the IBM 370/168 computer.

Figures 29, 30, 31 and 32 all describe the flow about an early version of a shuttle orbiter configuration flying at an angle of 30° for $M_{\infty} = 26.1$. The calculation was performed for an ideal gas, $\gamma = 1.12$. Figure 29 shows the top and side views of the shocks and body, while figure 30 shows the cross sectional views. The shock pattern in this calculation is quite complex, a strake shock is generated at $Z \cong 380$ and intersects the bow shock at $Z \cong 440$, a cross flow shock is generated starting at $Z \cong 550$ and a wing shock starts at $Z \cong 800$ and intersects the bow shock at $Z \cong 850$. Figure 31 shows the surface pressure variation with surface distance around the vehicle at several cross sectional stations. Between $Z = 800$ and $Z = 850$ there is a large pressure raise (Fig. 31) due to the beginning of the wing. The large

peak in pressure at Z = 850 could not be computed without concentrating grid points in the wing tip region. Near Z = 850 the wing shock intersects the bow shock and causes an expansion fan which reduces the pressure (at the wing tip) further downstream. This phenomenon can be observed up to Z = 1050; while the peak pressure remains unchanged, the expansion moves toward the windward symmetry plane. The drop in the peak pressure between Z = 1050 and Z = 1100 is due to the wing tip turning parallel to the flow. Figure 32 shows the radial entropy distribution at three circumferential positions (X is the normalized radial coordinate). In these figures the thinning of the entropy layer is shown. This calculation (from Z = 50 to Z = 1280) took approximately 1.5 hours on the IBM 370/168 using a maximum of 20 x 30 grid points.

Figure 33 shows the surface pressure distribution in the windward symmetry plane on the forward portion of the 089-B shuttle orbiter. The calculations were performed using equilibrium air thermodynamics (at 215 thousand feet altitude) and ideal gases at γ = 1.12 and 1.4. In each case the Mach number was 26.1 and the angle of attack was 30°. The trends in the γ = 1.12 and real gas cases look very similar, while in the γ = 1.4 calculation the recompression (after the nose expansion) seems weaker. In the real gas calculation the computer running time was increased by approximately 30 percent. Figure 34 shows the surface streamlines on the 089-B shuttle orbiter. In the figure, the strength of the cross flow shock is demonstrated by its deflection of the surface streamlines.

The windward symmetry plane surface pressure distributions on a modified version of the current 140-C space shuttle orbiter are shown in figure 35 for M_{∞} = 10.29, γ = 1.4, and α = 20 and 25°. The vehicle was modified for the computations by increasing the wing sweep from 45° to 55° (fig. 35) to avoid subsonic axial Mach numbers near the wing tip which would occur for this value of γ. This modification has little effect on the windward symmetry plane pressure distributions. The calculated results are compared with experimental data (unpublished) obtained at NASA/Ames. The agreement is very good except near the trailing edge. The under prediction near the trailing edge is due to a mismatch in lower surface slope (of approximately 5°) between the experimental and numerical geometry models.

The circumferential pressure distribution for this configuration at Z/L = 0.3 is compared with experimental data in figure 36. Again the agreement is very good. These calculations required approximately one hour of computing time on the CDC 6600 using a maximum of 15 x 32 grid points.

Another complex shock pattern is shown in figure 37. The vehicle is a fighter aircraft and the flight conditions are $M_\infty = 2.5$ and $\alpha = 6^\circ$. In this flow field there was a canopy shock, a wing shock and an additional shock due to a recompression after the canopy. Figure 37c shows a series of cross sectional views in which the intersection of the canopy and bow shocks is evident. This calculation demonstrated that flow fields containing multiple imbedded shocks in a cross section can be computed treating all shocks explicitly.

Figure 38 compares the computed and experimental surface pressures on this vehicle ($M_\infty = 2.2$, $\alpha = 5$ and 10°). The experiment was run by Grumman Aerospace Corp. at NASA/Ames and the data are unpublished. This calculation (from Z = 0 to Z = 45) took about 1 hour on the IBM 370/165 computer with a 24 x 29 grid in each cross section.

Figure 39 shows the inlet flow field for a supersonic fighter configuration. The axial station shown corresponds to the inlet forward lip station, so that this is the flow field ingested by the inlet. The maximum difference between calculation and experiment is less than 3 percent. The experimental data were obtained from reference 31 and the calculation took approximately 30 minutes on the IBM 370/165 with a 25 x 30 grid.

Figure 40 shows surface pressure distributions on the X-15 aircraft top and bottom symmetry planes. In figure 40a the flight Mach number is 6 and in figure 40b the Mach number is 4. The comparison with the experimental data is good. The deviation from the experimental results near the vehicle nose is due to the starting solution which was used (i.e., a conical flow solution was used to start the calculation).

Figure 41 shows a sample of the type of sharp leading edge wing configuration which can be computed. The figure shows the computed shock pattern with the bow shock intersecting the wing shock.

Shown in figure 42 is another complex shock pattern. The vehicle is a hypersonic research aircraft (HSRA) configuration and the flight conditions are $M_\infty = 6$, $\gamma = 1.2$, and $\alpha = 0^\circ$. As shown in the figure the canopy shock is generated ahead of Z = 36 and is intersecting the bow shock at Z = 60. A shock wave is generated by the vertical tail ahead of Z = 50. Figure 43 shows a lift vs angle of attack curve for the HSRA vehicle. Both the experimental and Newtonian flow results were supplied by Mr. Lewis Clark of NASA/LRC. The figure shows that both the Newtonian calculation (with viscous effects included) and the present one compute lift accurately. The calculation of the HSRA flow field ($M_\infty = 6$ $\alpha = 0^\circ$) took 1 hour on the IBM 370/168 computer using a 25 x 30 grid.

The metric coefficients of the coordinate system based on the body streamlines (see figure 44) are one of the less straightforward by-products of this computation.

On normals to the body, flow quantities and their normal derivatives are also automatically computed (Fig. 45) and turn out to be smooth and satisfactory.

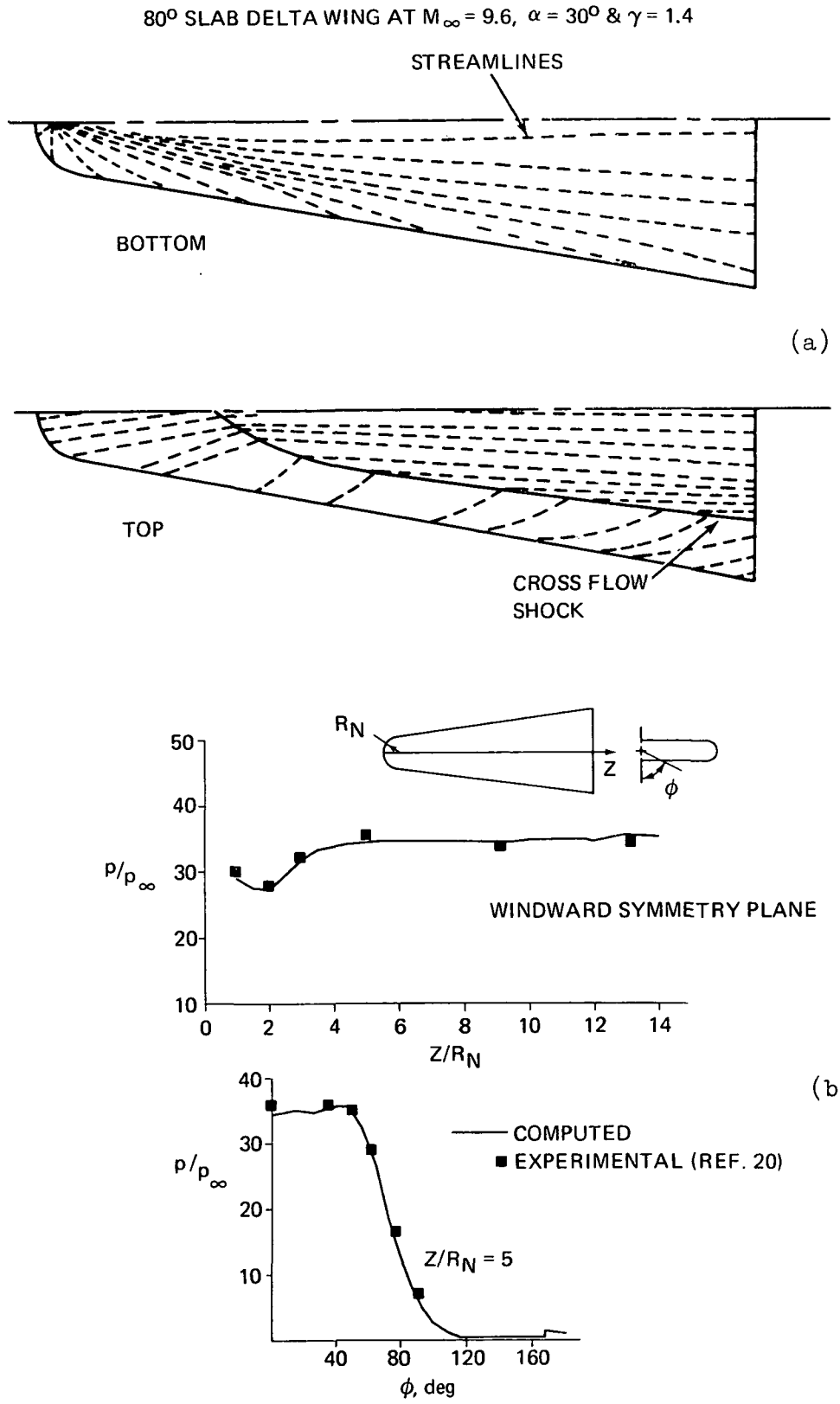

Figure 28. - Slab delta wing streamlines and surface pressure.

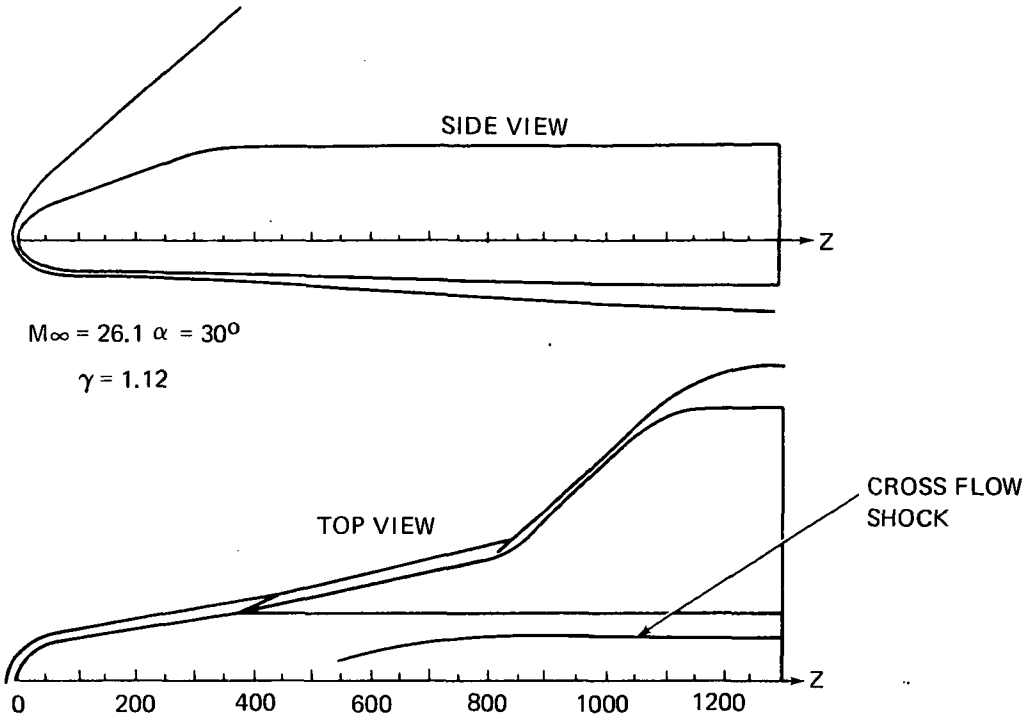

Figure 29. - 089-B shuttle orbiter shock patterns.

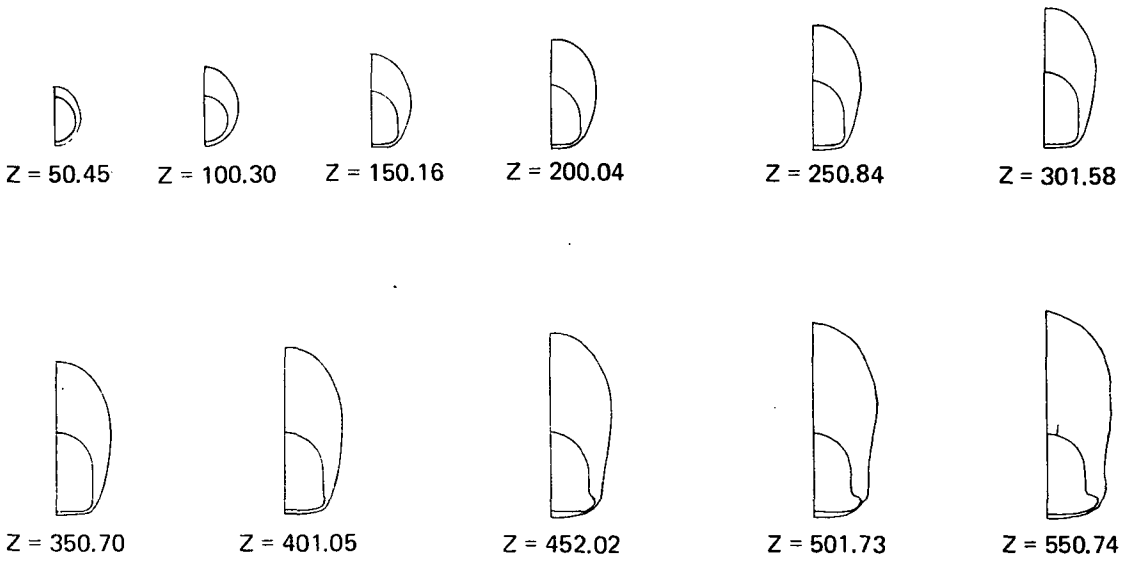

Figure 30. - 089-B orbiter cross sectional shock patterns.

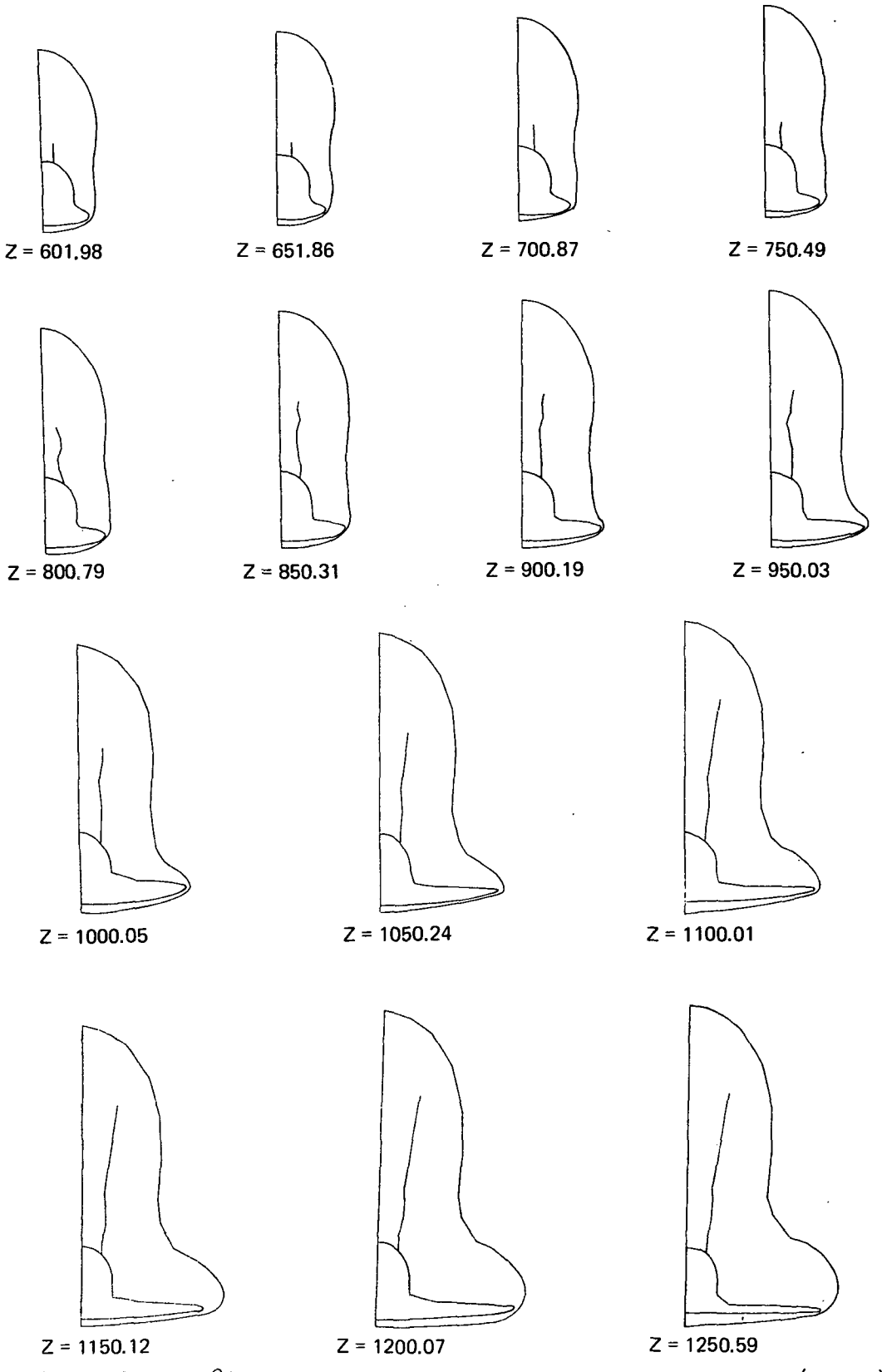

Figure 30. - 089-B orbiter cross-sectional shock patterns (contd).

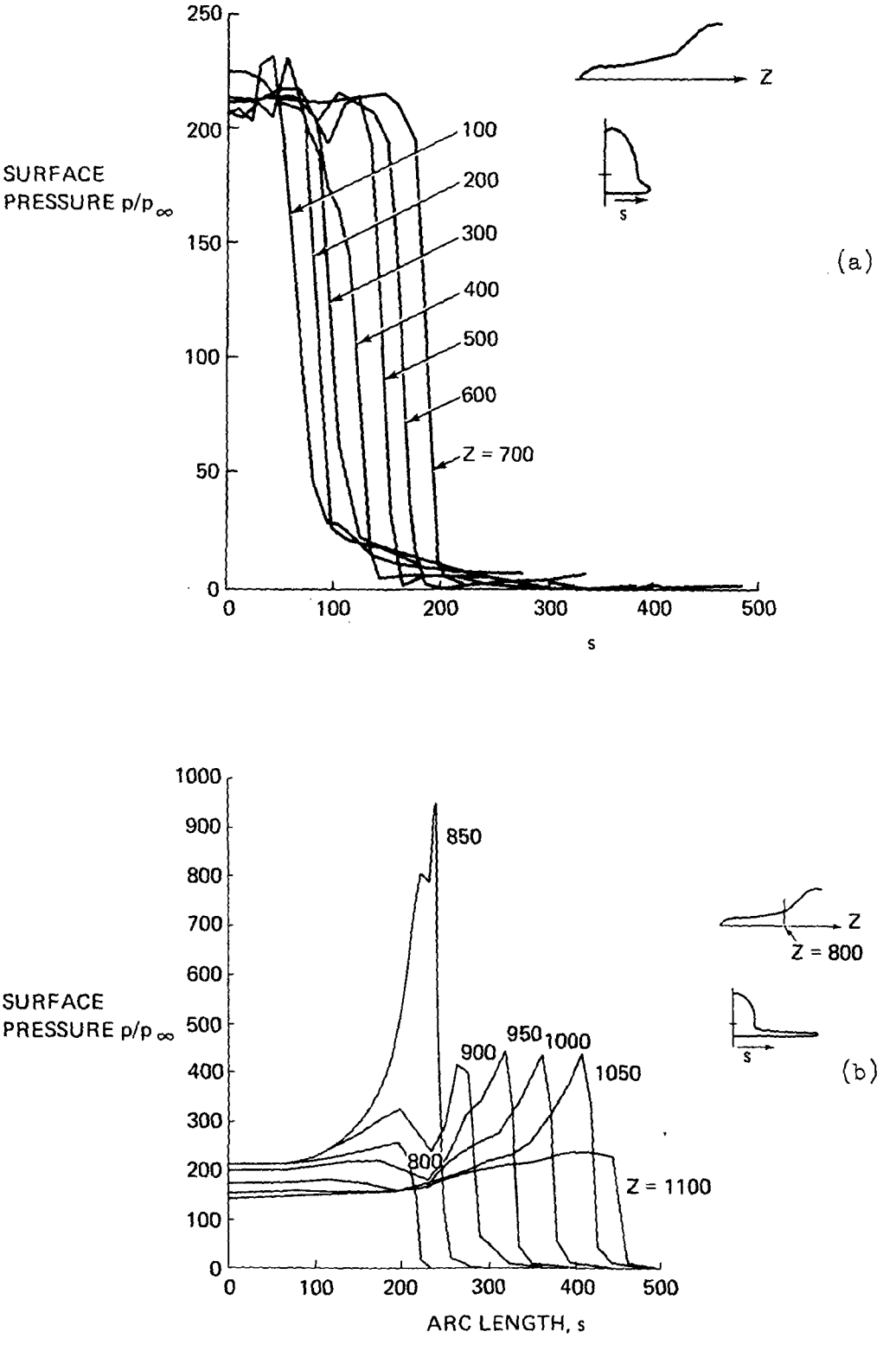

Figure 31. - 089-B orbiter surface pressure.

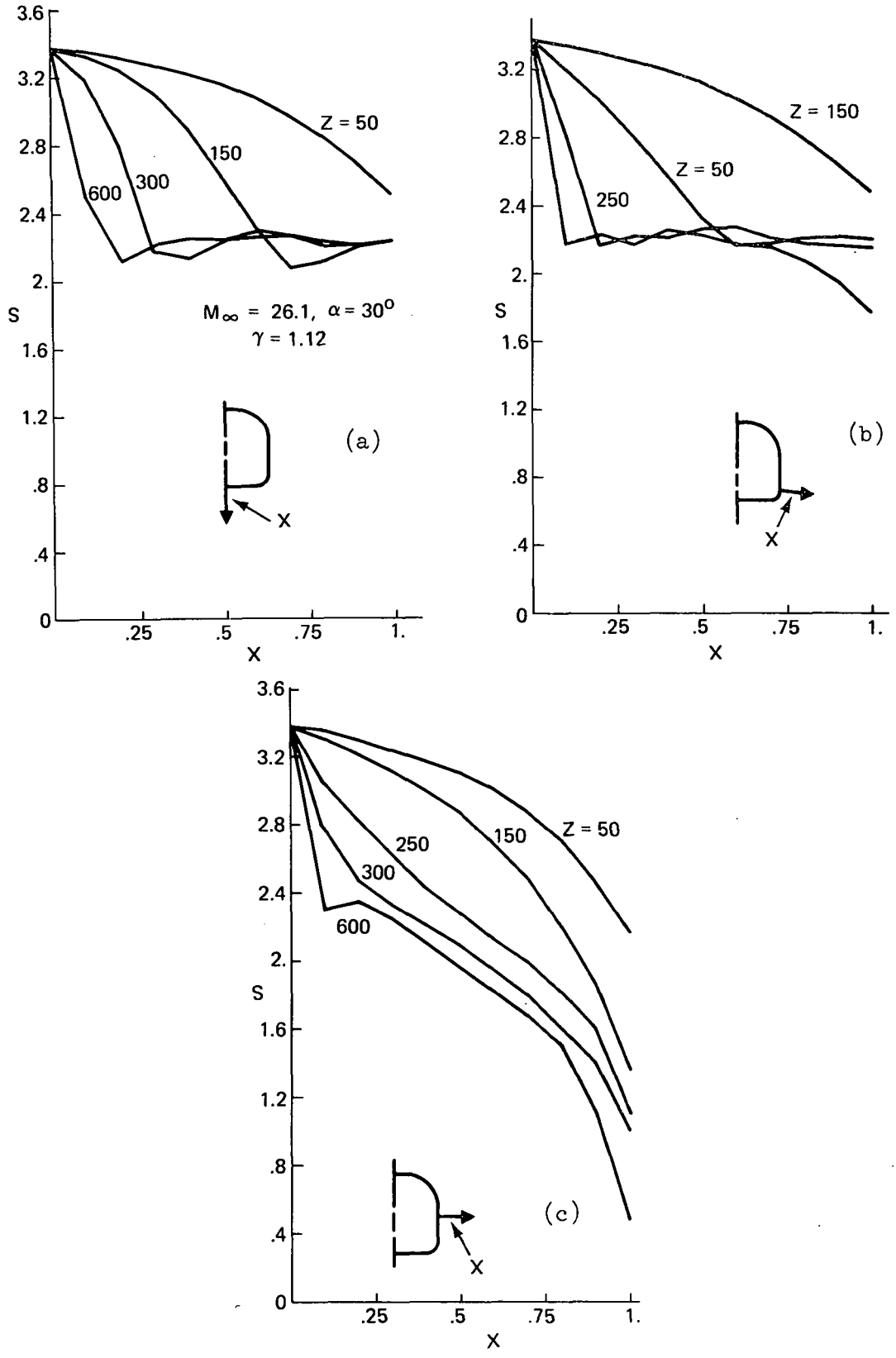

Figure 32. - 089-B orbiter entropy distribution.

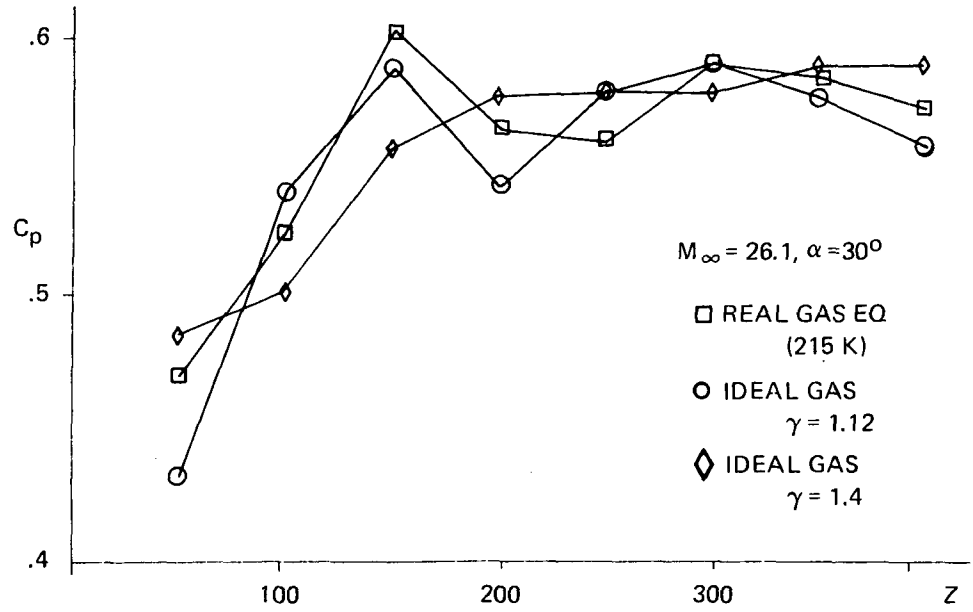

Figure 33. - 089-B orbiter windward plane surface pressure.

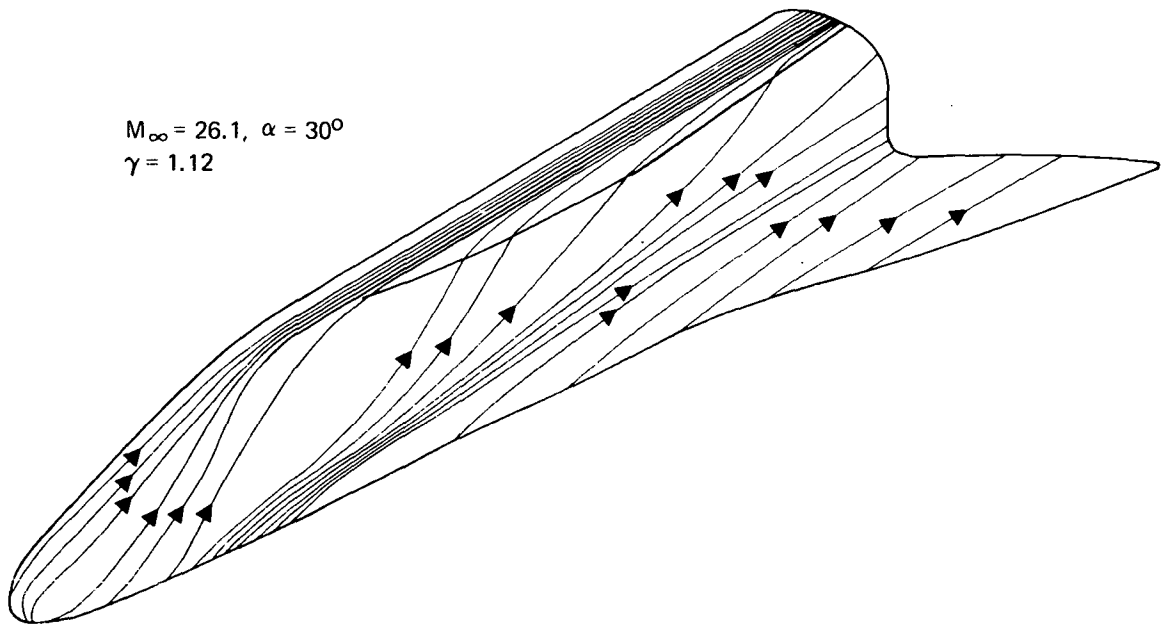

Figure 34. - 089-B orbiter surface streamlines.

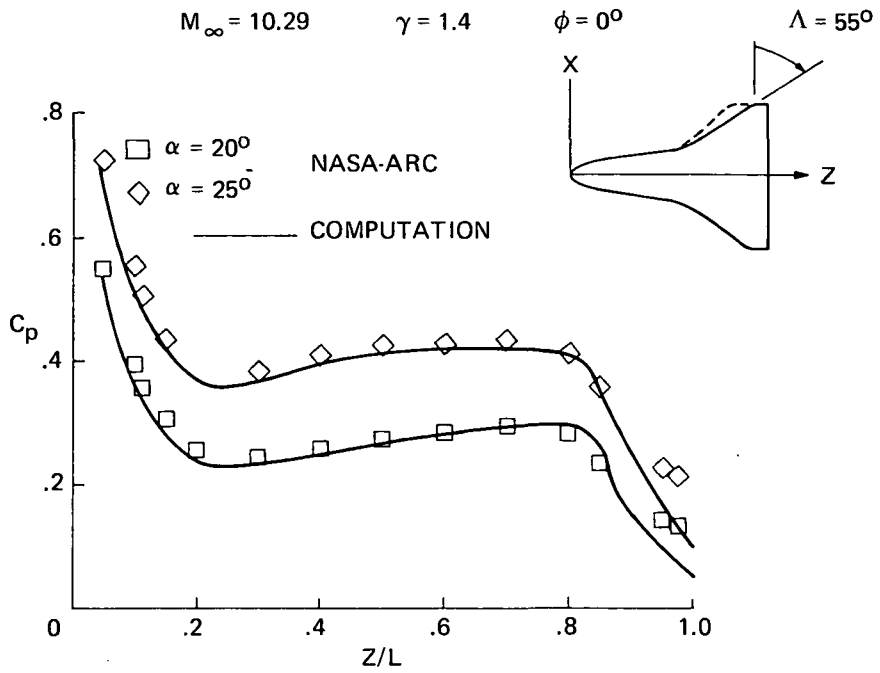

Figure 35. - Windward symmetry plane distribution, modified 140-c shuttle orbiter.

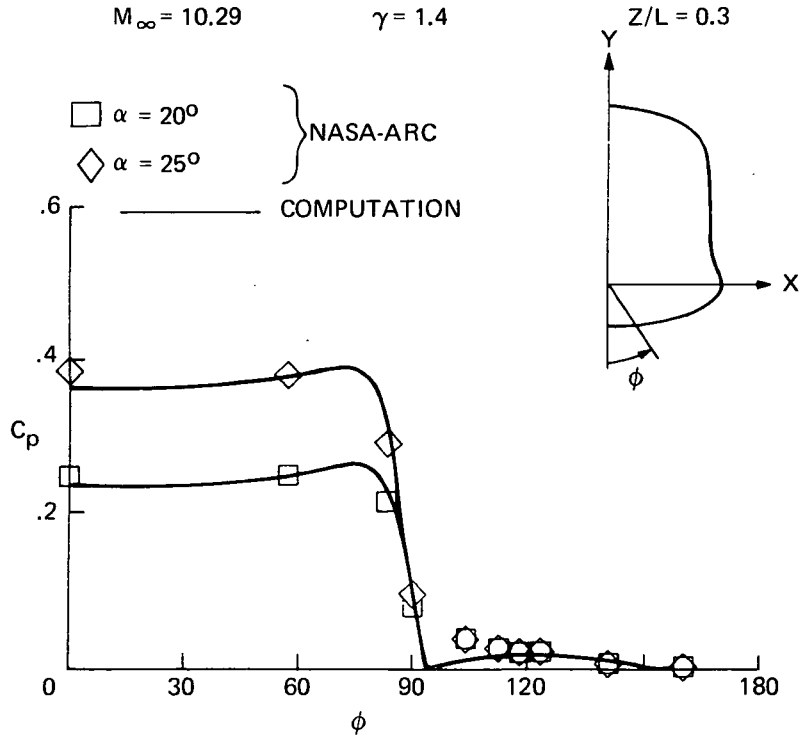

Figure 36. - Circumferential pressure distribution, modified 140-c shuttle orbiter.

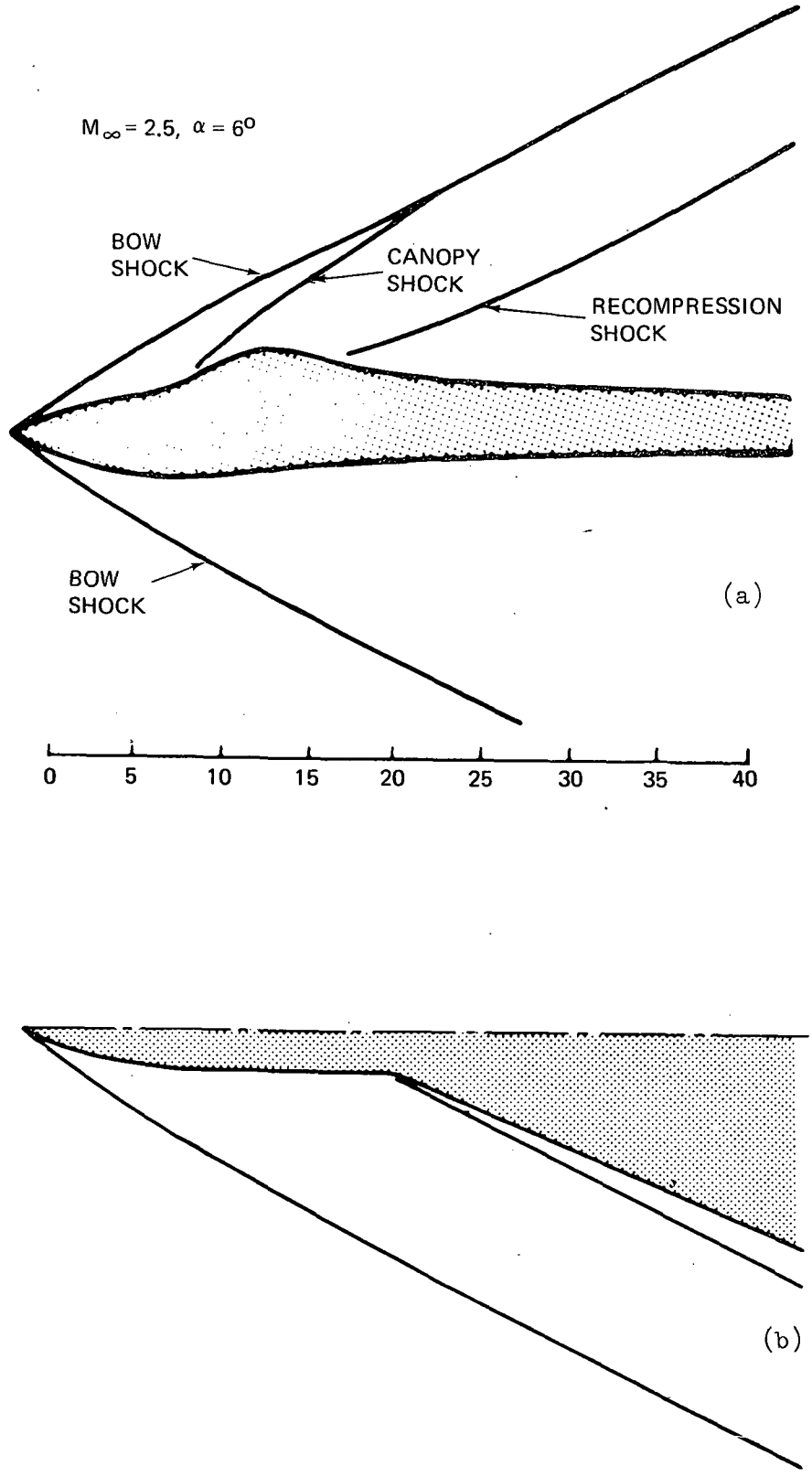

Figure 37. - Aircraft configuration shock pattern.

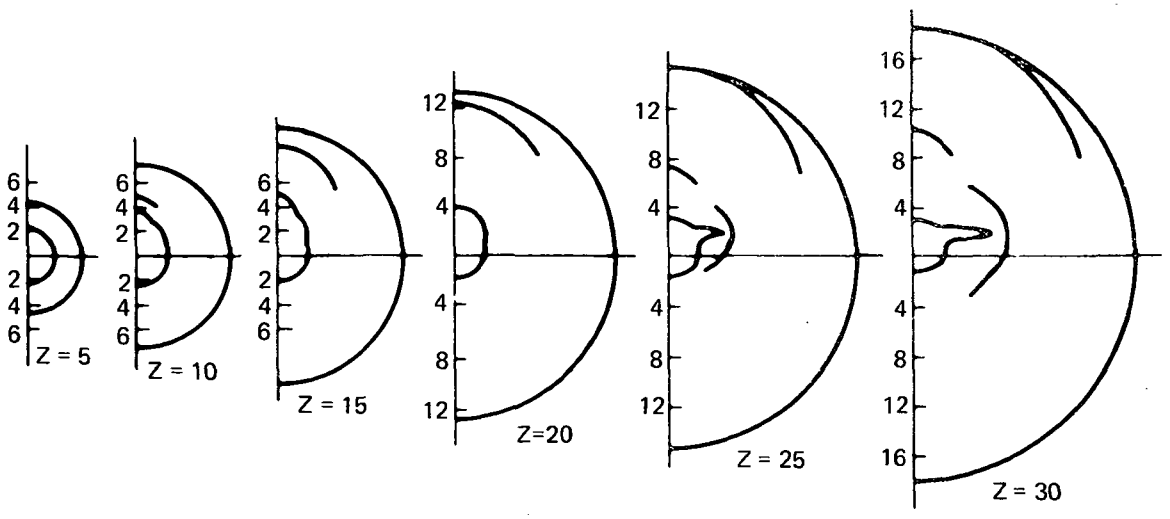

(c)

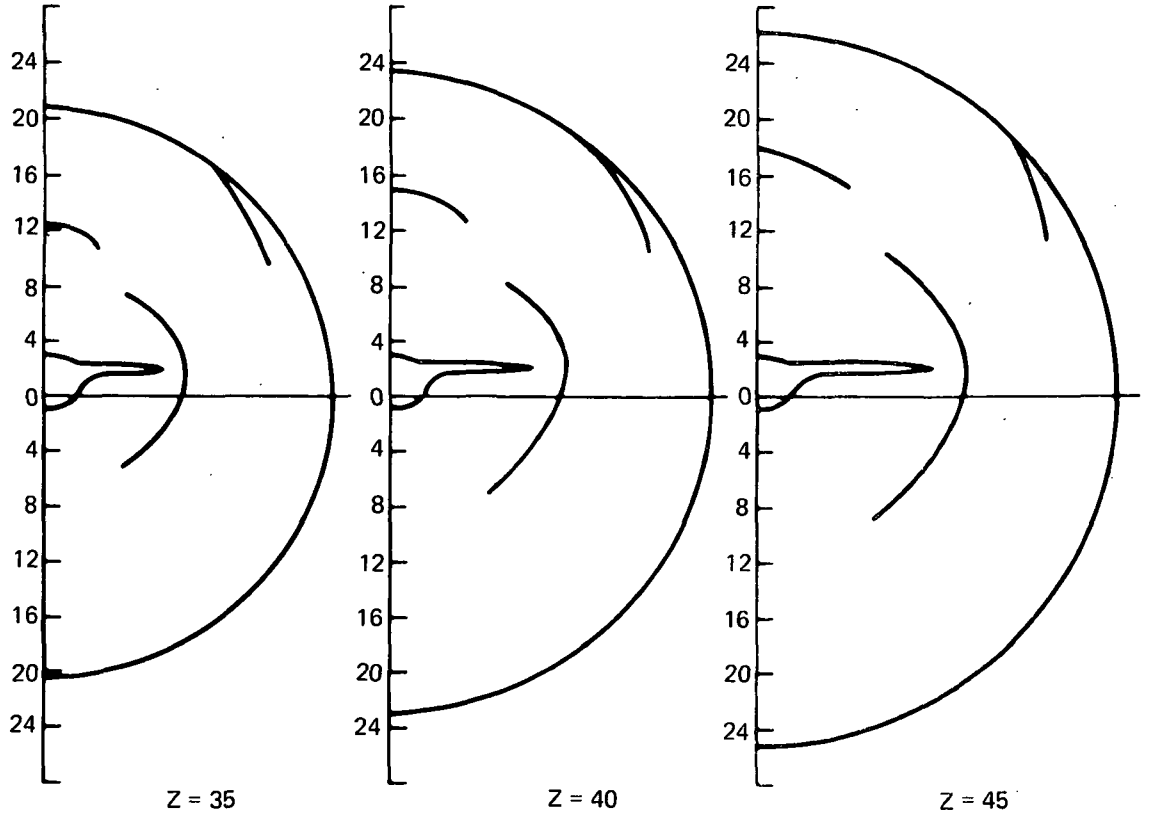

Figure 37. - Aircraft configuration shock pattern (contd).

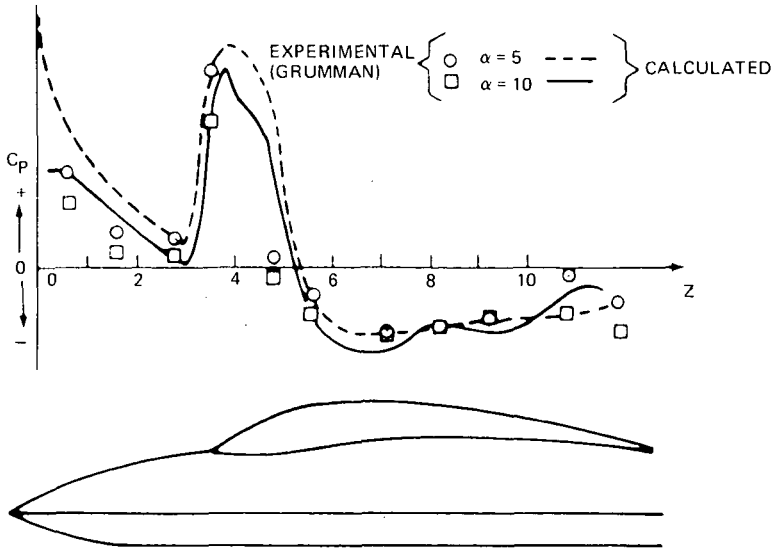

Figure 38. - Aircraft configuration, top symmetry plane surface pressure ($M_\infty = 2.2$).

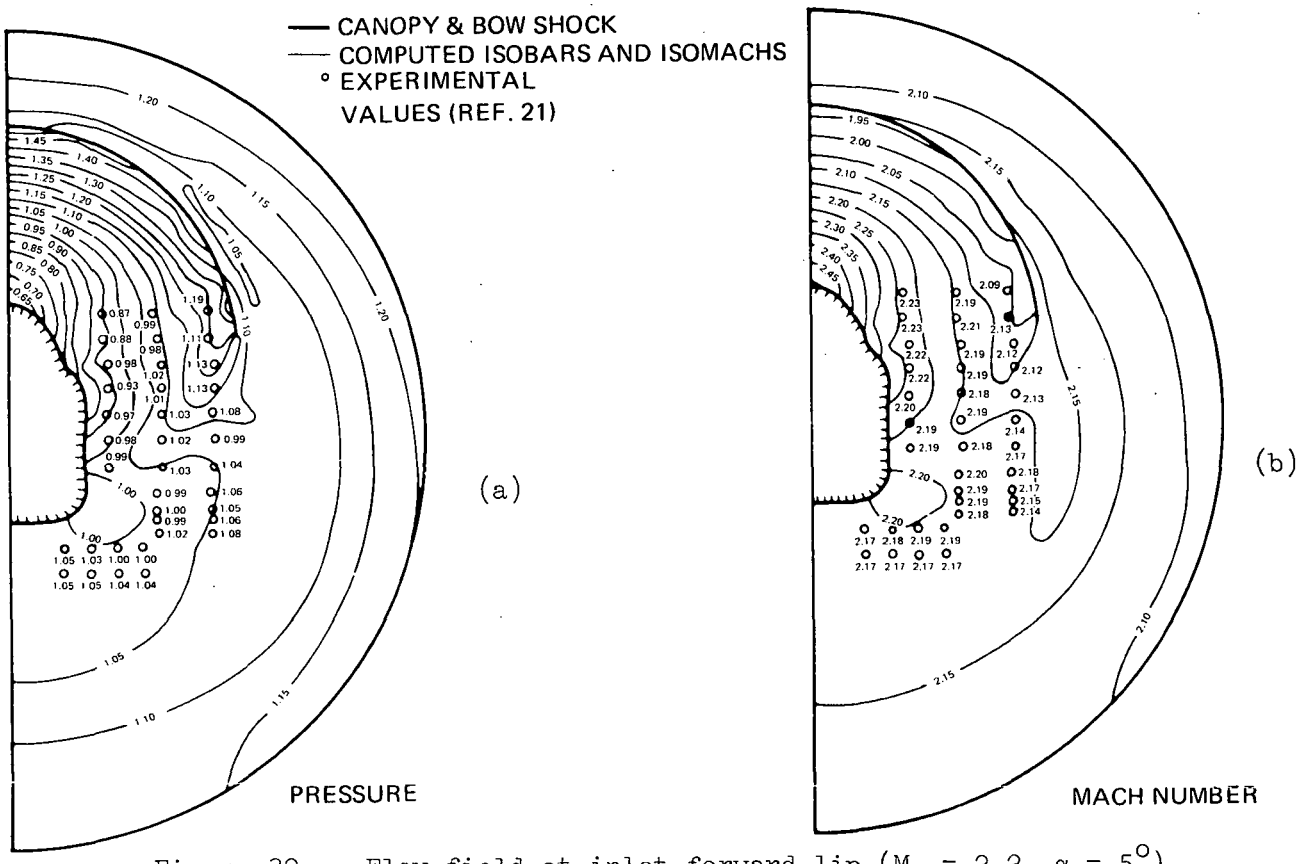

Figure 39. - Flow field at inlet forward lip ($M_\infty = 2.2$, $\alpha = 5^\circ$).

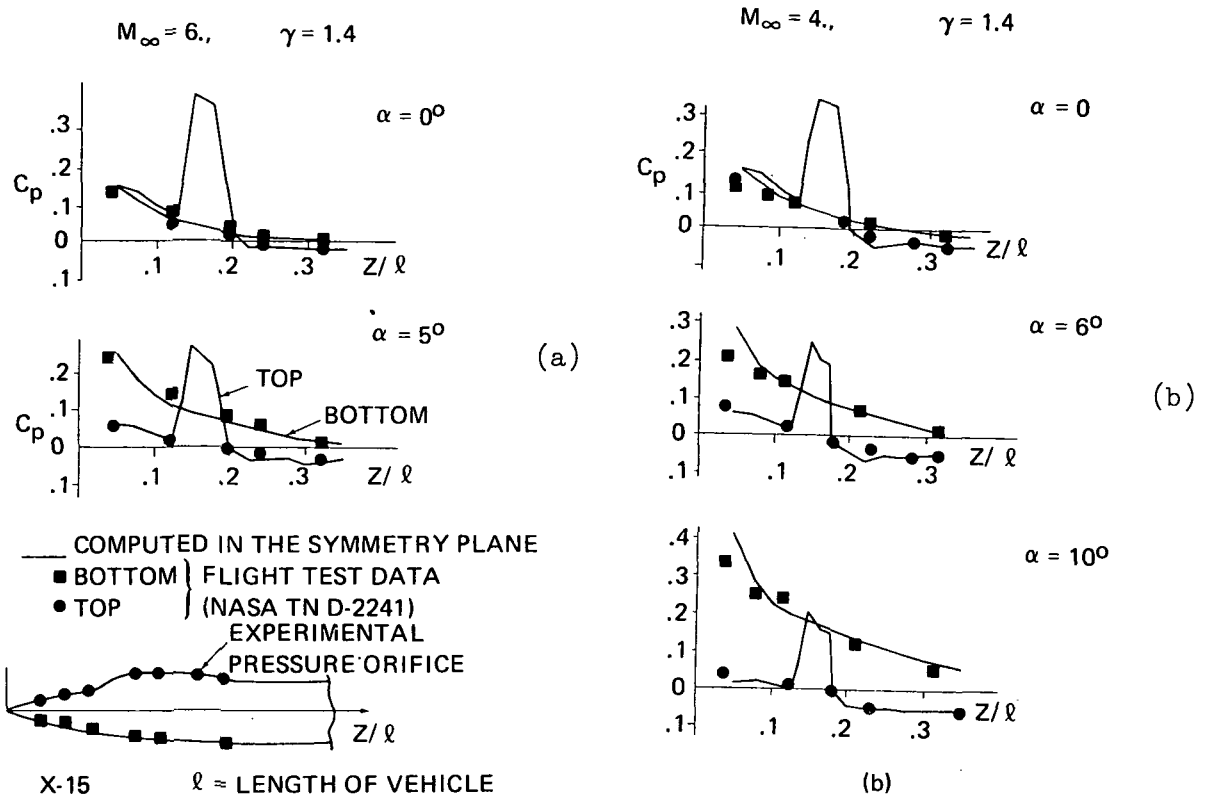

Figure 40. - X-15 surface pressure.

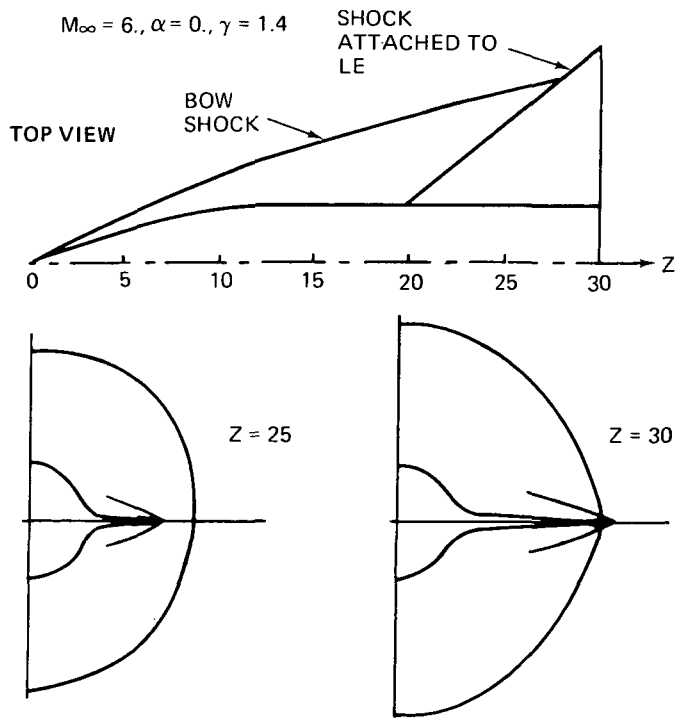

Figure 41. - Sharp leading edge wing configuration shock pattern.

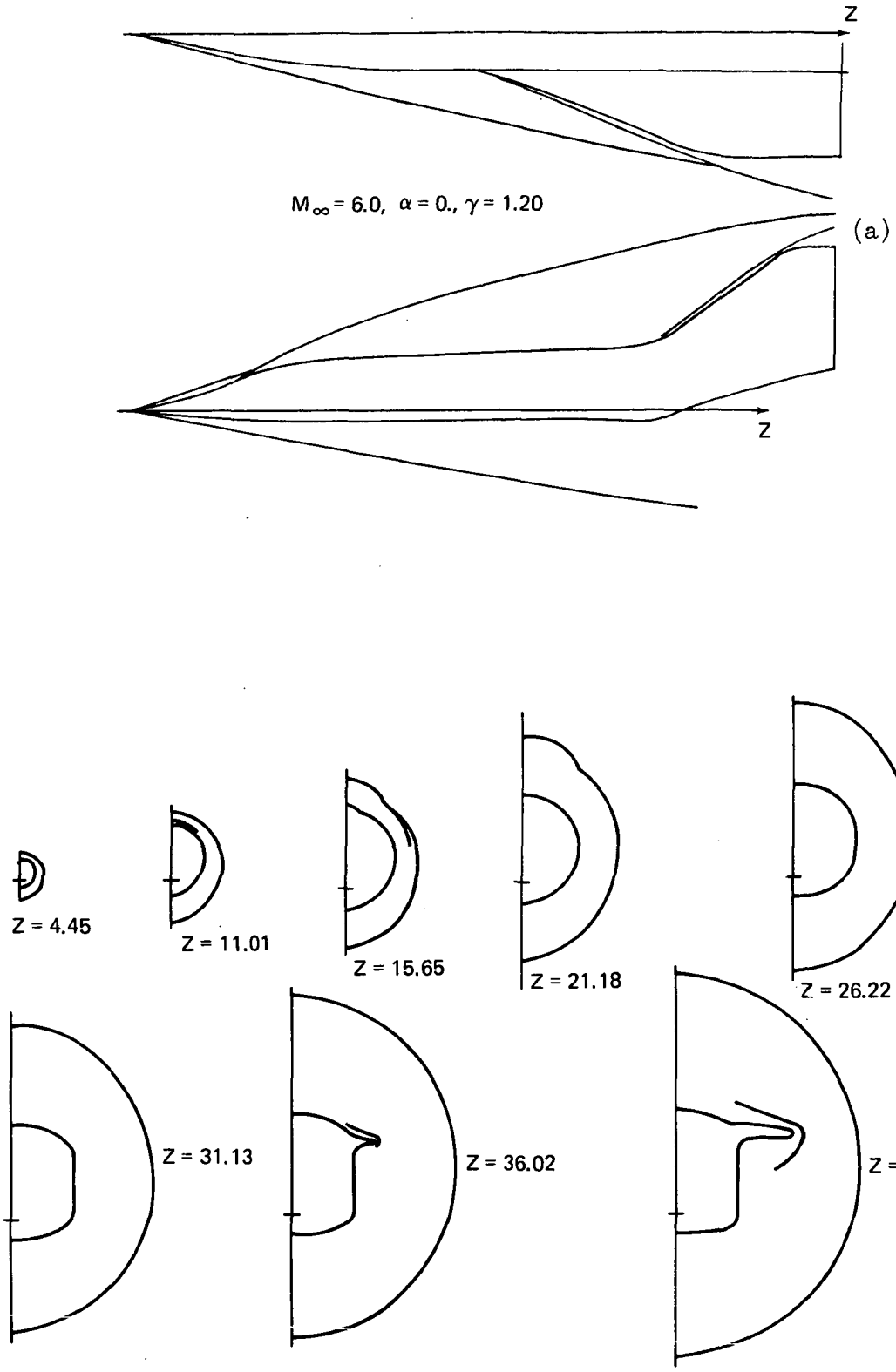

Figure 42. - Hypersonic research aircraft, shock pattern.

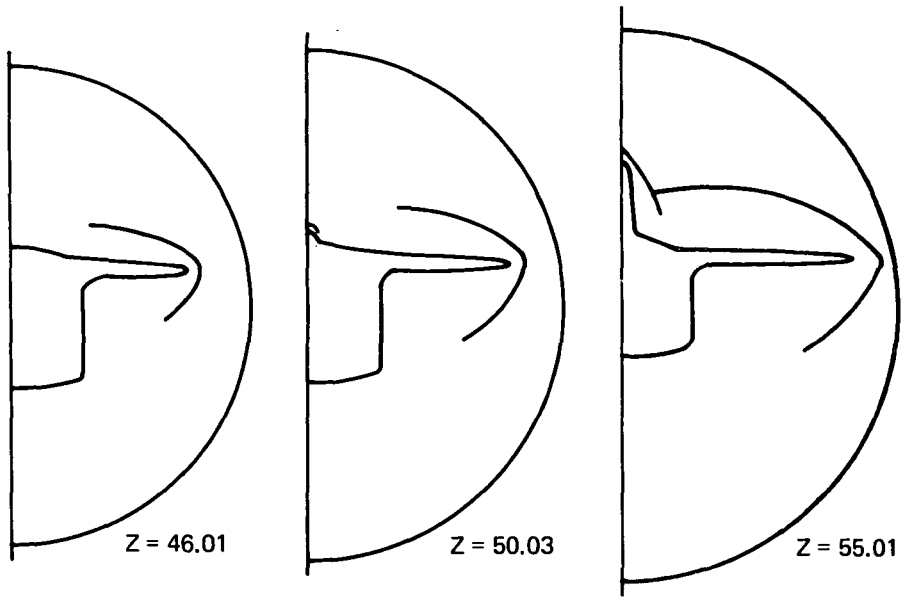

(b)

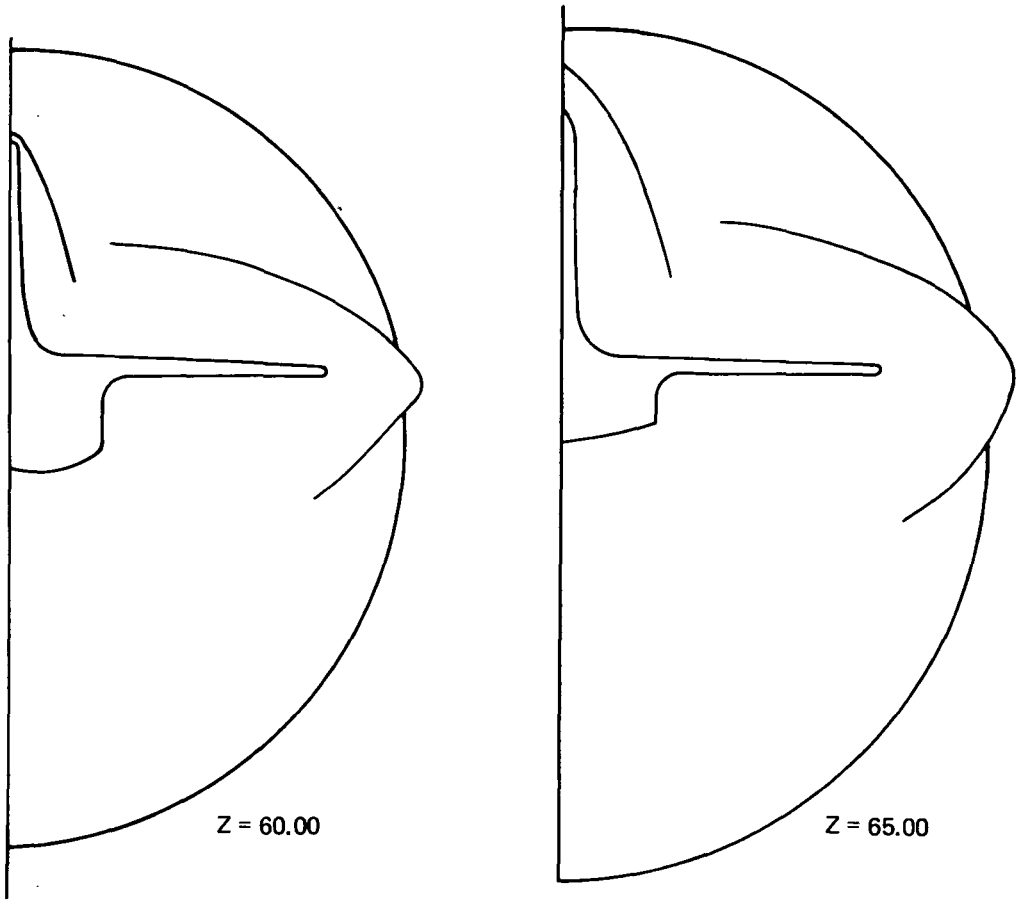

Figure 42. - Hypersonic research aircraft, shock pattern (contd).

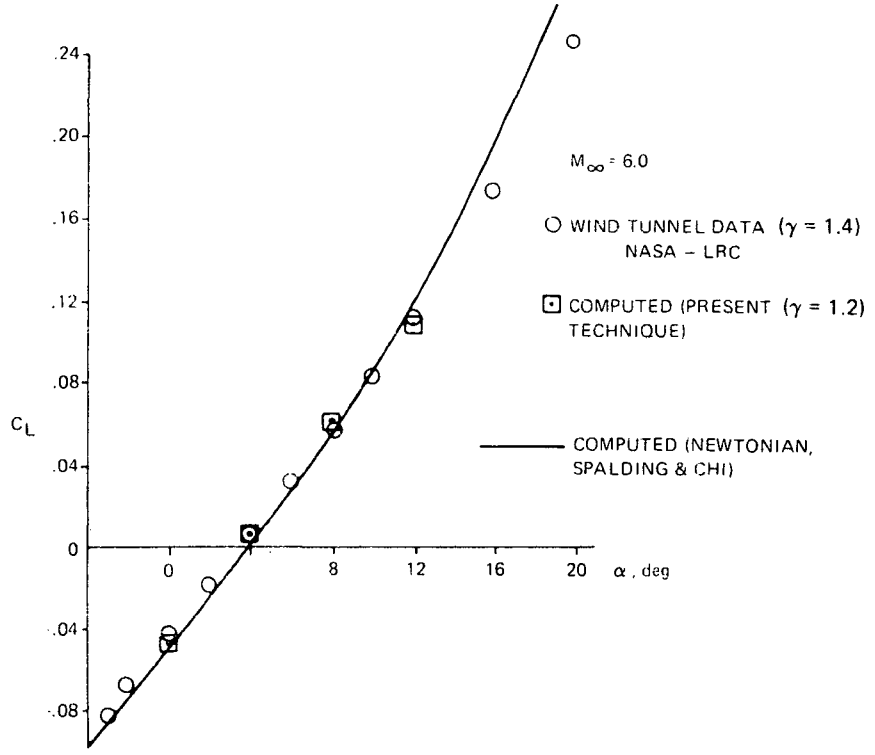

Figure 43. - Hypersonic research aircraft, lift vs angle of attack.

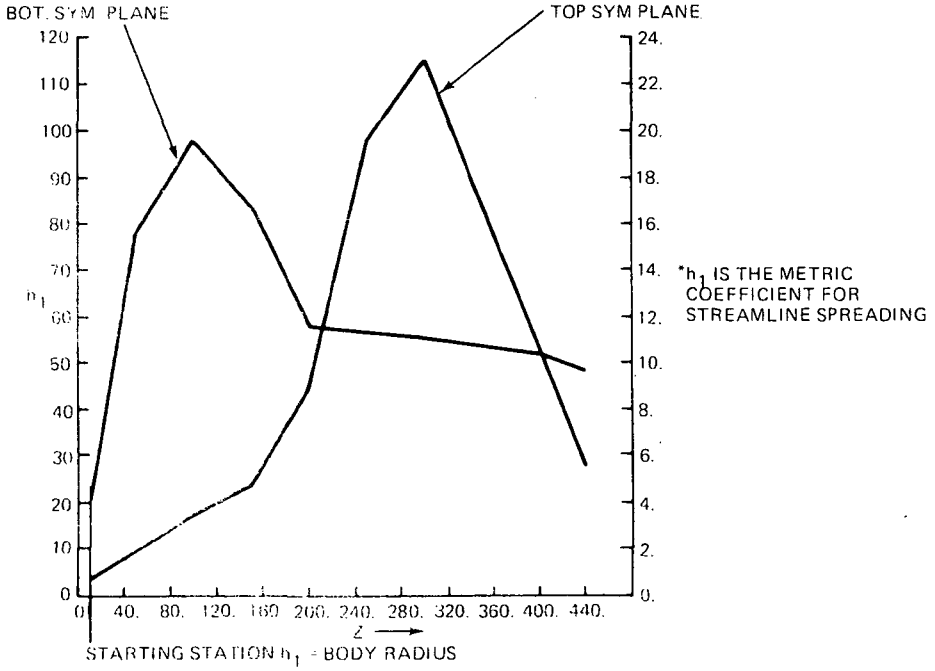

Figure 44. - Metric coefficient (h_1), F-111A, M_∞ = 2, α = 0

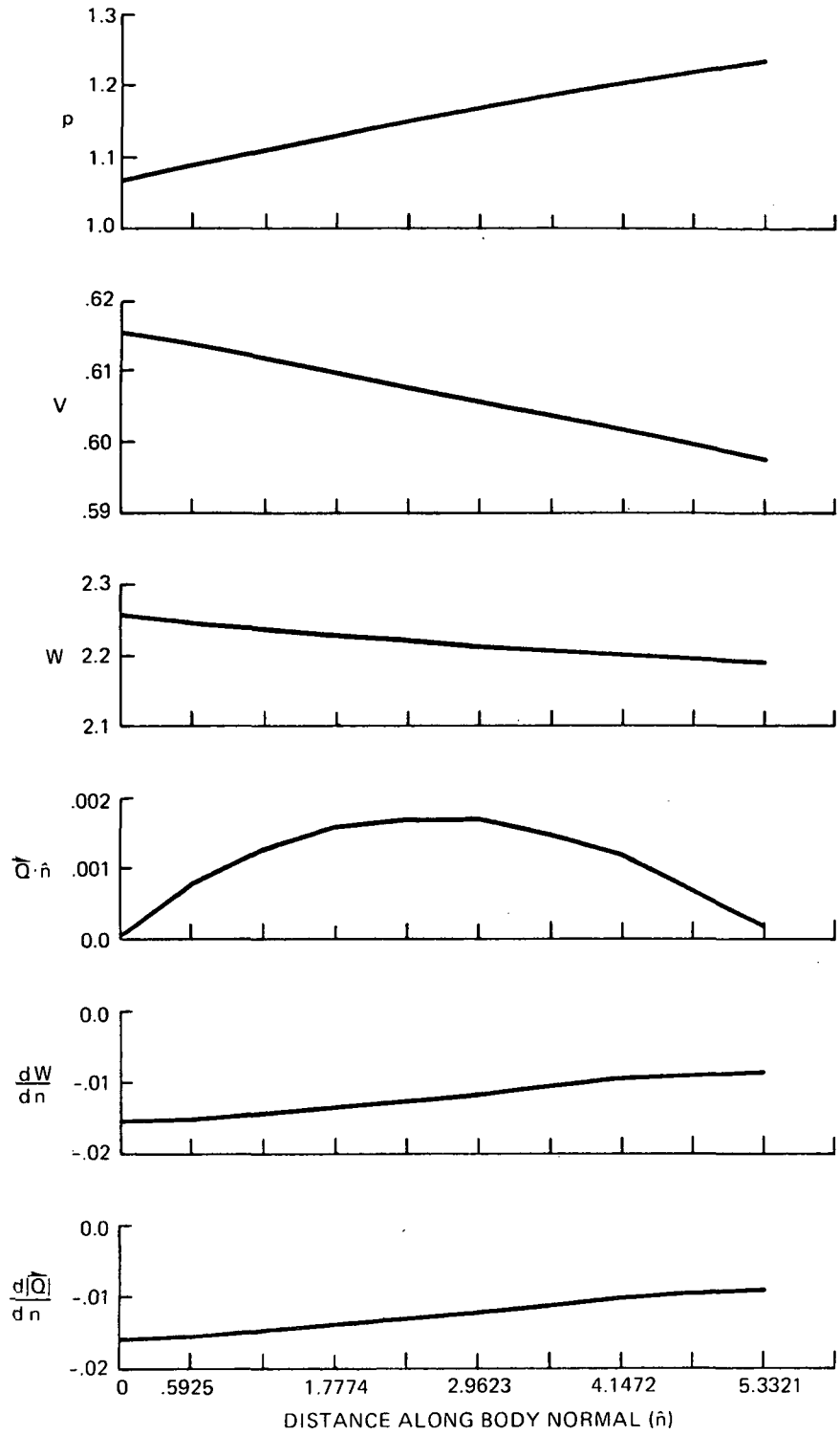

Figure 45. - Boundary layer quantities in pseudo-stream surface in top symmetry plane, F-111A, $M_\infty = 2.$, $\alpha = 5^\circ$.

CONCLUSIONS

1. A computer tool has been developed for a high-quality computation of the inviscid flow field about realistic vehicle configurations at supersonic and hypersonic speeds.

2. The underlying numerical techniques, while available for simple bodies, have been expanded, adapted and integrated into a tool. For high-quality results, all shocks are treated as shock discontinuities and entropy layers are handled in a special way. Moreover, a crucial element of the numerical technique evolved is the use of mappings to simplify the cross sectional shapes in the computational space and efficiently distribute a relatively small number of mesh points.

3. Equilibrium and frozen air are included.

4. The computer tool automatically produces specialized outputs such as aerodynamic coefficients, metric factors, normal derivatives in pseudo stream surfaces and sonic boom data.

5. The initial results obtained from the computer tool for orbiter and other configurations are quite satisfactory.

6. As an orientation, the machine time expenditure for the flow field past a typical orbiter configuration at $M = 26.1$, $\alpha = 30^{\circ}$, and for a perfect gas is about 1.5 hours on the C.D.C. 6600.

REFERENCES

1. G. Moretti: Three-Dimensional, Supersonic, Steady Flows with Any Number of Imbedded Shocks, AIAA Paper No. 74-10, (1974).

2. L. D'Attorre; M. A. Bilyk; and R. J. Sergeant: Three Dimensional Supersonic Flow Field Analysis of the B-1 Airplane by a Finite Difference Technique and Comparison with Experimental Data. AIAA Paper No. 74-189, (1974).

3. P. Kutler; Harvard Lomax; and R. F. Warming: Computation of Space Shuttle Flow Fields Using Noncentered Finite-Difference Schemes, AIAA Paper No. 72-193, (1972)

4. G. Moretti; and G. Bleich: Three-Dimensional Flow Around Blunt Bodies. AIAA J5, (1966).

5. G. Moretti; B. Grossman; and F. Marconi: A Complete Numerical Technique for the Calculation of Three-Dimensional Inviscid Supersonic Flows, AIAA Paper No. 72-192, (1972).

6. G. Moretti: Thoughts and Afterthoughts about Shock Computations, PIBAL Report No. 72-37, (1972).

7. G. Moretti; and M. Pandolfi: Entropy Layers, J. Computers and Fluids, 1, 19, (1973).

8. G. Moretti; and M. Pandolfi: Analysis of the Inviscid Flow about a Yawed Cone. Preliminary studies, PIBAL Report No. 72-18, (1972).

9. A. Vachris; and L. Yaeger: QUICK-GEOMETRY User's Manual, Grumman Aerospace-Aerodynamic Section Technical Data Report, 393-74, (1974).

10. D. J. Jones: Tables of Inviscid Supersonic Flow about Circular Cones at Incidence, $\gamma = 1.4$, AGARD A6137, (1969).

11. J. L. Sims: Tables for Supersonic Flow Around Right Circular Cones at Zero Angle of Attack, NASA SP-3004, (1964).

12. R. S. Skulsky: A Conformal Mapping Method to Predict Low-Speed Aerodynamic Characteristics of Arbitrary Slender Re-entry Shapes, J. Spacecraft, V3, No. 2, (1966).

13. R. Courant; K. O. Friedricks; and H. Lewy: Ubber die partiellen Differenzgleichungen der Mathematischen Physik, Math. Ann., 100, 32, (1928).

14. R. W. MacCormack: The Effects of Viscosity in Hypervelocity Impact Cratering, AIAA Paper No. 69-354, (1969).

15. AMES Research Staff: Equations, Tables and Charts for Compressible Flow, NACA 1135, (1953).

16. G. Moretti: Analytical Expressions for a Speedy Computation of Thermodynamical Properties of Air, General Applied Science Laboratory, TM-39, (1960).

17. W. G. Vincenti; and C. H. Kruger: Introduction to Physical Gas Dynamics, Wiley (New York), (1967).

18. F. Marconi; and M. Salas: Computation of Three-Dimensional Flows about Aircraft Configurations, J. Computers and Fluids, 1, 185, (1973).

19. F. Marconi; L. Yaeger; and H. H. Hamilton: Computation of High-Speed Inviscid Flows About Real Configurations, NASA SP-347 (1975).

20. A. H. Whitehead Jr.; and J. C. Dunavant: A Study of Pressure and Heat Transfer Over an 80° Sweep Slab Delta Wing in Hypersonic Flow. NASA TN-D - 2708, (1965).

21. C. Prokop: Investigation of the Effects of Airframe Design on Inlet Flow Fields. AFFDL-TR-72-11 1, (1972).

APPENDIX A

Second Derivatives of Mappings

$$G_\zeta = W_{1\zeta}\, W_{3_{W_2}}\, W_{5_{W_4}}$$

$$G_{\zeta\zeta} = W_{1\zeta\zeta}\,(W_{3_{W_2}})(W_{5_{W_4}}) + W_{1\zeta}\,(W_{5_{W_4}})(W_{3_{W_{2\zeta}}}) + W_{1\zeta}\,(W_{5_{W_{4\zeta}}})(W_{3_{W_2}})$$

$$\therefore\ \zeta_{GG} = G_{\zeta\zeta}/G_\zeta^3$$

(if $\zeta = u+iv$)

$$u_{xx} = \mathrm{Re}\,(\zeta_{GG})$$

$$v_{xx} = \mathrm{Im}\,(\zeta_{GG})$$

using the Cauchy-Riemann conditions we can get $u_{yy} = -u_{xx}$, $u_{yx} = -v_{yy}$ etc.

Now we can differentiate equations (7) to get:

$$r_{xr} = (u_r u_x + u u_{xr} + v_r v_x + v v_{xr})/r - r_x/r$$

$$r_{yr} = (u_r u_y + u u_{yr} + u_r v_y + v v_{yr})/r - r_y/r$$

$$r_{y\theta} = (u_\theta u_y + u u_{yr} + v_\theta v_y + v v_{y\theta})/r$$

$$\theta_{xr} = (u_r v_x + u v_{xr} - v_r u_x - v u_{xr})/r^2 - 2\theta_x/r$$

$$\theta_{yr} = (u_r v_y + u u_{yr} - v_r u_y - v u_{yr})/r^2 - 2\theta_y/r$$

$$\theta_{x\theta} = (u_\theta v_x + u v_{x\theta} - v_\theta u_x - v u_{x\theta})/r^2$$

$$\theta_{y\theta} = (u_\theta v_y + u v_{y\theta} - v_\theta u_y - v u_{y\theta})/r^2$$

Now:

$$G_{\zeta z} = W_{1\zeta z}\,(W_{3W_2})(W_{5W_4}) + (W_{3W_{2z}})(W_{1\zeta})(W_5 W_4) + (W_{5W_{4z}})(W_{1\zeta})(W_{3W_4})$$

$$\zeta_{Gz} = -\,(G_{\zeta z} - G_{\zeta\zeta}\,\zeta_G G_z)/G_\zeta^2$$

$$u_{xz} = \mathrm{Re}\,(\zeta_{Gz})$$

$$v_{xz} = \mathrm{Im}\,(\zeta_{Gz})$$

Then we can get r_{xz}, r_{yz}, θ_{xz} and θ_{yz} by taking the derivatives of equations (7). In order to get r_{zz} and θ_{zz} we take the z derivatives of equations (8) and calculate x_{zz} and y_{zz} (again $A_{zz} = A_{zz}$, $B_{zz} = B_{zz}$, etc. since $z = z$), and we get from (9)

$$r_{zz} = -\,(r_y y_z + r_y y_{zz} + r_{xz} x_z - r_x x_{zz})$$

$$\theta_{zz} = -\,(\theta_y y_z + \theta_y y_{zz} + \theta_{xz} x_z - \theta_x x_{zz})$$

APPENDIX B

Coefficients of Transformed Euler Equations

$$A_1 = w^2 - \gamma T = w^2 - a^2$$

$$A_2 = \theta_z + (\theta_x u + \theta_y v)\, w/A_1$$

$$A_3 = \theta_z + \theta_x u/w + \theta_y v/w$$

$$A_4 = (\theta_x u + \theta_y v)/A_1$$

$$A_5 = \theta_z + (r_x u + r_y v)w/A_1$$

$$A_6 = r_z + r_x\, u/w + r_y v/w$$

$$A_7 = (r_x u + r_y v)/A_1$$

$$a_{11} = X_{\not z} + X_r A_5 + X_\theta A_2$$

$$a_{12} = X_x \gamma w/A_1$$

$$a_{13} = X_y \gamma w/A_1$$

$$a_{14} = -\gamma(X_r A_7 + X_\theta A_4)$$

$$b_{11} = Y_{\not z} + Y_r A_5 + Y_\theta A_2$$

$$b_{12} = \gamma w Y_x/A_1$$

$$b_{13} = \gamma w Y_y/A_1$$

$$b_{14} = -\gamma(Y_r A_7 + Y_\theta A_4)$$

$$a_{21} = X_x T/w$$

$$a_{22} = X_{\not z} + X_r A_6 + X_\theta A_3$$

$$b_{21} = X_x T/w$$

$$b_{22} = Y_{\not 2} + Y_r A_6 + Y_\theta A_3$$

$$a_{31} = X_y T/w$$

$$a_{33} = a_{22}$$

$$b_{31} = Y_y T/w$$

$$b_{33} = b_{22}$$

$$a_{41} = -T(X_r A_7 + X_\theta A_4)$$

$$a_{42} = -X_x \gamma T/A_1$$

$$a_{43} = -X_y \gamma T/A_1$$

$$a_{44} = X_{\not 2} + A_5 X_r + A_2 X_\theta$$

$$b_{41} = -T(Y_r A_7 + Y_\theta A_4)$$

$$b_{42} = -Y_x \gamma T/A_1$$

$$b_{43} = -Y_y \gamma T/A_1$$

$$b_{44} = Y_{\not 2} + Y_r A_5 + Y_\theta A_2$$

$$a_{55} = a_{22}$$

$$b_{55} = b_{22}$$

NATIONAL AERONAUTICS AND SPACE ADMINISTRATION
WASHINGTON, D.C. 20546

OFFICIAL BUSINESS
PENALTY FOR PRIVATE USE $300

SPECIAL FOURTH-CLASS RATE
BOOK

POSTAGE AND FEES PAID
NATIONAL AERONAUTICS AND
SPACE ADMINISTRATION
451

U.S. MAIL

POSTMASTER: If Undeliverable (Section 158 Postal Manual) Do Not Return

"The aeronautical and space activities of the United States shall be conducted so as to contribute . . . to the expansion of human knowledge of phenomena in the atmosphere and space. The Administration shall provide for the widest practicable and appropriate dissemination of information concerning its activities and the results thereof."

—NATIONAL AERONAUTICS AND SPACE ACT OF 1958

NASA SCIENTIFIC AND TECHNICAL PUBLICATIONS

TECHNICAL REPORTS: Scientific and technical information considered important, complete, and a lasting contribution to existing knowledge.

TECHNICAL NOTES: Information less broad in scope but nevertheless of importance as a contribution to existing knowledge.

TECHNICAL MEMORANDUMS: Information receiving limited distribution because of preliminary data, security classification, or other reasons. Also includes conference proceedings with either limited or unlimited distribution.

CONTRACTOR REPORTS: Scientific and technical information generated under a NASA contract or grant and considered an important contribution to existing knowledge.

TECHNICAL TRANSLATIONS: Information published in a foreign language considered to merit NASA distribution in English.

SPECIAL PUBLICATIONS: Information derived from or of value to NASA activities. Publications include final reports of major projects, monographs, data compilations, handbooks, sourcebooks, and special bibliographies.

TECHNOLOGY UTILIZATION PUBLICATIONS: Information on technology used by NASA that may be of particular interest in commercial and other non-aerospace applications. Publications include Tech Briefs, Technology Utilization Reports and Technology Surveys.

Details on the availability of these publications may be obtained from:

SCIENTIFIC AND TECHNICAL INFORMATION OFFICE

NATIONAL AERONAUTICS AND SPACE ADMINISTRATION

Washington, D.C. 20546